Tunable diode-laser absorption-based sensors for the detection of water vapor concentration, film thickness and temperature

Von der Fakultät für Ingenieurwissenschaften,
Abteilung Maschinenbau und Verfahrenstechnik der

Universität Duisburg-Essen

zur Erlangung des akademischen Grades

einer

Doktorin der Ingenieurwissenschaften

Dr.-Ing.

genehmigte Dissertation

von

Huinan Yang

aus

Sichuan, China

Referent: Prof. Dr. Christof Schulz

Korreferent: Prof. Dr. Volker Ebert

Tag der mündlichen Prüfung: 12. Januar 2012

Summary

Temperature and species concentration are fundamental parameters in combustion-related systems. For optimizing the operation and minimizing the pollutant emissions of combustion devices and to provide validation data for simulations, quantitative measurement techniques of these parameters are required.

Laser-based diagnostic techniques are an advantageous tool for in-situ non-intrusive measurement in combustion related systems, e.g. flame reactors, combustors, and shock tubes. Fiber-based multiplexed tunable diode laser absorption spectroscopy (TDLAS) is attractive and employed in this thesis because of compact, rugged packaging, low cost, reliability and relative ease of use. In the present work, water (H_2O) is chosen as the target species for the technique, since it has a rich absorption spectrum in the vapor-phase and a broad-band absorption spectrum for the liquid-phase in the near infrared region (NIR).

TDLAS two-line thermometry is used to determine the temperature in gas-phase systems with homogenous temperature distribution. However, in many practical environments, temperature varies along the beam path. For this case the temperature-binning technique is used for retrieving non-uniform temperature distributions from line-of-sight (LOS) absorption data with multiplexed five-color absorbance areas. In this thesis, TDLAS was applied to determine the spatially-resolved temperature information inside a low-pressure nanoparticle flame synthesis reactor. The temperature distribution was obtained by assuming the temperature to be constant in variable lengths along the LOS. The length fractions for the temperature values along the LOS are determined using postulated temperature bins.

Quantitative knowledge of liquid film thickness is important in many industrial applications. One example is Diesel engine exhaust gas aftertreatment, where NO_x reduction via selective catalytic reduction (SCR) is accomplished in the exhaust using sprays of water/urea solutions. In this thesis a novel TDLAS sensor was developed to simultaneously measure the water film thickness, film temperature and vapor-phase temperature above the film. For this sensor four individual NIR wavelengths were selected for optimized sensitivity of the technique. The sensor was first validated using a calibration tool providing known film thicknesses and temperature, and then applied to open liquid water films deposited on a transparent quartz plate. In a collaborative project the technique was also compared with imaging measurements based on laser-induced fluorescence and Raman scattering, respectively. Furthermore, the TDLAS sensor was applied to determine time series data of liquid water film thickness resulting from impinging water jets and subsequent film evaporation on the wall of a gas flow channel.

Zusammenfassung

Temperatur und Spezies-Konzentration sind elementare Kenngrößen in Verbrennungssystemen. Um den Betrieb von Verbrennungs- und Reaktionsprozessen zu optimieren, die Schadstoffemission zu minimieren und außerdem Validierungsdaten für Simulationen zu generieren, sind quantitative Messungen dieser Kenngrößen notwendig.

Laserbasierte Diagnostik-Methoden sind nützliche Verfahren für die berührungslose in-situ Messung innerhalb von Verbrennungssystemen wie z.B. Brenner, Flammenreaktoren und Stoßwellenrohren. Absorptionsspektroskopie mit mehreren faserbasierten und abstimmbaren Laserdioden (tunable diode laser absorption spectroscopy, TDLAS) wurde in dieser Arbeit wegen des kompakten, robusten Aufbaus, der kostengünstigen Komponenten und der Zuverlässigkeit aufgrund der optischen Fasern verwendet. In der vorliegenden Arbeit wurde Wasser (H_2O) als Untersuchungssubstanz für diese Methode ausgewählt, da es in zahlreichen technisch relevanten Prozessen, im nahen Infrarot-Bereich (NIR) in der Gasphase ein schmalbandiges und in der flüssigen Phase ein breitbandiges Absorptionsspektrum besitzt.

Die TDLAS-zwei-Linien-Thermometrie wird zur Temperaturbestimmung in Verbrennungssystemen mit homogener Temperaturverteilung benutzt. In anwendungsnahen Systemen jedoch ändert sich die Temperatur entlang des Strahlweges. In diesem Fall ist ein Temperatur-binning-Verfahren nötig, um aus einer Absorptionsmessung entlang einer Sichtlinie auch auf ungleichförmige Temperaturverteilungen rückschließen zu können. In der vorliegenden Arbeit wurde TDLAS mit einer Kombination von fünf Wellenlängen eingesetzt, um räumlich aufgelöst Temperaturen innerhalb eines Niederdruck-Nanopartikel-Synthesereaktors zu bestimmen. Dabei wurden Temperaturen bestimmt, indem diese in variablen Längen entlang der Sichtlinie als konstant angesehen wurde. Die Längenanteile dieser Wegstrecken mit verschiedenen Temperaturen wurden für vordefinierte Temperaturbereiche bestimmt.

Die quantitative Kenntnis der Filmdicke von flüssigen Filmen ist wichtig für zahlreiche industrielle Anwendungen, z.B. die NO_x-Reduktion mittels einer Wasser/Harnstoff-Lösung in selektiv-katalytischer Reduktion (selective catalytic reduction, SCR) im Abgas von Dieselmotoren. In der vorliegenden Arbeit wurde ein neuartiger TDLAS-Sensor entwickelt, um gleichzeitig Filmdicke, Filmtemperatur und Wasserdampftemperatur oberhalb des Films zu messen. Die vier eingesetzten NIR-Wellenlängen wurden hierbei auf optimale Empfindlichkeit hin ausgewählt. Der Sensor wurde zuerst in einer Kalibrationszelle mit bekannter Filmdicke und Filmtemperatur validiert und dann an einem freien Film auf einer transparenten Quarzglas-Platte getestet. Zusätzlich wurde der TDLAS-Sensor verwendet, um zeitaufgelöst die Filmdicke während der Einspritzung- und Verdampfungsprozesse innerhalb eines Strömungskanals zu bestimmen.

Contents

1 Introduction

Improvement of combustion efficiency and reduction of emissions in combustion-related systems are key tasks in the next decades due to limited fuel resources on earth and an increasingly deteriorated environment. Measurements of combustion parameters, e.g. temperature, species concentrations are helpful to understand the combustion process, improve the combustion efficiency and reduce the production of pollutants. Laser-based diagnostics is advantageous in providing in-situ measurements of these parameters due to its non-intrusiveness, fast time response, high sensitivity, and robustness [1-3].

Tunable diode laser absorption spectroscopy (TDLAS) is one of the attractive diagnostics methods [4-7]. Compared with many bulky laser systems, diode lasers are compact, ruggedly packed, low-cost instruments and can be used with relative ease [4]. Furthermore, their wavelengths can be directly tuned by varying the injection current thus scanning over the entire lineshape of an absorption line. In addition, the diode lasers employed in the present work emit around ~1.4 μm in the near-infrared (NIR) region, which is a wavelength region that is commonly used for telecommunication [4]. Therefore, robust systems have been developed and are readily available at low cost.

Temperature is a fundamental parameter in combustion processes. Several methods have been developed to measure the temperature. A traditional thermometer requires thermal contact with the object of interest. Glass and gas thermometers are based on the thermal expansion of liquids and gases, respectively. The frequently used thermocouples are based on the thermoelectric effect generating a potential difference at the bead of two different metals. Optical methods can measure the temperature remotely, like laser-induced fluorescence (LIF) [8-9], UV absorption [10], coherent anti-Stokes Raman scattering (CARS) [11], and TDLAS [12-13] applied in this thesis. For more detailed reviews on the laser-based gas phase temperature measurement techniques, see [14-15].

Water vapor (H_2O) is a major product in hydrocarbon combustion and has a rich absorption spectrum in the NIR region from 1.3 to 1.5 μm, where the v_1+v_3 combination and $2v_1$ overtone bands of H_2O absorption spectra overlap with the commonly used NIR-telecommunication bands. In the liquid phase, due to van der Waals hydrogen bridge bonding and hindered rotations H_2O exhibits broad unstructured absorption bands in the OH-stretch vibrational overtone and combination band regions within the same spectral range. The selection of appropriate absorption lines is very important for the TDLAS sensor employed in the thesis for both vapor-phase temperature and liquid film measurement. The HITRAN (High Resolution Transmission Molecular Absorption Database) database [16-17] contains spectroscopic parameters for specific spectral lines, which allows to simulate the gas-phase absorption spectra and to optimize the line selection.

TDLAS two-line thermometry [12-13, 18-19] is a frequently used method for TDLAS temperature measurements. The gas temperature is determined by forming a ratio between the line strengths of two different transitions which have different temperature dependences (different lower state energies). Therefore, this technique is exact for temperature measurements in homogenous gas-phase distributed systems or for very short pathlengths where the temperature distribution can be assumed uniform. However, in many practical applications, temperature varies significantly along the beam path. The temperature distribution along the beam path can be determined by using multiple transitions with different temperature dependences, that is, different lower state energy. Hence, other strategies, like temperature-binning techniques [20] were applied to determine the most probable temperature distribution along the beam path using estimated temperature bins. In the present thesis the temperature binning technique is first validated on an atmospheric-pressure burner, and then applied in a low-pressure nanoparticle synthesis premixed-flame reactor.

Liquid film formation and evaporation is common in many practical applications. For the design and optimization of the application systems, e.g., Diesel engine exhaust gas aftertreatment, a quantitative measurement of film thickness is important. Various methods [21-23] have been developed to determine the film thickness. In the present work the motivation to develop a film thickness measurement technique is related to exhaust gas aftertreatment in modern Diesel engines by selective catalytic reduction (SCR) of nitrogen oxides (NO_x), where water-based urea solutions are injected into the exhaust manifold, which generally is accompanied by wall wetting. Temperature measurements in liquid films are important to understand heat and mass transfer processes [24]. In many applications the temperature of the liquid film is not known, which is an important quantity on one hand when determining heat transfer and simulating evaporation. On the other hand, temperature information helps for the evaluation of film thickness because the essential physical parameters required for signal evaluation in absorption or emission based techniques, such as temperature-dependent parameter, absorption cross-sections and fluorescence quantum yields. Thermocouples are typically inadequate for applications in thin liquid films. Therefore, non-intrusive techniques are required.

A novel multi-wavelength TDLAS based sensor was developed here for liquid water film thickness measurements, which simultaneously is capable to rapidly scan the narrow line-shapes of water vapor via current tuning of the diode lasers to obtain the vapor-phase temperature and thus distinguish from laser attenuation due to absorption of the liquid and other non-specific attenuation, e.g. window fouling, scattering, beam steering, etc. The film thickness and temperature can be then determined by forming the absorbance ratio at three wavelengths assessing the broad-band attenuation of liquid water. Thus, the liquid-film temperature changed during film evaporation can be obtained in real time with getting more accurate film thickness.

In this work, four diode lasers were chosen based on an optimization via a sensitivity analysis. The developed TDLAS sensor is first validated using a calibration tool providing known water film thickness at known temperatures. In a second step the sensor is applied to open water films deposited on a transparent quartz plate for the simultaneous measurement of liquid film thickness, liquid-phase temperature and vapor-phase temperature above the film. The TDLAS technique is compared to the results of water film thickness imaging diagnostics methods based on tracer based laser-induced fluorescence (LIF) and spontaneous Raman scattering. Finally, the sensor is also applied for the film thickness measurements in a flow channel.

The main objective of the thesis is to develop fiber-based, multiplexed tunable diode laser absorption spectrometers for the measurement of spatially-resolved temperature in a low pressure premixed-flame flame reactor, and for the development and application of a system to simultaneously measure liquid water film thickness, temperature and vapor phase temperature. In the present chapter, the motivation and structure of the thesis are discussed. Chapter 2 introduces the background of diode laser and also presents the basic theory of absorption and the related important parameters and methods. Chapter 3 provides the vapor phase of the water absorption lines in the HITRAN spectroscopic database, the line selection strategies and an overview of the multiplexing techniques. The 1.4 µm H_2O sensor involved in the thesis and 2.7 µm CO_2 sensor planned for the future work are also introduced. A literature review of the related previous research is also given. Chapter 4 describes the spatially-resolved temperature sensing inside the low-pressure reactor. The temperature distribution inside a low-pressure flat-flame reactor is determined by a temperature-binning technique. Chapter 5 introduces the development and application of the 1.4 µm sensor for simultaneous measurement of liquid water film thickness and vapor-phase temperature above the film during film evaporation. Chapter 6 summarizes the major investigations and conclusions of the thesis, and suggests some future work in the related areas. Chapter 7 lists the achieved publications during the course of this PhD research, and the list of references and abbreviation are provided in chapter 8 and 9.

2 Theoretical background

In this chapter, the basics of the diode laser are briefly introduced. The basic theory of absorption and important related parameters such as the different kinds of broadening mechanisms are summarized. Finally, two methods of direct absorption spectroscopy: Fixed- and scanned-wavelength absorption techniques are discussed and the absorption-based thermometry for systems with homogenous and inhomogeneous temperature distribution is described.

2.1 Fundamentals of diode lasers

The first GaAs semiconductor diode laser was invented by three groups independently [25-27] in 1962 based on the analysis done by Basov et al. [28], and it has been developed fast over the last decades. Diode lasers have been widely used in a number of applications, e.g., in optical-fiber communication and optical data storage. For optical-fiber communication systems the systems are modified such that the laser output can be modulated by modulating the injection current. The development of diode lasers in the NIR region (1.3–1.5 µm) is mainly motivated by telecommunication industry, since optical fiber technology is well developed there as the most important medium for signal transmission with minimum loss at 1.3 µm and minimum dispersion of fiber material around 1.5 µm, respectively [29]. Therefore, the fiber-based distributed feedback (DFB) diode lasers at ～1.4 µm are used in most of our work presented here.

2.1.1 Basics of diode lasers

The basic structure of a typical diode laser is shown in Fig. 1. A *p*-doped layer is grown on top of an *n*-doped substrate. The *n*- and *p*-doping are processes that change the density of electrons and holes in the conduction band and valence band by increasing donor and acceptor concentrations, respectively. Current is injected via two electrodes, and lasing occurs in the active region which is shown as shaded area between both electrodes in Fig. 1. The shaded area indicates the depletion region in a simple *p*-*n* junction or an intrinsic layer in a heterostructure laser [29].

In order to understand the inversion created at a *p*-*n* junction, the Fermi-Dirac distribution law should be introduced first, which describes the probability that an electron state at energy E_e is occupied,

$$f(E_e) = \frac{1}{1 + \exp {(E_e - E_F)}/_{kT}} \tag{1}$$

where E_F is the Fermi energy, which is the chemical potential of electrons in semiconductors, k is the Boltzmann constant and T is the temperature. At $T = 0$ K, according to eq. 1, all the states below E_F are filled with electrons, and those above it are empty. Due to the current flow in the *p*-*n* junction, a number of electrons and holes are created by the applied potential, the quasi-Fermi levels E_{Fc} and E_{Fv} are used for the conduction band and valence band, respectively.

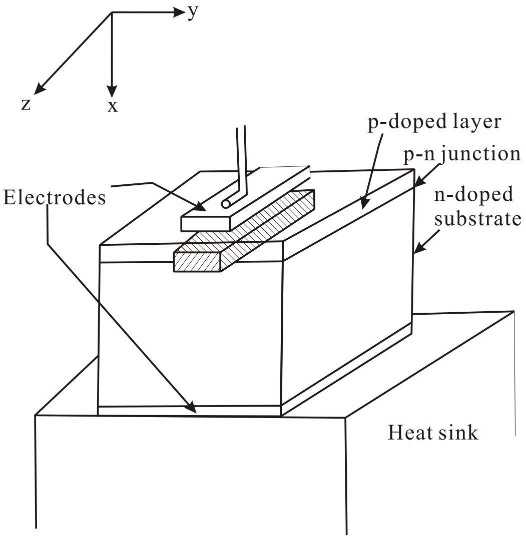

Fig. 1: Schematic drawing of a diode laser [29]

In Fig. 2 the energy bands and their population (shaded areas) are plotted as a function of *x* direction which is perpendicular to the junction plane. When there is no applied voltage the Fermi energy is constant throughout the whole structure and no net flow of carriers occurs (Fig. 2a). When an external voltage is applied, the *p*-doped region is relative positive than the *n*-doped region (Fig. 2b). Stimulated emission occurs in the active region because of electron-hole recombination. Lasing occurs when the rate of stimulated emission approximately equals the total rate of optical losses. The injection current needed to initiate the lasing is called the threshold current.

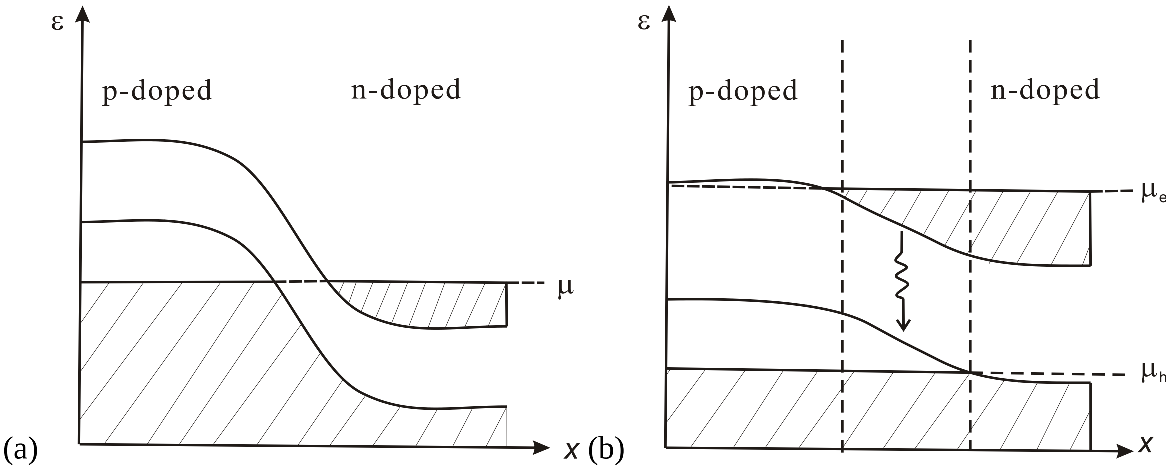

Fig. 2: Electron energy and occupation perpendicular to the p-n junction (a) without an applied voltage and (b) with a forward biased applied voltage [29]

Several types of diode lasers have been developed in the last decades, e.g., edge-emitting lasers: Fabry-Perot (FP) laser; distributed Bragg grating (DBR) and distributed feedback (DFB) lasers, and surface-emitting laser: Vertical cavity surface emitting lasers (VCSELs), quantum cascade lasers and external cavity lasers. However, only the edge-emitting lasers will be discussed further in this thesis. The structure of these lasers is such that the emitted laser beams and laser cavities are parallel to the laser substrates.

2.1.2 Fabry-Perot laser

The Fabry-Perot (FP) laser is the simplest and cheapest type of diode lasers. It consists of two parallel mirrors by polishing and coating the facets of the semiconductor body. Light travels back and forth between the polished interfaces thus forming a standing wave in the laser as shown in Fig. 3. The gain medium is assumed to be homogenous. However, the FP laser is usually not operated single-mode, but with several different amplitudes in longitudinal modes. Hence, the FP laser is not applicable for high-resolution spectroscopic measurements. For example, in an InGaAsP/InP FP laser at 1.55 μm, 4 to 10 longitudinal modes can occur [30]. Since the lasing conditions are not reproducible, the laser may operate on different modes from one day to another even with the same operating temperature and current [4]. In order to obtain single-mode operation, this structure can be improved by a coupled cavity, the grating-based structure which can provide the wavelength-selective reflection is one of the choice and two kinds of common structures will be discussed next.

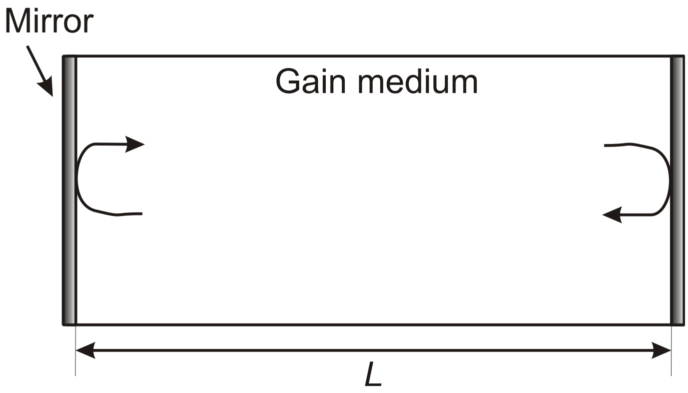

Fig. 3: Schematic drawing of FP laser in the longitudinal axis

2.1.3 DBR and DFB diode lasers

The basic structure of the DBR laser (Fig. 4) is that the cleaved facet at one or both ends of the FP laser is replaced by a grating. An antireflection (AR) coating is applied on the grating in order to avoid any partial reflection at the output. The DBR laser has an active region with length L_a and a grating length of L_b. In a DBR laser, the active region provides gain, while the grating provides the wavelength selectivity. It has the advantage of fast discreet and continuous tuning speeds on both the phase section and Bragg section [31].

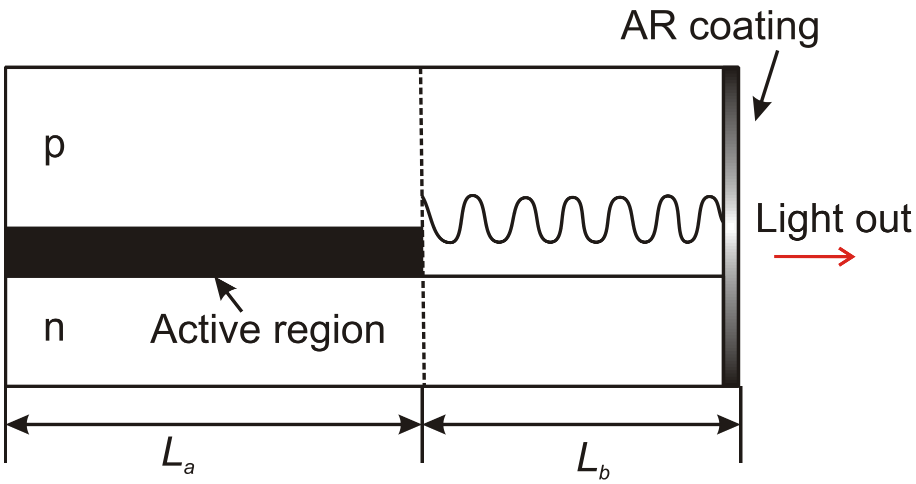

Fig. 4: A typical DBR laser structure

In a DFB laser both functions – gain and wavelength selectivity – are distributed in the same spatial region: A typical DFB structure is shown in Fig. 5. The DFB laser is much easier to manufacture than DBR laser because of the longitudinal uniformity and is widely used in telecommunication applications [4]. The DFB diode lasers can be wavelength-tuned in two different ways: temperature tuning and current tuning. In the first case the optical refractive index of the medium is changed by varying the temperature of the diode and the laser can be tuned by 3 to 5 nm between 275 and 325 K. In the case of current tuning, the optical index can be adjusted by changing the injection current at a fixed temperature, the laser wavelength can be tuned extremely rapidly. The injection current tuning range with this method is only around 1–2 cm^{-1}. It is limited by the threshold current at the low gain limit and output facet damage at high end [4].

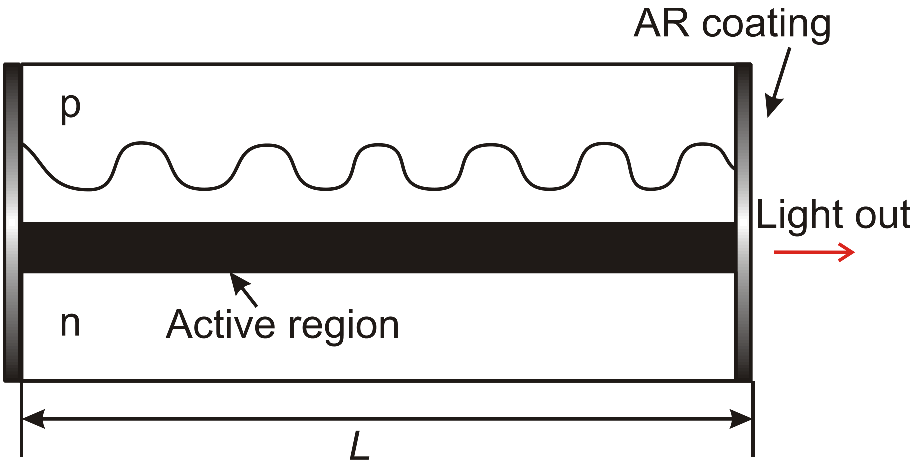

Fig. 5: A standard DFB laser structure

2.2 Spectroscopy

It is necessary to introduce the relationship in the vacuum between wavelength λ [nm], frequency ν [s^{-1}] and wavenumber $\tilde{\nu}$ [cm^{-1}] at first

$$c = \lambda\nu \tag{2}$$

$$\tilde{\nu} = {}^{1}\!/_{\lambda} \tag{3}$$

here, c is the speed of light [m/s].

In the gas phase the interactions between light and matter are in the form of emission, scattering and absorption. Since the energy levels of the molecules are discrete, emission or absorption can only occur at certain cases when there is a match between the energy of the photon and the difference in initial and final energy level. In quantum mechanics, the time-independent Schrödinger equation $\Psi(x)$ is used to determine the energy levels for the molecule with mass m moving in a potential field by $U(x)$,

$$\frac{d^2\psi(x)}{dx^2} + \frac{8m\pi^2}{h^2}[E - U(x)]\psi(x) = 0 \tag{4}$$

where E is the total energy of the system,

$$E = E_{elec} + E_{vib} + E_{rot} \tag{5}$$

where h is Planck‘s constant. E_{elec} is the electronic energy, E_{vib} is the vibrational energy and E_{rot} is the rotational energy. They are depending on quantum numbers.

If one assumes the diatomic molecule is a rigid rotor the rotational energy can be obtained as

$$E_{rot} = BJ(J+1) \tag{6}$$

where J = 0, 1, 2, 3, … is the rotational quantum number and B [cm^{-1}] is the rotational constant. For pure rotational lines (absorption or emission), the change in rotational quantum number is $\Delta J = \pm 1$. And the rotational frequencies for these transitions are given by

$$v_{J' \leftarrow J''} = 2B\left(J'' + 1\right) \tag{7}$$

where J' and J'' are the quantum numbers for the upper and lower state, respectively.

If one further assumes that the diatomic molecule is a simple harmonic oscillator (SHO), the vibrational energy is given by

$$E_{vib} = w_e\left(\upsilon + \frac{1}{2}\right) \tag{8}$$

where υ = 0, 1, 2, 3,… is the vibrational quantum number, and w_e is the energy spacing between adjacent quantum states. The quantum mechanics solution for absorption and emission assumed by the SHO model leads to a simple selection rule that says that the change in vibrational quantum number is $\Delta\upsilon = \pm 1$.

2.2.1 Boltzmann distribution

The Boltzmann equation describes the temperature-dependent population distribution of the molecules in their allowed quantum states. The fraction of molecules or atoms in energy level i can be described by [32],

$$f_i = \frac{N_i}{N} = \frac{g_i exp\left(-\frac{\varepsilon_i}{kT}\right)}{Q} \tag{9}$$

where g_i is the degeneracy of level i, ε_i is the common energy for state i, N is the total number of molecules,

$$N = \sum_i N_i \tag{10}$$

and the partition function Q is given by,

$$Q = \sum_i g_i exp\left(-\frac{\varepsilon_i}{kT}\right) = Q_{rot}\, Q_{vib} Q_{elec} \tag{11}$$

which in this approximation can also be described as the product for rotational, vibrational and electronic partition functions ,that are Q_{rot}, Q_{vib}, and Q_{elec}, respectively.

2.2.2 Absorption

If radiative transitions between two molecular quantum states are allowed, there is a high probability in state 1 or 2 for transitions as is shown in Fig. 6. The energy difference, ΔE, of the photon-induced transitions between these two quantum states can be described by Planck's law,

$$\Delta E = E_2 - E_1 = h\nu \tag{12}$$

Now let N_1 and N_2 denote the number of molecules in state 1 and 2, respectively. A_{21}, B_{12} and B_{21} are the Einstein coefficients for spontaneous emission, induced absorption and stimulated emission, respectively. A_{21} is the probability (per second) of spontaneous release of a photon with energy ΔE from state 2 to 1; $B_{12}\rho(\nu)$ is the probability (per second) that a molecule in state 1 exposed to radiation of spectral density $\rho(\nu)$ will absorb a quantum $h\nu$ and pass to state 2, $B_{21}\rho(\nu)$ is the probability/s that a molecule in state 2 exposed to radiation of spectral density $\rho(\nu)$ emits a quantum $h\nu$ and pass to state 1 [33].

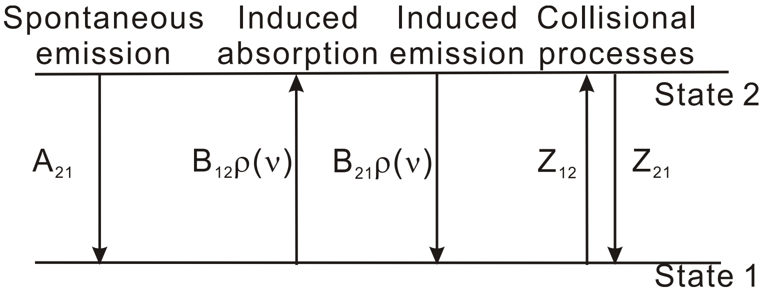

Fig. 6: Transition probabilities between states 1 and 2

At equilibrium the rate of change of number density in any state is zero. For example, the rate of the molecules which enter state 1 equals the rate of the molecules leaving state 1,

$$N_2\big(A_{21} + B_{21}\rho(\nu)\big) - N_1 B_{12}\rho(\nu) = 0 \tag{13}$$

which yields

$$\frac{N_2}{N_1} = \frac{B_{12}\rho(\nu)_{eq}}{A_{21} + B_{21}\rho(\nu)_{eq}} \tag{14}$$

On the other hand, the ratio of the number density between the two quantum states can also be expressed with the Boltzmann fraction

$$\frac{N_2}{N_1} = \frac{g_2}{g_1} exp\left(-\frac{h\nu}{kT}\right) \tag{15}$$

Compare eq. 14 with eq. 15, $\rho(\nu)_{eq}$ will be obtained as

$$\rho(\nu)_{eq} = \frac{(A_{21}/B_{21})}{\frac{g_2}{g_1}\frac{B_{12}}{B_{21}} exp\left(-\frac{h\nu}{kT}\right) - 1} = \frac{(8\pi h\nu^3/c^3)}{exp\left(-\frac{h\nu}{kT}\right) - 1} \tag{16}$$

It follows that

$$A_{21} = (8\pi h\nu^3/c^3)B_{21} \tag{17}$$

$$g_1 B_{12} = g_2 B_{21} \tag{18}$$

When light enters a gas medium with differential length *dx*, the spectral absorbance α_ν is defined as the fraction of the incident light I_ν over the frequency range $[\nu, \nu + \delta\nu]$ that is absorbed; it can be also described as the product of absorption coefficient k_ν and length *dx* [33].

$$\alpha_\nu = -\frac{dI_\nu}{I_\nu} = k_\nu dx \tag{19}$$

the absorption coefficient can be expressed as

$$k_\nu = -\frac{dI_\nu}{I_\nu dx} \tag{20}$$

The change in intensity after transmitting the gas medium $(dI_\nu)\delta\nu$ is the net combination of the effects of absorption and emission [33]

$$(dI_\nu)\delta\nu = n_2 dx \cdot B_{21}\rho(\nu) \cdot h\nu - n_1 dx \cdot B_{12}\rho(\nu) \cdot h\nu \tag{21}$$

where n_1 and n_2 are the number densities in states 1 and 2, respectively.

Hence,

$$\frac{dI_\nu}{I_\nu dx} = \frac{h\nu}{c}\frac{1}{\delta\nu}[n_2 B_{21} - n_1 B_{12}] \tag{22}$$

therefore, k_ν can be described as

$$k_\nu = \frac{h\nu}{c}\frac{1}{\delta\nu} n_1 B_{12}\left(1 - exp\left(-\frac{h\nu}{kT}\right)\right) \tag{23}$$

The normalized line shape function is defined as

$$\phi(\nu) \equiv \frac{k_\nu}{\int k_\nu d\nu} \tag{24}$$

such that its integral over frequency is unity,

$$\int_{-\infty}^{\infty} \phi(\nu)\, d\nu = 1 \tag{25}$$

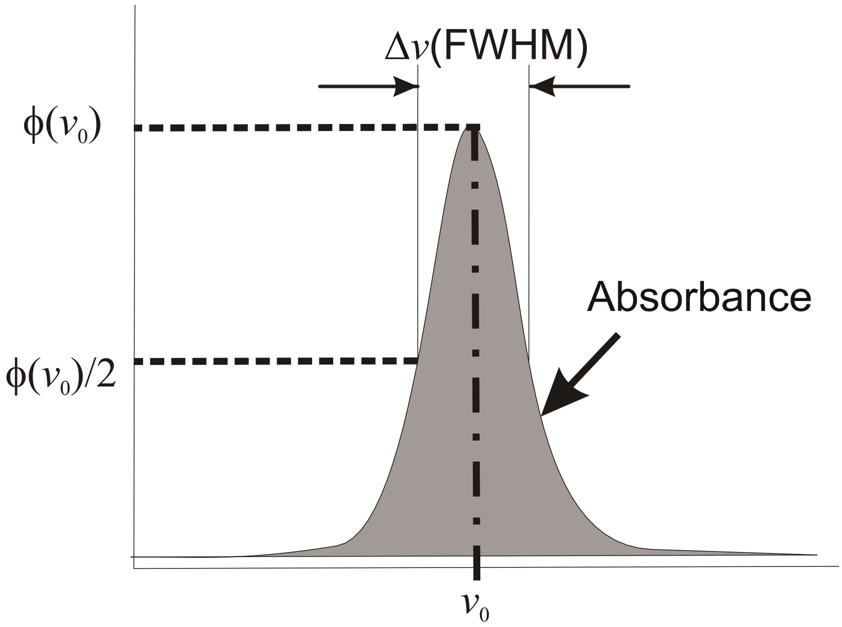

Fig. 7: The lineshape function for a transition located at ν_0

A typical lineshape of an isolated line centered at ν_0 is shown in Fig. 7. The lineshape function has a maximum value $\phi(\nu_0)$ at the line center, and the width of the line can be described by the full width at half maximum (FWHM) $\Delta\nu$.

For the frequency range $[\nu, \nu + \delta\nu]$, multiply $\phi(\nu)$ from eq. 13 to eq. 22 and k_ν can be expressed as when considering the line shape function [33]

$$k_\nu = \frac{h\nu}{c}\frac{1}{\delta\nu} n_1 B_{12}\left(1 - exp\left(-\frac{h\nu}{kT}\right)\right)\phi(\nu) \tag{26}$$

Integrating k_ν over the frequency range yields the line strength S_{12}

$$S_{12} \equiv \int k_\nu \, d\nu \tag{27}$$

$$S_{12} = \frac{h\nu}{c}\frac{1}{\delta\nu} n_1 B_{12}\left(1 - exp\left(-\frac{h\nu}{kT}\right)\right) \tag{28}$$

2.2.3 Beer-Lambert law

The typical setup of an absorption-spectroscopy experiment is sketched in Fig. 8. The laser is used as a radiation source, which sends a beam with the initial intensity I_0 through a gas medium with a path length L, and the transmitted light intensity I_t behind the gas medium can be recorded by a detector.

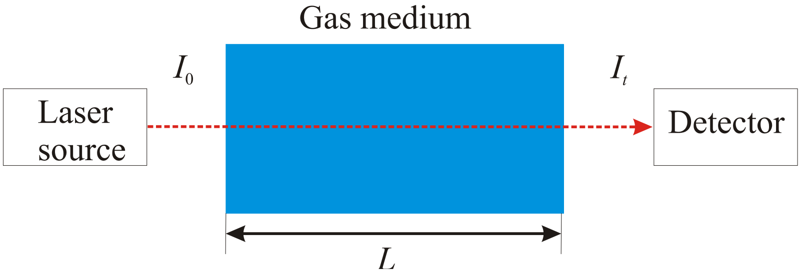

Fig. 8: Schematic of absorption-spectroscopy experimental setup

The basic law of absorption spectroscopy is the Beer-Lambert law

$$\tau = \frac{I_t}{I_0} = exp(-k_\nu L) = \exp\left(-n\sigma_\nu L\right) \tag{29}$$

where τ is the transmission, k_ν [cm^{-1}] is the spectral absorption coefficient, n is the number density of the absorbing species [molecules/cm^3] and σ_ν [cm^2/molecules] is the frequency-dependent absorption cross-section. For an isolated transition i,

$$k_\nu = px_{abs}S_i(T)\phi(\nu) \tag{30}$$

where p [bar] is the total pressure of the gas medium, x_{abs} is the mole fraction of the absorption species of interest, $\phi(\nu)$ is the lineshape function, $S_i(T)$ [cm^{-2}bar^{-1}] is the line strength of the transition at temperature T [K], which is only a function of T,

$$S(T) = S(T_0)\frac{Q(T_0)}{Q(T)}\left(\frac{T_0}{T}\right) exp\left[-\frac{hcE''}{k}\left(\frac{1}{T}-\frac{1}{T_0}\right)\right]\frac{1-exp\left(\frac{hc\nu_0}{kT}\right)}{1-exp\left(\frac{hc\nu_0}{kT_0}\right)} \tag{31}$$

k is Boltzmann’s constant, ν_0 is the center frequency of the transition, $S(T_0)$ denotes the line strength at a reference temperature T_0 (296 K), Q is the partition function and E'' is the lower-state energy of the quantum transition. These parameters at reference temperature can be measured in a reference cell or obtained from the HITRAN database [16-17]. The last ratio of eq. 31 can be neglected in a small temperature and frequency range.

The partition function of water vapor can be described over a range of temperatures by a third-order polynomial fit to a calculated partition function summation, the coefficients of the polynomial expression a_Q, b_Q, c_Q, and d_Q are listed in Table 1 [16].

$$Q(T) = a_Q + b_Q T + c_Q T^2 + d_Q T^3 \tag{32}$$

Table 1: Coefficients of the polynomial expression for the partition function of water vapor [16]

Coefficients	70 K < T < 405 K	400 K < T < 1500 K	1500 K < T < 3005 K
a_Q	-0.44405×10^{1}	-0.94327×10^{2}	-0.11727×10^{4}
b_Q	0.27678×10^{0}	0.81903×10^{0}	0.29261×10^{1}
c_Q	0.12536×10^{-2}	0.74005×10^{-4}	-0.13299×10^{-2}
d_Q	-0.48938×10^{-6}	0.42437×10^{-6}	0.74356×10^{-6}

Usually, the absorbance α_v can be described as

$$\alpha_v = -ln\left(\frac{I}{I_0}\right) = k_v L = p x_{abs} S_i(T) \phi(v) L \tag{33}$$

The integrated area A_i under the lineshape can be calculated as the integral of the absorbance,

$$A_i = \int_{-\infty}^{\infty} \alpha_v \, dv = p x_{abs} S_i(T) L \tag{34}$$

which is only related to the partial pressure px_{abs}, pathlength and the temperature depended line strength.

2.3 Line broadening mechanisms

The absorption lineshape broadening occurs when the absorbing molecules interact with light or the energy levels of the transition are perturbed by physical mechanisms [34-35]. The broadening mechanisms can be classified into two groups: homogenous broadening and in-homogeneous broadening. The homogenous broadening mechanisms affect all the molecules the same way. However, in the inhomogeneous broadening mechanisms, there are separate classes or subgroups for which the interaction varies. The most important broadening mechanisms are discussed below [33].

The Heisenberg uncertainty principle describes the relationship between the uncertainties of these energy levels with their lifetimes, the uncertainty in the energy level *i* is limited by

$$\Delta E_i \geq \frac{h}{2\pi\tau_i} \tag{35}$$

where τ_i is the lifetime of level *i*. The total uncertainty of a transition in units of frequency $\Delta\nu$ can be given by

$$\Delta\nu = \frac{1}{2\pi}\left(\frac{1}{\tau'} + \frac{1}{\tau''}\right) \tag{36}$$

where τ‘ and τ‘‘ are the lifetimes for the upper and lower states. Since the uncertainty is homogenous for all the molecules, the broadening is homogenous. The resulting lineshape function $\phi(\nu)$ can be derived as a form of Lorentzian function [36]:

$$\phi(\nu) = \frac{1}{2\pi}\frac{\Delta\nu}{(\nu - \nu_0)^2 + \frac{\Delta\nu}{2}^2} \tag{37}$$

where ν_0 is the line center. There are several different mechanisms which lead to line broadening. Three main types of broadening are described below.

2.3.1 Collisional broadening and shift

Collisional broadening is the other most important homogenous broadening mechanism. The lifetime of an energy state can be shortened because of perturbations that occur during collisions. According to eq. 36, the reduced lifetime leads to a broader linewidth. And it also can be expressed by a Lorentzian profile [36]:

$$\phi_C(\nu) = \frac{1}{2\pi}\frac{\Delta\nu_C}{(\nu - \nu_0 - \nu_S)^2 + \frac{\Delta\nu_C}{2}^2} \tag{38}$$

where $\Delta\nu_C$ is the collisional FWHM and $\Delta\nu_S$ is the pressure-induced frequency shift. If collisions occur between identical species this is called self-broadening, while when it takes place between different species it is called foreign broadening and needs to be known for each species *i*. Both $\Delta\nu_C$ and $\Delta\nu_S$ are proportional to pressure *p*

$$\Delta\upsilon_C = p\sum_i x_i\, 2\gamma_i \tag{39}$$

$$\Delta\upsilon_S = p\sum_i x_i\, \delta_i \tag{40}$$

where x_i is the mole fraction of the component i, and γ_i and δ_i are the collisional line broadening half-width and shifting coefficients due to the perturbation by the i^{th} component. The broadening coefficient γ_i is a function of temperature according to the following expression:

$$\gamma_i(T) = \gamma_i(T_0)\left(\frac{T_0}{T}\right)^{n_i} \tag{41}$$

$$\delta_i(T) = \delta_i(T_0)\left(\frac{T_0}{T}\right)^{m_i} \tag{42}$$

where T_0 is the reference temperature, n_i and m_i are the corresponding temperature-dependent coefficients which generally are determined experimentally.

2.3.2 Doppler broadening

Doppler broadening is the dominant inhomogeneous broadening mechanism. If the direction of a molecule’s (with mass m) velocity component is consistent with the light’s propagation path, there will be a frequency shift called Doppler shift. The values of velocities of molecules are described by the Maxwellian velocity distribution function. Each group of molecules with velocities in a small interval is considered part of a specific velocity class. The Maxwellian velocity distribution function describes the fraction of molecules in each class. The distribution function leads to a Doppler lineshape function ϕ_D with a Gaussian form:

$$\phi_D(\nu) = \frac{2}{\Delta\nu_D}\left(\frac{\ln 2}{\pi}\right)^{1/2} exp\left\{-4\ln 2\left(\frac{\nu-\nu_0}{\Delta\nu_D}\right)^2\right\} \tag{43}$$

the Gaussian lineshape at line center ν_0 is

$$\phi_D(\nu_0) = \frac{2}{\Delta\nu_D}\left(\frac{\ln 2}{\pi}\right)^{1/2} \tag{44}$$

where $\Delta\nu_D$ is the Doppler half width (FWHM) given by

$$\Delta\nu_D = \nu_0\left(\frac{8kT\ln 2}{mc^2}\right)^{1/2} \tag{45}$$

which also can be expressed as

$$\Delta\nu_D = \nu_0(7.1623\times 10^{-7})\left(\frac{T}{M}\right)^{1/2} \tag{46}$$

where ν_0 [cm^{-1}] is the wavenumber of the line center, T [K] is the temperature, and M [g/mole] is the molecular mass. When temperature increases the Doppler half width will be bigger, and hence, the line is broadened. Thus, the Doppler half width can be used to roughly calculate the gas temperature. Fig. 9 presents the increasing Doppler width with increasing temperatures between 300 and 1500 K for H_2O at 7185.59 cm^{-1}.

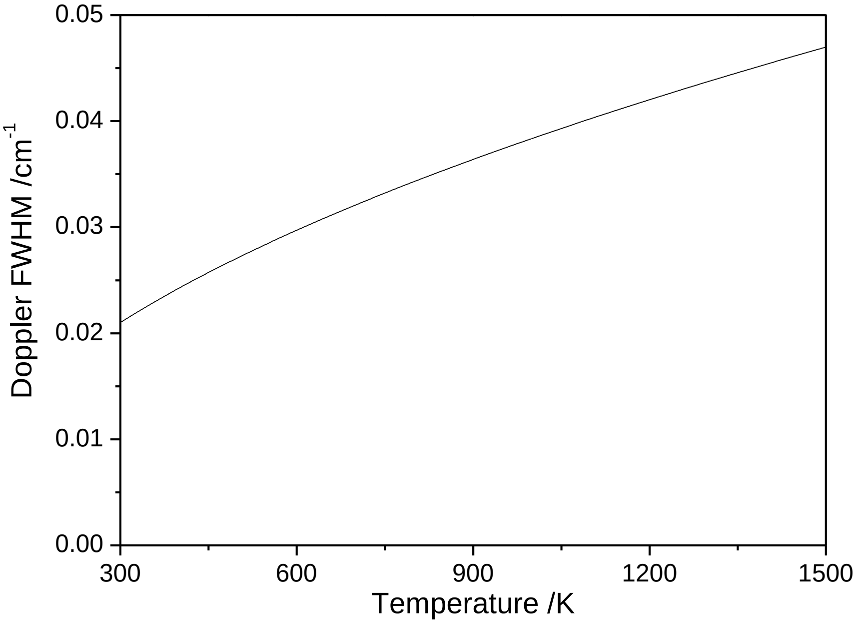

Fig. 9: Doppler width (FWHM) for H_2O with the transition at 7185.59 cm^{-1} as a function of temperature between 300 and 1500 K

Fig. 10 shows the comparison between the Gaussian and Lorentzian lineshapes when they have the same half width. The peak height of the Gaussian lineshape is larger than that of the Lorentzian profile, however, it drops much faster in the wings. If the Gaussian and Lorentzian lineshapes are normalized to the same area, the Gaussian profile also decays faster than the Lorentzian profile when moving away from the line center.

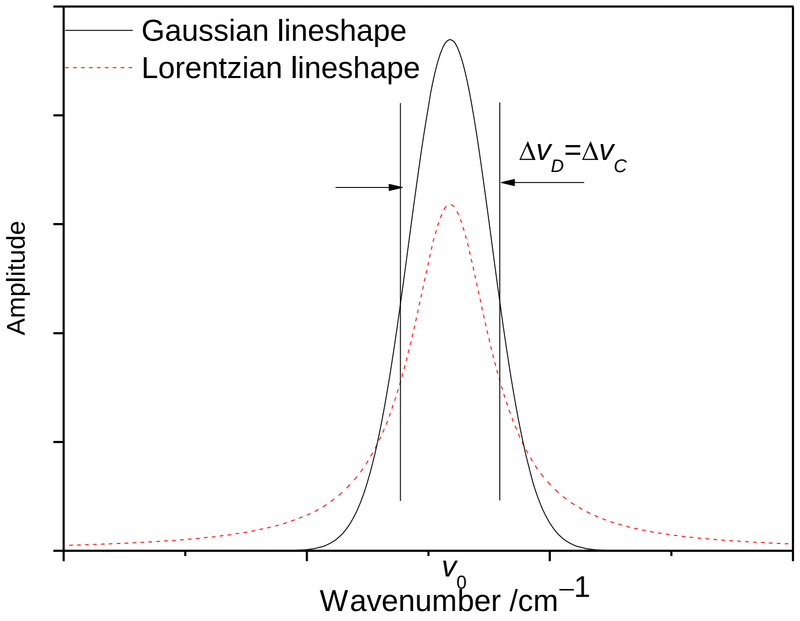

Fig. 10: Comparison of Gaussian and Lorentzian lineshapes with the same FWHM

2.3.3 Voigt profiles

Doppler broadening dominates at low pressures, while collisional broadening plays a more important role at high pressures. However, both mechanisms are significant at atmospheric conditions. The combination of both effects leads to a Voigt profile, which is a convolution of Lorentzian and Gaussian profiles [33]:

$$\phi_\nu(\nu) = \int_{-\infty}^{+\infty} \phi_D(u)\phi_C(\nu - u)du \tag{47}$$

The Voigt profile can be expressed as

$$\phi_\nu(\nu) = \phi_D(\nu_0)V(a, w) \tag{48}$$

$\phi_D(\nu_0)$ indicates the peak amplitude at line center of the Gaussian lineshape function, a is the Voigt parameter, which shows the relative significance of Doppler and collisional broadening

$$a = \frac{\Delta\nu_C\sqrt{\ln 2}}{\Delta\nu_D} \tag{49}$$

And w is the nondimensional distance line position

$$w = \frac{2(\nu - \nu_0)\sqrt{\ln 2}}{\Delta\nu_D} \tag{50}$$

The Voigt function *V*(*a*,*w*) can be determined by mathematical routines. A number of numerical approximations for the Voigt lineshape has been published before [37-38], one of the most common used assumption is the algorithm published by Humlicek et al. [39].

2.4 Direct absorption spectroscopy

There are typically two kinds of experimental methods for direct absorption spectroscopy: Fixed- and scanned- wavelength spectroscopy. Both of them have been widely used to measure a number of gas dynamic parameters, e.g. temperature, pressure, species concentration and flow velocity [4].

2.4.1 Fixed-wavelength absorption spectroscopy

In fixed-wavelength absorption spectroscopy, the laser wavelength is fixed at the center of an absorption line, or – if a broadband absorber is investigated – at a suitable position depending on other measurement issues. The laser beam is sent through the gas medium and the transmission is measured for a certain time period depending on the intended temporal resolution of data acquisition. The method is easy to design and it can also achieve high sensor bandwidth of several MHz in which allows the acquisition of highly transient events such as in IC engines [40]. The wavelength selection range of this technique is relative large by tuning the laser temperature while the laser current is constant. However, two aspects must be considered for this technique: one is non-resonant attenuation by unknown species or other effects (scattering, extinction, dirty optics, beam steering), and the missing lineshape information. In most practical environments, beam steering, window fouling and absorption by other liquid-phase species will cause non-resonant attenuation of the laser beam. Hence, an additional non-resonant laser must be combined to infer the non-absorbing baseline [40]. For the second aspect, as described above the lineshape of the absorption line depends on pressure, temperature and absorber concentration. These parameters and their effects on the lineshape need to be known beforehand for extracting meaningful quantitative information, i.e. concentration, from the measurement.

2.4.2 Scanned-wavelength absorption spectroscopy

The scanned-wavelength absorption spectroscopy will compensate the drawbacks of the fixed-wavelength absorption method [19, 41], and the schematic drawing of a typical scanned-wavelength absorption setup is shown in Fig. 11. The laser wavelength is rapidly current-tuned by a saw-tooth signal generated by a function generator. The laser output is separated into two parts by a splitter. The main portion of the beam is transmitted directly through the gas medium onto a detector. A typical measured signal as a function of time is shown in Fig. 12. A third-order polynomial is fitted to the baseline region of the signal as shown by the dotted line in Fig. 12, while the absorption spectrum (here as a function of scan time of the laser wavelength) will be obtained by subtracting the baseline. A fraction of the incident beam is sent through a Fabry-Perot interferometer (etalon), and the transmission is measured by a second detector.

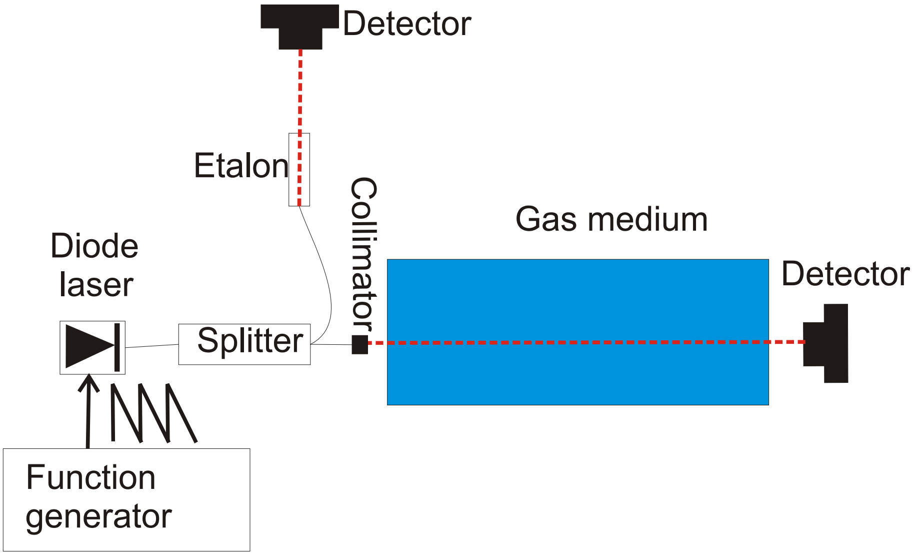

Fig. 11: Schematic drawing of a typical scanned-wavelength absorption experiment

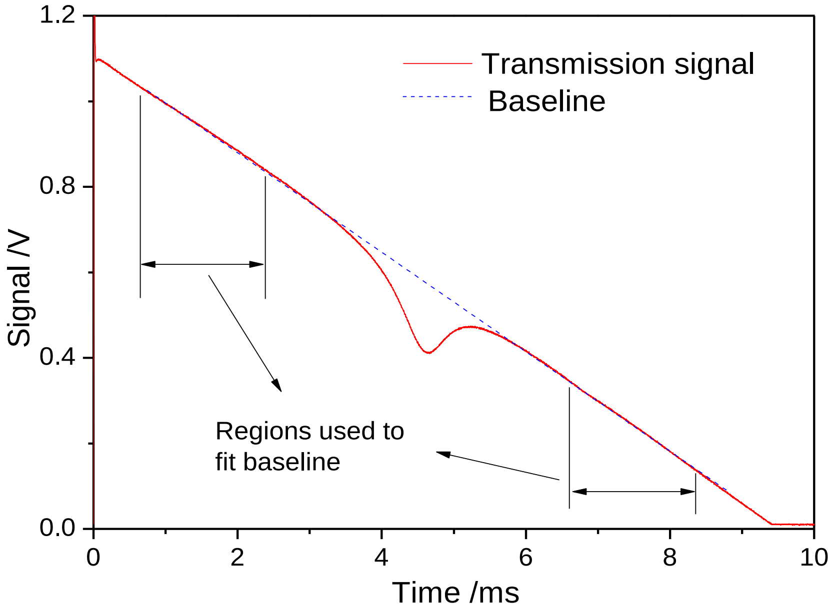

Fig. 12: Detected signal for a direct absorption scan near 1353 nm

A fiber-based interferometer (Micron Optics, FFP-I etalon) consists of a lensless plane-parallel Fabry-Perot interferometer with a single-mode optical fiber waveguide between two multilayer mirrors at a distance *d* and coated for high reflection within the laser tuning range. If the laser beam enters from one side, the multiple internal reflections between the inner surfaces of the two mirrors cause a standing wave [42]. The laser tuning causes an interference with fixed frequency spacing, which is the free spectral range (FSR):

$$FSR[\mathrm{cm}^{-1}] = \frac{1}{2nd} \tag{51}$$

where *n* is the refractive index of the material between these two surfaces.

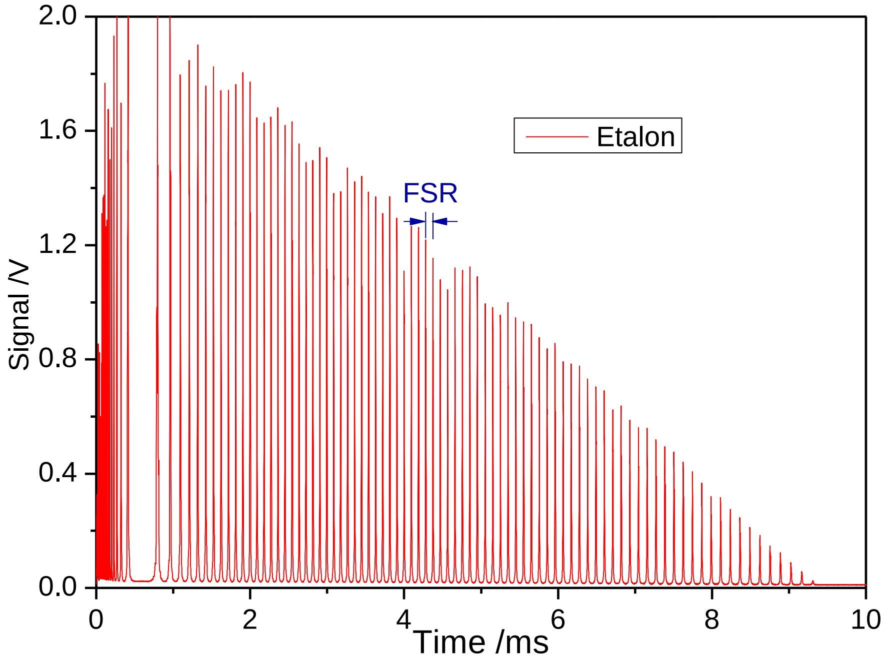

Fig. 13: Measured etalon transmission vs. time, i.e., wavelength

According to the known FSR, the transmission of etalon as a function of time (Fig. 13) can be used to obtain the temporal variation in frequency. The relationship between time and frequency can be determined by correlating the peak positions on the time scale with the frequency provided by given FSR. This information can be used for converting the time into a frequency scale as can be seen for the absorbance versus frequency plot of a water transition shown in Fig. 14. Subsequently, the measured lineshape of the determined absorbance is fitted by a Voigt profile, and the integrated area *A* is used to calculate the temperature (see following section) or species concentration.

For the DFB diode laser used in this work the current-tuning range is ~2 cm^{-1}. Due to the limited tuning range a fully resolved lineshape can only be obtained at low pressures. However, it is difficult to fit the baseline at high pressure conditions where the line is overlapped with neighboring lines, where the fixed-wavelength spectroscopy method is more advantageous. Meanwhile, the laser scan range also decrease with increasing laser repetition rate, the application in some extra high transient event will be restricted.

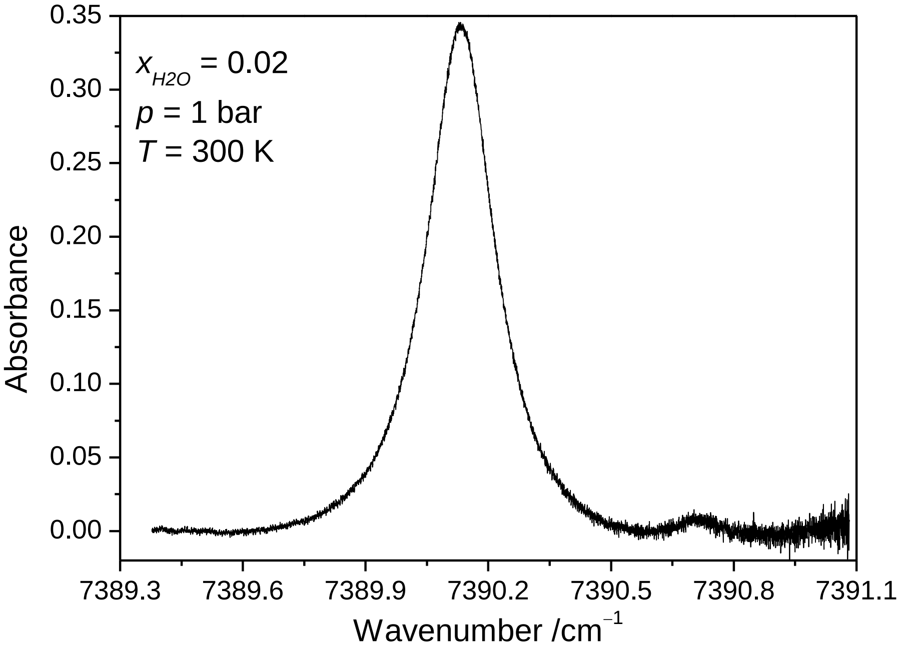

Fig. 14: Absorbance vs. frequency determined from a direct absorption scan of water vapor near 1353 nm

2.5 Absorption-based thermometry

Temperature is a fundamental parameter in combustion systems. Several methods have been used to determine the temperature, including the thermometer, thermocouples and laser-based diagnostics. The absorption-based thermometry is one of the non-intrusive diagnostic methods, which is widely used to infer the gas-phase temperature and species concentration because of the advantages of high sensitivity, robustness and fast response, etc. [4, 43]. For the case of a homogenous temperature field along the line-of-sight of the laser beam the two-line thermometry technique can be applied. The temperature can be determined by comparing the line strengths between two different transitions with different temperature dependence (different lower state energy *E”*). For the case that the temperature along the laser beam is spatially not homogeneous distributed, the temperature binning technique is used to determine the temperature length fraction along the laser beam with several estimated temperature bins [44].

2.5.1 System with homogenous temperature distribution

In the fixed-wavelength absorption technique the laser wavelength is fixed at the line center of the transition. The peak absorbances (peak height, $H_{1,2}$) at the line center of the two transitions are then measured (Fig. 15). The ratio between the two heights can be expressed as the ratio of the spectral absorption coefficients,

$$R = \frac{H_1}{H_2} = \frac{k_{v1}}{k_{v2}} = \frac{p x_{abs} S_1(T) \phi(\nu_1) L}{p x_{abs} S_2(T) \phi(\nu_2) L} = \frac{S_1(T) \phi_{v1}}{S_2(T) \phi_{v2}} \tag{52}$$

The ratio not only is a function of temperature, but also related to the mole fraction and pressure, since the lineshape function is involved. However, in order to simplify the technique, the two transitions are usually chosen to have similar lineshape functions such that their peak height ratio is insensitive to mole fraction [12]. A calibration database of the peak height ratio versus temperature and pressure can be calculated with some given mole fraction. Once the pressure is known in the system, comparison of the measured peak height ratio with the one in the calibration database can infer the temperate.

Once the temperature is known the mole fraction of the absorbing species can be determined from the peak height of one of the transitions,

$$x_{abs} = \frac{H}{p \phi(\nu) S(T) L} \tag{53}$$

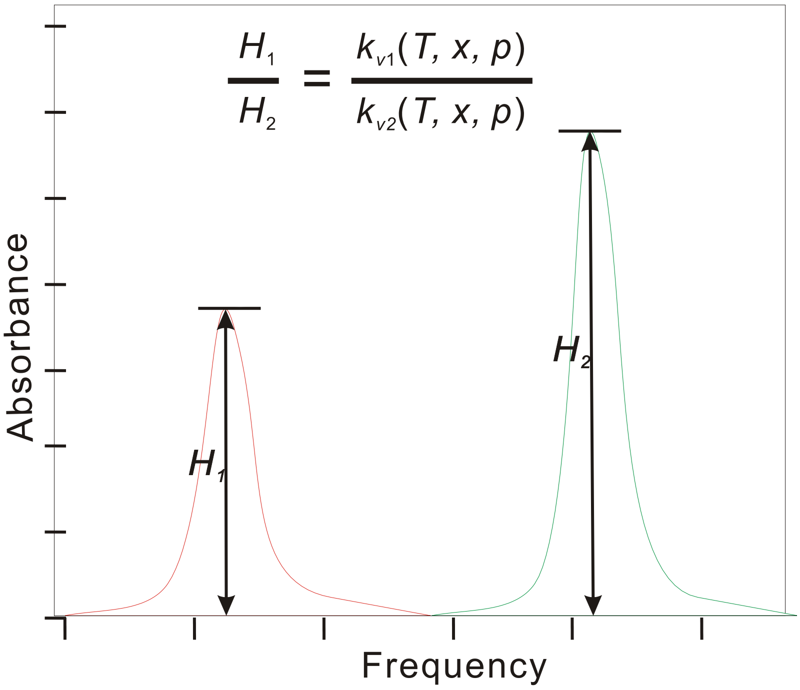

Fig. 15: Fixed-wavelength two-line thermometry

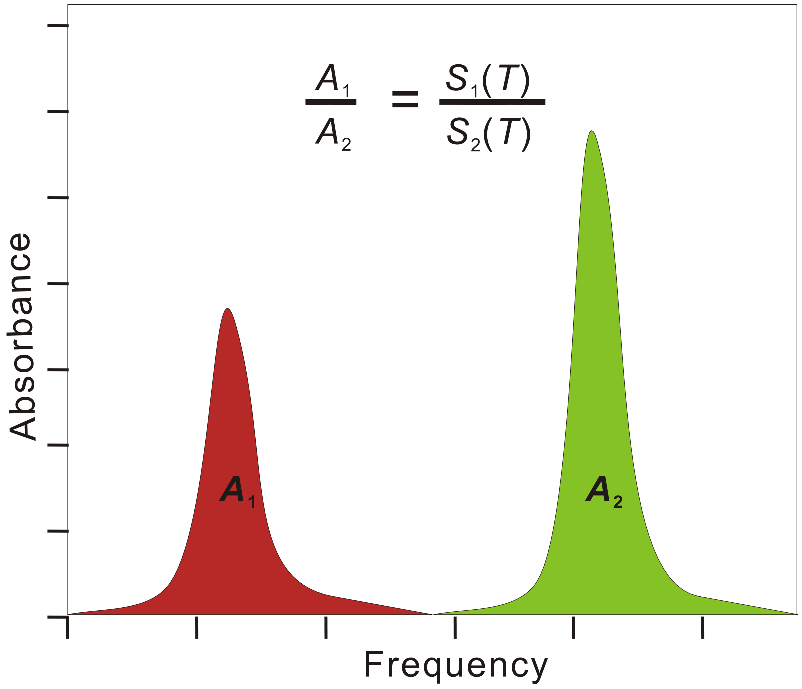

Fig. 16: Scanned-wavelength two-line thermometry

In the scanned-wavelength absorption technique, the integrated areas of the two lines shown in Fig. 16 can be simplified to the ratio of line strengths, since they have been measured simultaneously with the same pressure, mole fraction and path length, which is only a function of temperature. The line strengths of a pair of transitions versus temperature are plotted in Fig. 17, together with their ratio [12]. Thus, the absorbance ratio can be reduced to

$$R = \frac{A_1}{A_2} = \frac{S_1(T)}{S_2(T)} = \frac{S_1(T_0)}{S_2(T_0)} exp\left[-\frac{hc}{k}\left(E_1'' - E_2''\right)\left(\frac{1}{T} - \frac{1}{T_0}\right)\right] \tag{54}$$

The relative sensitivity of the ratio to temperature can be determined by differentiating eq. 54 [12]:

$$\left|\frac{dR/R}{dT/T}\right| = \left(\frac{hc}{k}\right)\frac{\left|E_1'' - E_2''\right|}{T} \tag{55}$$

It can be seen from this equation that a line pair with a large difference in lower state energy will have high temperature sensitivity.

The gas temperature can be obtained as

$$T = \frac{\frac{hc}{k}\left(E_1'' - E_2''\right)}{\frac{hc}{kT_0}\left(E_1'' - E_2''\right) + ln\,R + ln\frac{S_1(T_0)}{S_2(T_0)}} \tag{56}$$

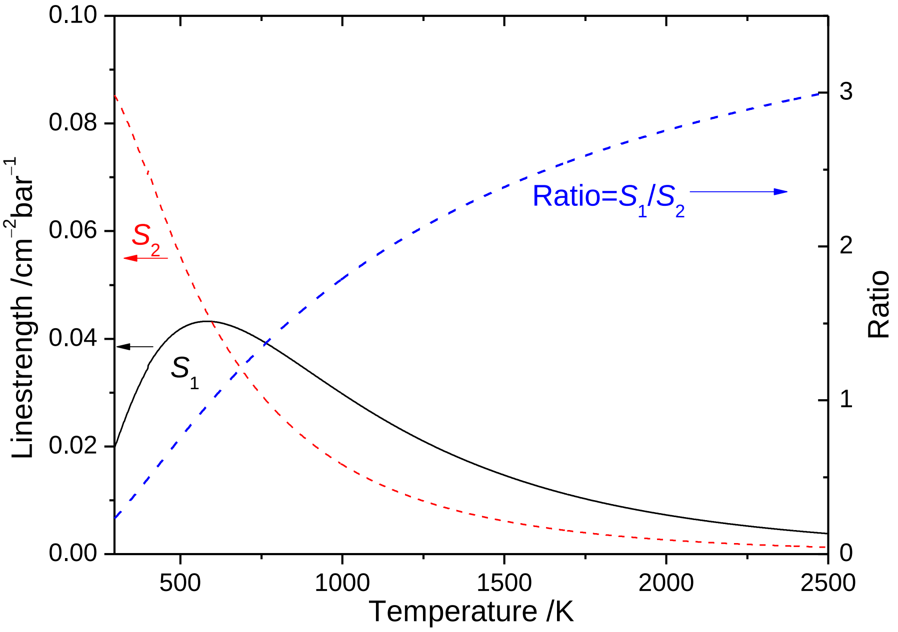

Fig. 17: Line strengths of two lines and their ratio as a function of temperature

The mole fraction of the absorbing species can be determined from the integrated area from one of the transitions,

$$x_{abs} = \frac{A}{pS(T)L} \tag{57}$$

Since temperature can be inferred from two properly chosen absorption transitions, combination of additional absorption lines could improve the temperature sensing range with reasonable sensitivity [40]. When simultaneously measuring three more absorption transitions with different lower state energies *E”*, the sensing range of the system can be increased. This will be discussed in chapter 3 in detail.

2.5.2 System with inhomogeneous temperature distribution

In many practical environments the temperature varies along the line-of-sight due to flow boundary layers [45], flow mixing, heat transfer to neighboring walls, or because the beam travels through, e.g., reaction zones within flames. Several techniques have been developed to infer the non-uniformities along the laser beam [46-48]; the strategy used in the present thesis is the temperature-binning technique [44].

In this method, the absorbing beam path is divided into *n* sections, for each section of length L_i, a uniform temperature T_i, mole fraction $x_{abs,i}$ and pressure p_i are assumed. For *m* selected transitions, the following equation can be derived from eq. 34

$$\begin{bmatrix} S_1(T_1) & S_1(T_2) & \dots & S_1(T_n) \\ S_2(T_1) & S_2(T_2) & \dots & S_2(T_n) \\ \vdots & \vdots & \vdots & \vdots \\ \vdots & \vdots & \vdots & \vdots \\ S_m(T_1) & S_m(T_2) & \dots & S_m(T_n) \end{bmatrix} \cdot \begin{bmatrix} (px_{abs}L)_1 \\ (px_{abs}L)_2 \\ \vdots \\ (px_{abs}L)_n \end{bmatrix} = \begin{bmatrix} A_1 \\ A_2 \\ \vdots \\ \vdots \\ A_m \end{bmatrix} \qquad (58)$$

If the individual temperatures (T_1, T_2, … T_n) along the beam path are estimated, the line strength matrix, which only is a function of temperature, can be calculated. The vector of absorbances A_i is the measured quantity. If the number of the selected absorption transitions *m* is larger than the number of temperature bins *n*, the equation can be solved unambiguously by a non-negative constrained least-square algorithm, which minimizes the following expression [44].

$$\min_{(px_{abs}L)_j} \sum_{i=1}^{m} \left(\sum_{j=1}^{n} S_i(T_j) \cdot (px_{abs}L)_j - A_i \right)^2 \qquad (59)$$

with

$$(px_{abs}L)_j \geq 0 \; (j = 1, 2, \dots, n) \qquad (60)$$

When the pressure and mole fraction are assumed uniform along the beam path, the length fraction f_j for each temperature bin can be calculated,

$$f_j = \frac{(px_{abs}L)_j}{\sum_{\mathrm{j=1}}^{\mathrm{n}} (px_{abs}L)_j} = \frac{L_j}{L} \qquad (61)$$

3 Sensor design

A suitable sensor design is the first step in absorption-based thermometry. This chapter first discusses the basic structure and fundamental vibrational modes of water and an overview of known water-vapor absorption lines in the HITRAN ([16]) spectroscopic database. The carbon dioxide absorption spectrum is also described. Then optimal line pair selection rules are presented, and the multiplexing techniques for multi-line two-line thermometry are also described. Finally, the 1.4 µm sensor used in the present work and the 2.7 µm laser applied in future work are introduced.

3.1 Water vapor

Water (H_2O) is one of the most important molecules in life. It is presented in three different states of aggregation on earth: liquid (e.g., seawater), solid (e.g., ice) and gas (e.g., water vapor). The water molecule has one oxygen and two hydrogen atoms connected by covalent bonds.

Water vapor is the main product in hydrocarbon combustion, and mainly shows strong absorptions in the infrared region. Thus many spectroscopic sensors developed before [49-51], including the one in this thesis focused on probing the water transitions. H_2O is a nonlinear triatomic molecule, which has three fundamental vibrational modes. The structure of H_2O and its fundamental vibrational modes v_1, v_2, v_3 are shown in Fig. 18. v_1 (3652 cm^{-1}) is the symmetric stretch mode, v_2 (1595 cm^{-1}) is the symmetric bend mode, and v_3 (3756 cm^{-1}) is the antisymmetric stretch mode [34]. Rotations are more complicated and there are interactions between the fundamental vibrations. Rotations about the three spatial axes are possible.

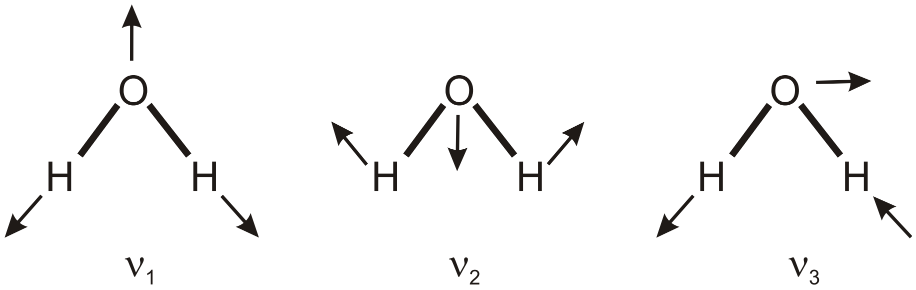

Fig. 18: The structure of water vapor and its three fundamental vibrational modes

The HITRAN (high-resolution transmission) molecular absorption database is a compilation of spectroscopic parameters from various molecules that can simulate the transmission and emission of light in the atmosphere [16-17]. The database has been developed over 40 years since 1960's by Rothman et al. and it provides spectroscopic parameters including the line-center frequency ν_0 [cm^{-1}], lines strength S [cm^{-2}/bar], lower state energy E" [cm^{-1}], air-broadening half-width γ_{air} [cm^{-1}bar^{-1}], temperature-dependent exponents n_{air} [–], self-broadening coefficients γ_{self} [cm^{-1}bar^{-1}] and air-induced frequency-shift coefficients δ_{air} [cm^{-1}bar^{-1}]. There are more than 2.7 million spectral lines for 39 different molecules in the HITRAN 2008 database [17]. However, the HITRAN database only contains data relevant to atmospheric conditions where temperature ranges between 200 and 350 K. Hence, a high temperature molecular database (HITEMP) was developed for improvement of data taken in high temperature applications, e.g. combustion processes, exhaust plumes, etc. It is analogous to HITRAN but encompasses many more bands and transitions than HITRAN [52]. There are more than 114 million water lines in HITEMP 2010. The line-by-line data, including the important spectroscopic parameter can be manipulated by the JavaHAWKS (HITRAN atmospheric workstation) software which is used to improve the cross-platform compatibility [53].

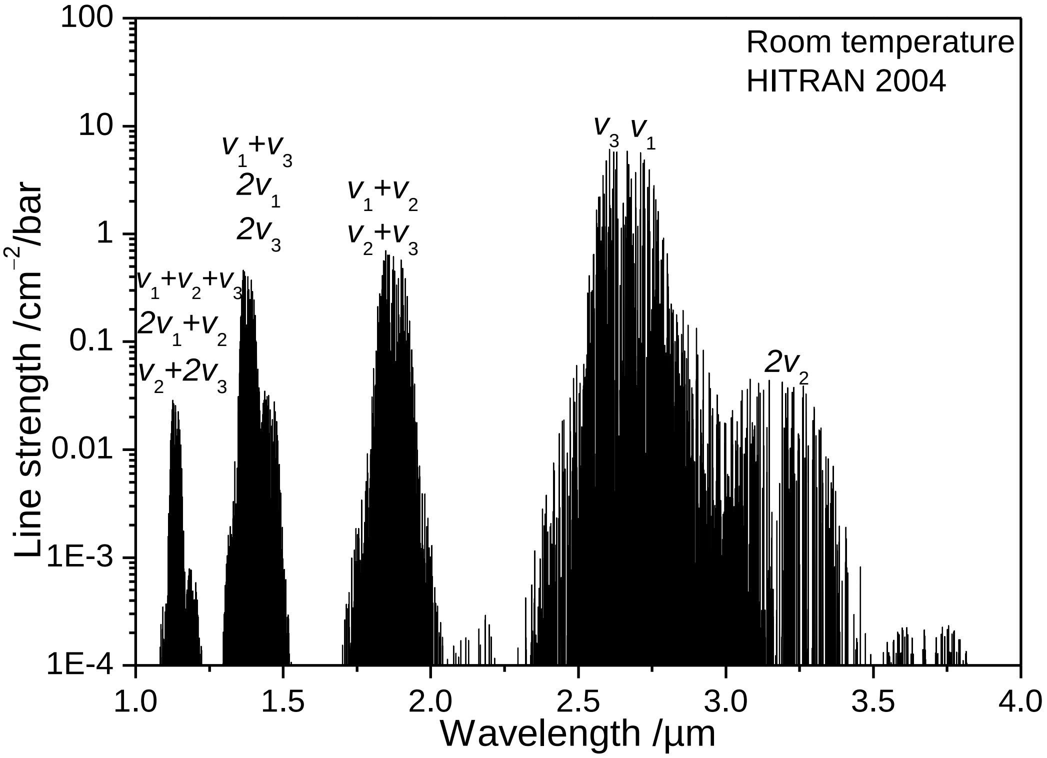

Fig. 19: Absorption spectrum of water vapor at room temperature from 1 to 4 µm based on HITRAN 2004 database

Since the water molecule has very small moment inertia, there are a large number of narrow-band and closely spaced rovibrational absorption lines. In Fig. 19, the water vapor absorption lines at room temperature from 1 to 4 µm based on the HITRAN database are plotted. The $2\nu_1$, $2\nu_3$ and $\nu_1+\nu_3$ absorption bands in the NIR region are popular for the sensor development since fiber-based, single-mode tunable diode lasers are commercially available in that wavelength range. Several researchers have chosen proper line pairs in this region to infer gas-phase temperatures [54-55]. The selection strategies will be discussed in the next section. It is also shown in Fig. 19 that in the region of the v_1, v_3 fundamental bands in the mid-infrared (MIR) region, e.g. around 2.7 µm, the corresponding line strengths are 20 times larger than in the NIR region. The transitions in this region are optimal to be used in the application with low absorber concentration or short path lengths.

3.2 Carbon dioxide (CO_2)

CO_2 is also the main product in hydrocarbon combustion. It is a linear triatomic molecule and its fundamental vibrational modes v_1, v_2, v_3 are shown in Fig. 20. v_1 (1330 cm^{-1}) is the symmetric stretch mode. Since there is no dipole moment for this mode since the two C-O bonds are compressed and stretched simultaneously, no direct light interaction (i.e., absorption or emission) is possible. Thus, “symmetric stretch” vibration for CO_2 is “infrared inactive”. v_3 (2349 cm^{-1}) is the asymmetric stretch mode. One bond is compressed while the other is stretched. v_2 (667 cm^{-1}) is the symmetric bend mode [33].

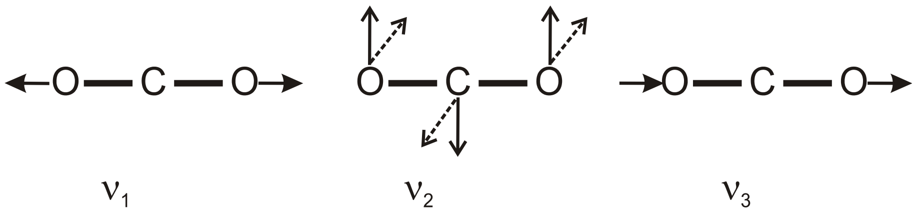

Fig. 20: The structure of CO_2 and its three fundamental vibrational modes

CO_2 has a rich absorption spectrum in the MIR region. The absorption spectrum of CO_2 at room temperature from 2.5 to 3 µm based on HITRAN database is shown in Fig. 21. However, the CO_2 absorption spectrum (black color) strongly overlaps with the water vapor absorption spectrum (red color) in this region. Hence, line pairs should be carefully chosen in order to avoid water vapor interference.

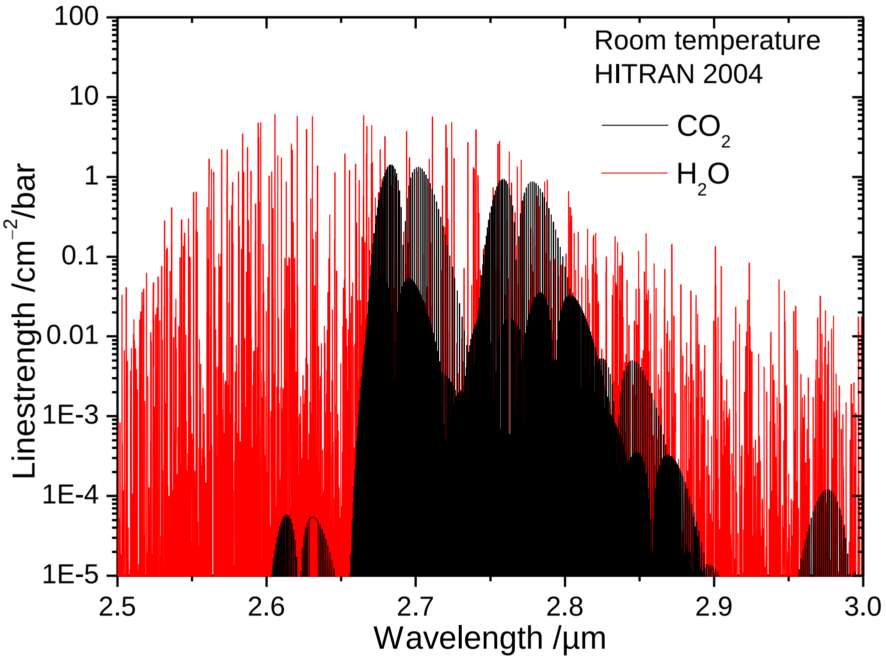

Fig. 21: Absorption spectrum of CO_2 and H_2O at room temperature from 2.5 to 3 µm based on HITRAN 2004 database

3.3 Line selection strategies

Since the absorption sensor used in this thesis operates around 1.4 µm in the NIR region, this section first focuses on describing the strategy of choosing proper line pairs between 1 and 2 µm for the conventional TDLAS two-line water vapor thermometry. The selection rules have been introduced by the group of Prof. Hanson at Stanford University, USA, and are summarized below [12,54]:

First, the selection of candidate H_2O lines should be limited to the spectral region of 1.25–1.65 µm, where H_2O absorption spectra overlap with the most common telecommunication bands, where optic fiber based diode lasers are widely available.

Second, both lines need sufficient absorption over the selected temperature range. A minimum detectable absorbance (noise level, NL) of 10^{-4} and a desired signal/noise ratio (SNR) of 10 are given. It is required that the peak absorption must be greater than (NL) × (SNR), that is 10^{-3}. However, the product should be less than 0.8 to avoid “optically-thick” measurements.

Third, the two lines should have sufficiently different lower state energy to make sure that the absorption ratio is sensitive to temperature. The larger the difference of the lower state energy is, the better is the temperature sensitivity (see. eq. 55). However, there are still two limitations. One is that lines with smaller E'' have large absorbance at cold boundary layers. The other is that lines with high *E*” always have very small absorbance, such that it is difficult to obtain a reasonable signal-to-noise ratio (SNR) with the smaller *E*” lines when building the ratio.

Fourth, both lines should be relatively free from interference of ambient H_2O and cold boundary layers. This can be achieved by using transitions with high ground-state energies. The two lines should also be free of significant interference from nearby transitions.

A single laser covering the wavelength range of two adjacent water lines with the above mentioned properties is optimal because of the simplicity of experimental setup. However, only few adjacent transition pairs exist which have proper spectroscopic parameters to enable sensitive temperature measurements. Zhou et al. has chosen a single laser at 1398 nm (denoted as laser 1) which was chosen here in a previous work [56] to measure the temperature in a premixed atmospheric-pressure burner. The spectroscopic parameters of the two transitions are shown in Table 2 [12].

The line strength of both lines of laser 1 are calculated with eq. 31 and shown in Fig. 22a. The temperature dependence reveals the change of ground-state population density with temperature, which was already introduced earlier. Since both of the lines reveal a lower state energy $E'' > 1700\ \mathrm{cm}^{-1}$, they are weak at low temperature and reach their maximum intensity around 1000 K. However, at low temperature, line 2 is significantly stronger than line 1, which results in a large variation of the ratio in this temperature range as shown in Fig. 22b. The ratio of line strengths is only a function of temperature. It is 10 around 500 K and decreases to 2 near 2500 K. The temperature sensitivity is related to the slope of the curve in Fig. 22b. The steeper the curve the larger is the sensitivity. However, in order to prevent one line dominating the ratio, both lines should have the same order of magnitude of absorption. The sensitivity of the line strength ratio to temperature is presented in Fig. 22b. It reveals that the laser is only sensitive in a limited temperature range between 700 and 1500 K.

It can be seen that a single laser may show a relatively high sensitivity in a specific temperature range, however, it does not provide high sensitivity in the whole temperature range of interest, e.g. 300 K to 3000 K. Therefore, several laser sources working in appropriate wavelength regions of suitable lines need to be operated simultaneously. The technique of wavelength-multiplexing overcomes the limitations in wavelength flexibility of using a single laser system. This way multiple transitions with different *E”* can be monitored simultaneously (s. chapter 3.4 below), and the temperature sensing range can be increased by combining different line pairs.

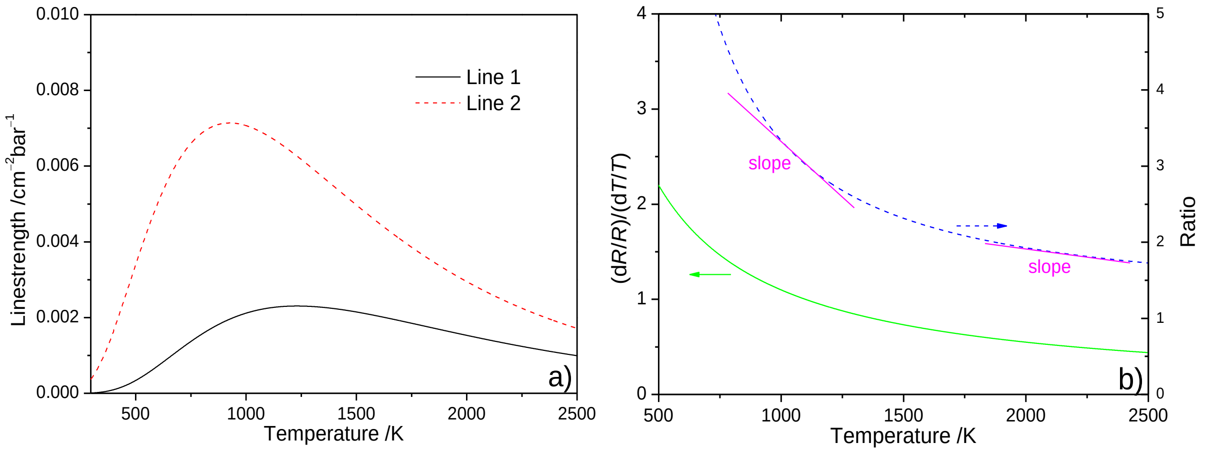

Fig. 22: Line strengths (a) and ratio (b) of line strength (blue dashed line) and its sensitivity (green line) vs. temperature for the lines 1 and 2 of laser 1 described in Table 2

Mattison et al. have set up a multiplexed diode-laser temperature sensor for measuring in a valveless pulse detonation engine [57]. At IVG such a system was used previously for temperature measurements in a shock tube [58]. The spectroscopic parameters of the used transitions are also listed in Table 2 (laser 1–4).

Table 2: Spectroscopic parameters of laser 1–4

Laser number	Line number	Line wavelength / nm	Line wavenumber / cm^{-1}	$S(T_0)$ / cm^{-2}/bar	E'' / cm^{-1}
1	1	1397.87	7153.75	8.05E–6	2552.9
1	2	1397.75	7154.35	3.67E–4	1789.0
2	3	1468.89	6807.83	1.02E–6	3319.4
3	4	1391.17	7185.59	1.97E–2	1045.1
4	5	1353.16	7390.13	8.53E–2	446.5

In Fig.23a, the line strengths of the three lines that can be scanned using lasers 2-4 are plotted. Line 3 has a maximum around 1500 K, and it is still significant up to 2500 K. Line 4 has a maximum line strength around 600 K. Line 5 is strong at low temperature, whereas it gets weaker at high temperature. The sensitivity of the ratio with respect to temperature of line strengths between the three lines are plotted in Fig.23b. It reveals that line pair 5 and 4 (black line) is optimal for low temperature measurements between 300 and 700 K, other two-line pairs have much broader sensitive temperature measurement range up to 2000 K.

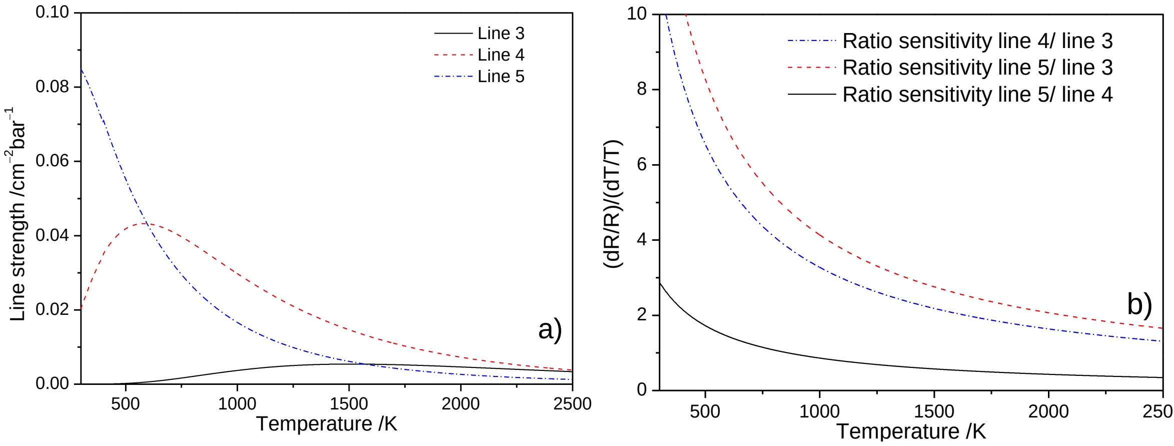

Fig. 23: Line strengths (a) and ratio sensitivity (b) vs. temperature for the lines 3–5 of laser 2–4 described in Table 2

In the following these four laser sources covering five transitions will be applied in a low-pressure reactor described in Chapter 4. Laser 3 and 4 will later further be applied for the liquid film measurement and introduced in Chapter 5.

3.4 Multiplexing techniques

The advantage of the wavelength-multiplexing technique has been introduced in the last section. Several lasers are combined together and transmitted along the same optical path. There are three different kinds of techniques usually used for this method: Time-Division Multiplexing (TDM), Frequency-Division Multiplexing (FDM) and Wavelength-Division Multiplexing (WDM). In order to simplify the description, for all the methods introduced below examples are restricted to two-line techniques. The FDM is typically used in modulation spectroscopy where the different wavelengths are modulated at different frequencies which is not used in the present thesis [59]. The other two methods are introduced in detail as below.

3.4.1 Time-division multiplexing

In TDM technique, two alternately scanned lasers are multiplexed and transmitted through the gas medium [20]. The transmitted laser beams are measured by one detector. The incident laser intensities of both lasers are shown in Fig. 24a, one laser is scanned at a specific time interval, and the other laser is kept below lasing threshold. The measured transmitted signal is shown in Fig. 24b.

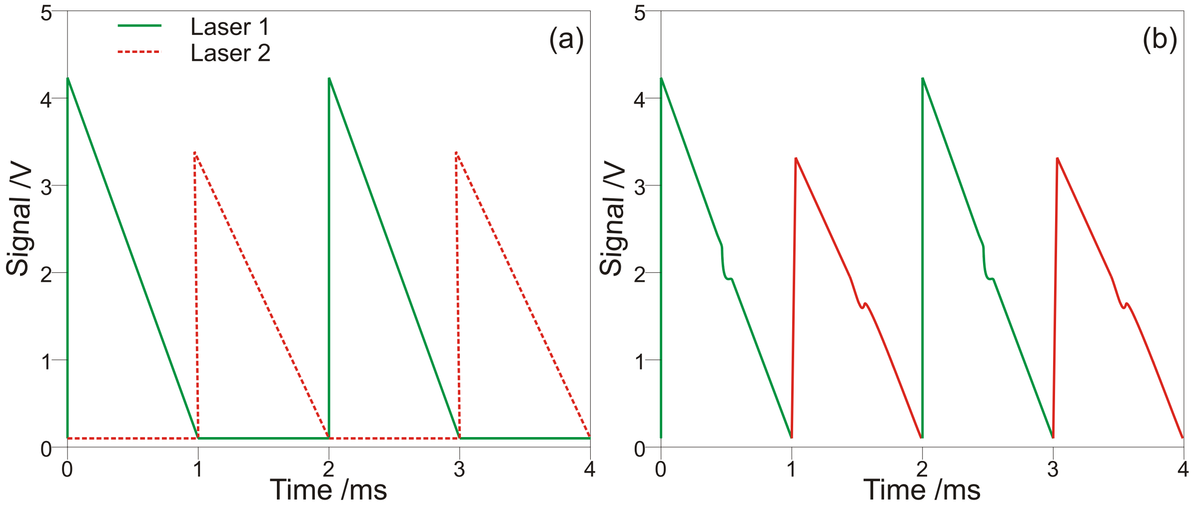

Fig. 24: The incident (a) and transmitted (b) laser intensities of TDM

The advantage of this technique is the simplicity of the optical setup, since only one detector is used. However, there are two drawbacks. One is that the laser intensities are not measured simultaneously. Therefore, the technique can only be applied in temperature steady environments, which will lead to large measurement uncertainties for the applications in highly transient events. The other drawback is that the sensor bandwidth is limited, since each laser is only scanned during a short time period. As will be discussed in Chapter 5, the TDM technique was used for water film thickness measurements in a flow channel.

3.4.2 Wavelength-division multiplexing

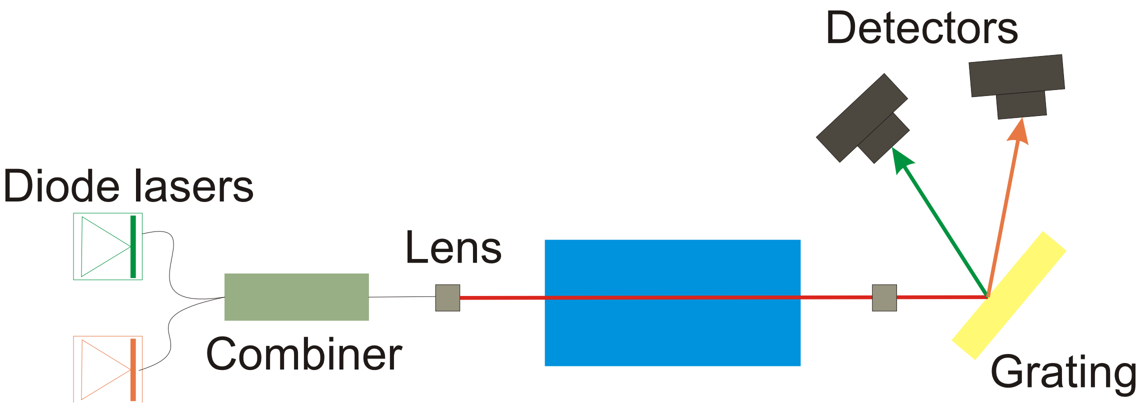

Fig. 25: Schematic of wavelength division multiplexing

In the present thesis the WDM technique is mainly used. The schematic drawing of the technique is shown in Fig. 25. Two different lasers are combined (usually by a fiber combiner), collimated and led through the gas sample, and the transmitted beams at different wavelengths are spatially separated by a diffraction grating [40]. In this technique, both lasers are tuned simultaneously by a continuous saw-tooth signal (shown in Fig. 26a). The transmitted intensities of each laser are detected by individual detectors and shown in Fig. 26b and Fig. 26c.

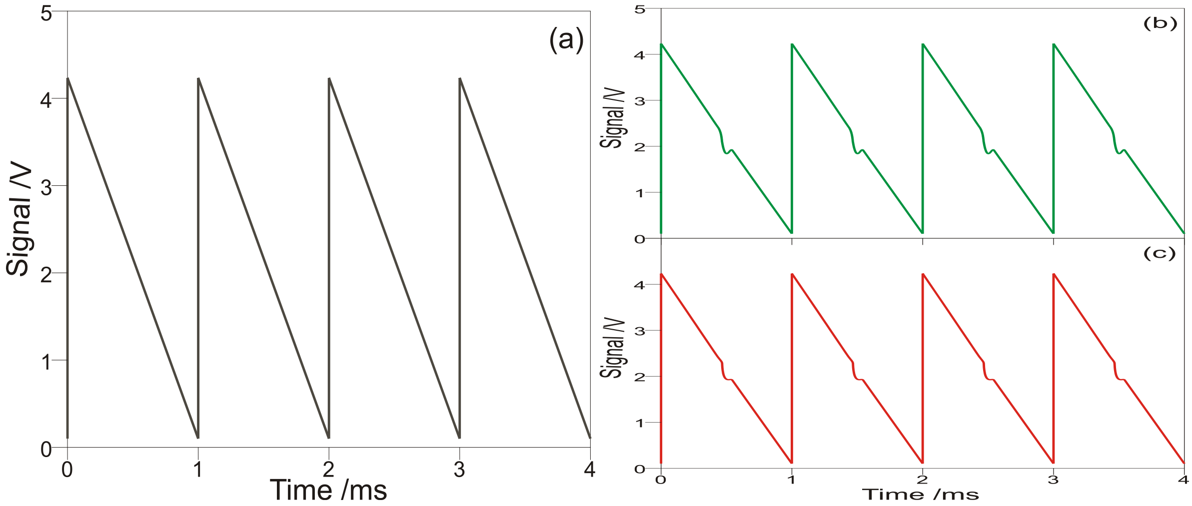

Fig. 26: The incident (a) and transmitted laser intensities of laser 1 (b) and laser 2 (c) of WDM

A diffraction grating is an optical component with parallel grooves with distance d_g, as shown in Fig. 27. The grating equation is given by

$$d_g(\sin\theta_m(\lambda) + \sin\theta_i) = m\lambda \tag{62}$$

where θ_i is the incident angle, θ_m is the diffracted angle, m is the order of diffraction and λ is the wavelength. The diffracted angle depends on wavelength. Thus, the multiple transmitted laser beams of different wavelength after diffraction will propagate in different directions and can be steered onto different detectors as shown in Fig. 25. It should be noticed that WDM cannot be used for a large number of wavelengths due to the overlap between different order reflections or the wavelength separation is geometrically insufficient.

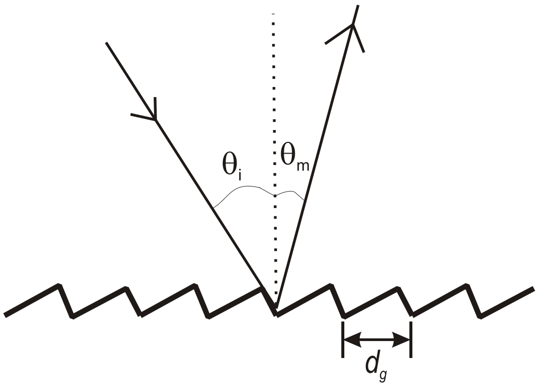

Fig. 27: Principle of a diffraction grating

3.5 Spectrometer design

3.5.1 1.4 µm spectrometer

As already discussed in section 3.1, water vapor has a relatively strong absorption spectrum near 1.4 µm which make the commercially available fiber-coupled NIR telecommunication lasers a low cost and simple in experimental setups. The 1.4 µm spectrometer in this thesis has been applied first in a low-pressure nanoparticle-synthesis reactor for temperature sensing and then for film thickness measurements, which will be described in detail in the next chapters.

The schematic drawing of the 1.4 µm fiber-based four-wavelength-multiplexed diode laser absorption sensor is illustrated in Fig. 28. The four fiber-pigtailed DFB diode lasers with 14-pin butterfly package (NEL) are multiplexed into a single-mode fiber (9 µm core diameter) using a 4 × 1 fused combiner (Laser 2000). The multiplexed light is first passed through a Faraday isolator (Laser 2000), which is capable of reducing light back-reflections into the laser diode by ~50 dB. The light is collimated by an aspheric lens (Thorlabs, F230FC-C), and steered through the absorbing medium. After that, the light is caught using another aspheric collection lens and focused into a multi-mode fiber (Thorlabs, BFL37-400). The multi-mode fiber (400 µm core size) has a larger core diameter than the sending single mode fiber, which ensures higher collection efficiency. However, it leads to increased sensor noise due to fiber mode noise. Both fibers should be firmly fixed in a holder to minimize fiber movement to reduce the effects of fiber mode and polarization noise [40].

The multiplexed light is brought to another location via the multi-mode fiber where the light is demultiplexed (also see the photograph in the left corner of Fig. 28). Absorption of the beams by water vapor in ambient air is avoided by enclosing the whole demultiplexing optics in a nitrogen-purged box. As shown in Fig. 28, the light from multi-mode fiber is collimated using an aspheric lens (Edmund, diameter: 25 mm, focus length: 25mm) and then pitched onto a diffraction grating (Edmund) with a 10 mm beam diameter (1200 grooves/mm) used in first-order Littrow configuration. The individual wavelengths are diffracted at different angles (demultiplexed) and are then focused onto InGaAs photo detectors (Thorlabs, PDA10CS-EC) using spherical focusing mirrors (diameter: 25 mm, focus length: 50 mm). The detectors have a large area (2 mm diameter) that can reduce the fiber mode noise since the entire laser beam can be focused onto the active area of the detector.

Fig. 29 shows a picture of function generator, laser controller, diode lasers and the fiber combiner. The diode lasers, function generator, laser controller, demultiplexing optics, detectors and data acquisition system are located on a movable table (Thorlabs), which enables convenient equipment transport to experiments situated at different places.

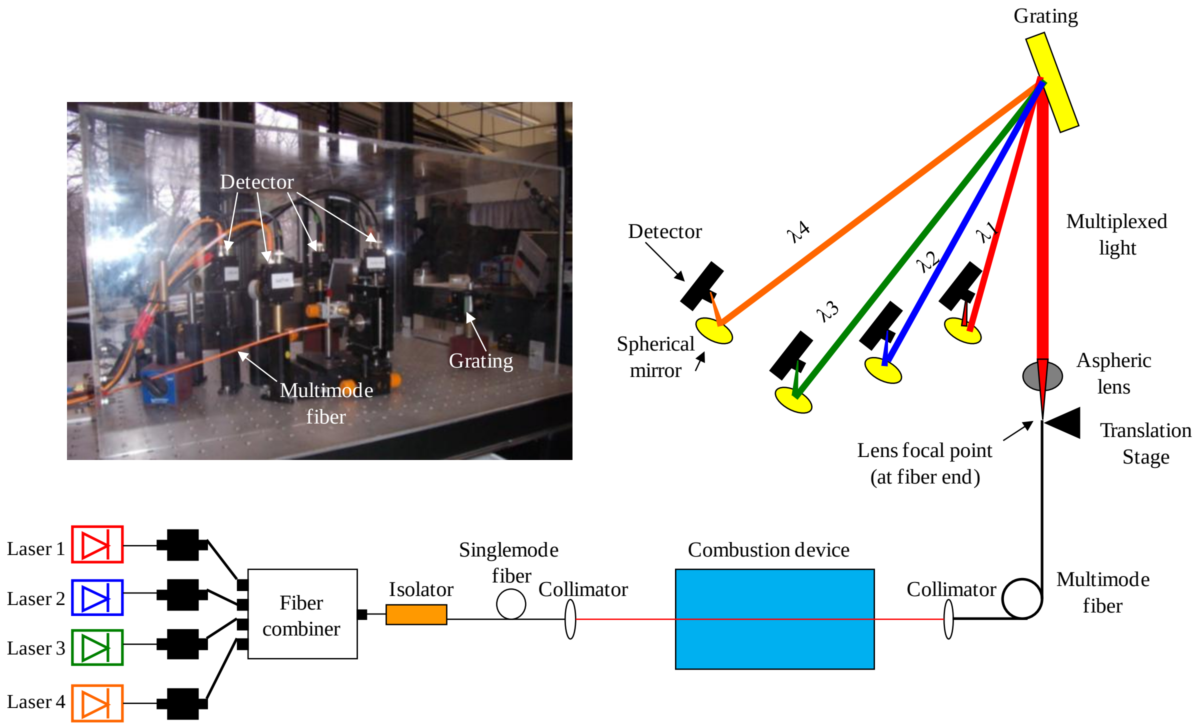

Fig. 28: Schematic drawing and photograph of a fiber-based wavelength-multiplexed diode laser sensor

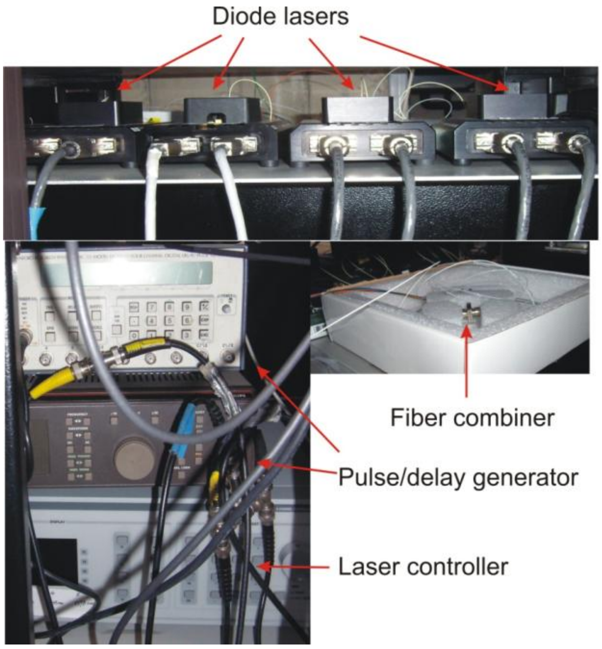

Fig. 29: Photographs of the components of the spectrometer

3.5.2 2.7 µm spectrometer

As mentioned in section 3.1, the line strengths of water vapor at 2.7 µm are much stronger than in the NIR region. However, since suitable optical fibers in this wavelength region are still missing, the system is no longer fiber-based thus increasing the complexity of laser alignment. Nanoplus GmbH provides compact DFB diode lasers up to 2.9 µm. This opens up the opportunity for measurements at short absorption path lengths and/or low absorbers concentrations. Wunderle et al. have used a DFB diode laser at 2761.97 nm (3619.611 cm^{-1}) for water vapor concentration measurements for absorption paths less than 10 cm [60]. Farooq et al. have set up a tunable diode-laser absorption sensor to monitor carbon dioxide (CO_2) near 2.7 µm for temperature measurements behind reflected shock waves in a shock tube [61].

For future experiments aimed at temperature measurements in shock tubes two CO_2 absorption lines were chosen at 2743.06 nm (3645.56 cm^{-1}) and 2752.48 nm (3633.08 cm^{-1}), respectively, based on the previous work by Farooq et al [62]. The simulated absorption spectrum of both lines at atmospheric pressure, and temperatures of 300, 1000 and 1500 K are plotted in Fig. 30a and b, respectively. The well isolated line at 3633.08 cm^{-1} (E" = 316.77 cm^{-1}) has strong absorbance at low temperature and decreases with increasing temperature. The line near 3645.56 cm^{-1} (E" = 1936.09 cm^{-1}) shows high sensitivity at higher temperature; however, it will lead to high measurement uncertainties at elevated pressure since the transition will be blended with nearby lines. The line strength ratio sensitivity of both lines is shown in Fig. 31. It shows that the line pair is sensitive in the temperature sensing between up to 2000 K.

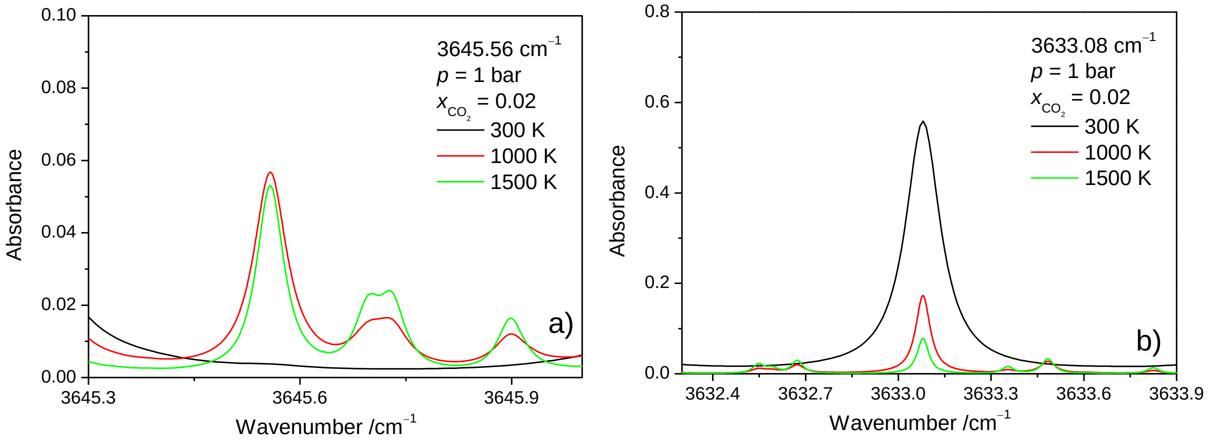

Fig. 30: Simulated absorption spectrum for CO_2 transitions near 3645.56 cm^{-1} (a) and (3633.08 cm^{-1}) (b)

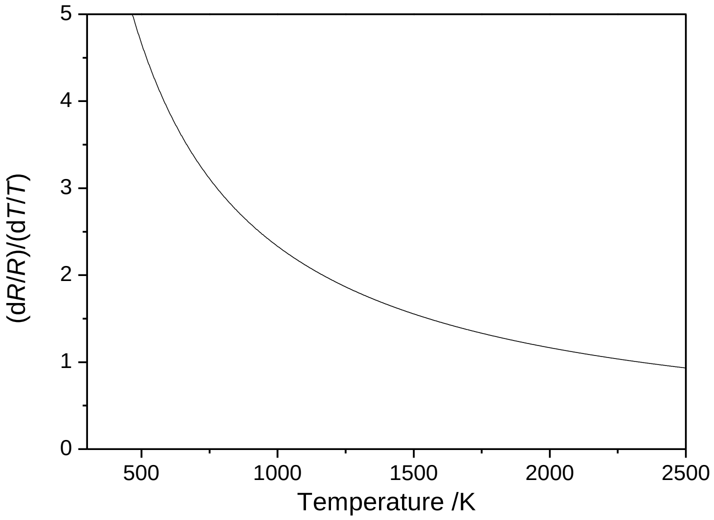

Fig. 31: Line strength ratio sensitivity between 3633.08 cm^{-1} / 3645.56 cm^{-1} vs. temperature

3.6 Literature review

In this thesis, multiplexed TDLAS sensors are developed for temperature measurements in a low-pressure flame reactor and for film thickness measurements, respectively. Therefore, a literature overview covering work of other groups in the design of multiplexed TDLAS sensors, and their studies on temperature measurements in non-uniform temperature-distributed systems is given here. In addition the importance of liquid film measurements, and results from liquid film and temperature measurements in other studies needs to be reviewed.

Many researchers have applied multiplexed TDLAS sensors for vapor-phase concentration and temperature measurements in combustion-related systems in the previous work. Mattison et al. used a multiplexed TDLAS spectrometer to measure crank-angle-resolved temperature and water concentration in a homogenous-charge-compression-ignition (HCCI) engine with wavelength-division multiplexing technique [40]. Baer et al. developed a multiplexed TDLAS sensor to simultaneously monitor several flow field constituents and properties along a single path to achieve combustion control, emissions monitoring, atmospheric studies and process control [63]. Ebert et al. demonstrated a spectrometer with two DFB diode lasers and one Fabry-Perot diode laser to simultaneously measure O_2, CH_4, CO_2, H_2O concentration and the temperature in order to ensure a safe ignition procedure of large-scare multi-burner gas-fired combustion systems [64].

A variety of studies have been done based on two-line thermometry for applications of temperature measurements in homogenous gas-phase distributed systems [12-13, 18-19]. For systems with inhomogeneous temperature distribution, Zhou et al. used a linear mixing model by assuming a trapezoidal-shaped temperature profiles to take into account the boundary layer effect in a Hencken burner [12], Palaghita et al. defined a non-uniformity variable based on the difference in temperatures measured with two pairs of absorption lines as well as by using several absorption lines to evaluate temperature non-uniformities [65]. Sanders et al. introduced a novel multi-line thermometry strategy and measured multiple O_2 absorption lines to determine the temperature distribution within an optical path through two static cells at different temperatures [44]. Liu et al. have improved the former multi-line thermometry with two different strategies, the profile fitting and temperature binning technique, and did several simulation studies and laboratory experiments [20]. The latter strategy is applied in this thesis.

Liquid film formation in the sub-millimeter thickness range is common in many practical applications. A quantitative measurement of liquid film thickness is helpful to optimize the operation of technical devices and to provide validation data for simulations of such processes. For instance, the characterization of fuel films is required in many situations of engine combustion: Fuel films may be formed on inner walls of the inlet port in port-injected gasoline engines (e.g. [66]), on piston heads in direct-injection spark-ignition (DISI) engines (e.g. [67]), or in the intake manifold during cold start [68]. The aim for improvement is to avoid wall wetting during fuel injection, thus increasing fuel efficiency and simultaneously decreasing pollutant (i.e., unburned hydrocarbon and soot) emissions. Water-based films or water mist diagnostics are of interest, e.g., in chemical industry [24], fire suppression [69], and, e.g. steam power generation [22]. In engine-related applications the observation of the dynamic behavior of liquid water films is also of interest during injection of water-urea solutions into the exhaust pipe for selective catalytic reduction (SCR) of NO_x [70], which motivates the present work of water-film measurements.

Because of their non-intrusiveness, in the past a number of optical techniques have been developed to measure liquid film thicknesses. Some of these make use of the relative intensity difference at the detector, of the totally and partially reflected light, respectively, inside the film as a measurement of film thickness. Hurlburt et al. used the technique of total internal reflection which occurs at a liquid-vapor interface due to the refractive index difference between the two phases. Film thickness was measured in a triangulation scheme where the lateral displacement of a laser beam; reflected off the liquid layer is observed by a camera [71]. Instead of a laser Shedd et al. directed light from a LED through the film-covered wall and also determined the displacement of the beam [22].

Spectroscopic methods have also been used for the measurement of fluid film thickness: The fluorescence emitted from hydrocarbon fuel films after excitation in the ultraviolet was exploited by Kull et al. for two-dimensional imaging [72]. Greszik et al. used a combination of LIF and spontaneous Raman scattering for imaging water film thickness [73]. The absorption of blue laser light in a dye-doped liquid was employed by Mouza et al. to measure the thickness of flowing films [23]. Porter et al. quantified the strong absorption bands around 3.4 µm of liquid hydrocarbon fuels [74] and used a mid-infrared laser-absorption sensor in this wavelength range to determine the thickness of liquid films of n-dodecane on transparent windows in the presence of n-decane vapor [75]. The absorption of near infrared (NIR) emission from a HeNe-laser was used by Wittig et al. to study the wall film behavior in the suction pipe of a spark ignition engine [21]. As mentioned in chapter 1, liquid film temperature measurements are also important. Schagen et al. has used a laser-induced luminescence technique to simultaneously determine the temperature distribution and film thickness in wavy liquid films [24], Alderfer et al. performed sub-microsecond temperature measurement in liquid water using laser-induced thermal acoustics [76].

In the present work, we apply the introduced temperature-binning technique [44] to resolve the non-uniform temperature distribution inside a low-pressure flat-flame reactor. Meanwhile, we setup a novel multi-line TDLAS sensor in the NIR region to simultaneous measure the liquid water film thickness, temperature and vapor-phase temperature above the film during film evaporation. To our knowledge, it is the first time to use diode laser absorption technique to measure liquid water film temperature.

4 Water-vapor temperature sensing in a low-pressure flame reactor

Two different diagnostic methods were compared to determine the spatially-resolved temperature information inside a low-pressure premixed-flame reactor for nanoparticle synthesis. One method is tunable diode laser absorption spectroscopy (TDLAS) of water vapor, where the temperature distribution can be obtained by assuming the temperature to be constant in variable lengths along the line-of-sight (LOS, section 2.5.2). The length fraction of postulated temperature bins along the LOS is determined. The TDLAS temperature binning technique is first validated on a premixed atmospheric-pressure burner that has a two-zone temperature distribution to infer the measurement accuracy and then applied in the lower-pressure reactor. In the reactor, the other method multi-line NO-LIF imaging was used to validate the spatial temperature distributions deduced from H_2O TDLAS.

4.1 Introduction

Nanosized semiconducting metal oxide particles including ZnO, SnO_2, and TiO_2 are widely used for gas-sensing devices, photocatalysis and (opto)electronic devices. A promising route for the synthesis of these particles is combustion synthesis from evaporated metal-organic precursors in low-pressure premixed flames [77]. Temperature is an important factor that influences the properties of the synthesized particles. Therefore, the temperature distribution inside the low-pressure premixed-flame reactor for nanoparticle synthesis must be known to simulate the particle formation and growth. For further studies, more specific information is of great interest, e.g. the effect of the three-dimensional structure of the flame (flame symmetry) on the particle growth process. Therefore, three-dimensional temperature distribution is necessary to be determined in such flames.

H_2O TDLAS

Laser-based diagnostic techniques are widely used for in-situ non-intrusive temperature measurements in flames [4]. In previous work TDLAS two-line thermometry with a single laser (laser 1) was used to infer the temperature inside the reactor [78]. This strategy can only provide LOS-averaged temperature information through the sample by assuming a homogenous temperature distribution along the path. In general, temperature varies along the beam path in the reactor due to inhomogeneous mixing flows, heat conduction near chamber walls, and boundary layer effects, etc. Previous research has been done to correct for such non-uniformities, e.g., the effect from boundary layers [45, 79], the sensitivities to flow non-uniformities

[80], and to infer the path-averaged temperature via different line pairs with different temperature sensitivities [81].

In this thesis the temperature binning technique first demonstrated by Sanders et al. [44] is applied to obtain the non-uniform temperature distribution inherent in the investigated reactor. As introduced in section 2.5.2, the length fraction in each specified temperature bin can be determined by postulated temperature bins with assumed known and uniform pressure and species mole fraction. However, no information is obtained with respect to the way in which the constant temperature sections are distributed along the beam path [44]. The technique has two main advantages: It is fast data evaluation process, because a system of linear equations is solved and only little knowledge of the temperature distribution in the system is required. The major drawback is that the result will be too coarse unless many bins are used. However, the number of probed transitions is limited by the number of laser sources, too many bins can result in an ill-conditioned problem (cf. chapter 2.5.2) [44].

The four DFB diode lasers (laser 1–4) employed here were used in our lab for previous work, e.g., temperature measurements in a flat-flame burner and a shock tube. They were first chosen by Mattison et al. [57] and have been listed in Table 2. The five water-vapor lines have lower state energies E” from 446.5 to 3319.4 cm^{-1} which are sensitive enough for the application in the reactor with a temperature range of 300–2000 K. The temperature distribution along the absorption path is obtained iteratively using estimated temperature bins along initially unknown length sections through the gas sample. From evaluating the temperature profile with this method at a fixed height position in the flame, TDLAS yields a coarse one-dimensional temperature profile that indicates the lengths of the paths within the different temperature regions but without information about their sequence and orientation. Here, we assume temperature is symmetrically monotonous distributed from the center towards the wall. Thus, by scanning the laser beam parallel to the burner plate a two-dimensional temperature distribution can be determined at a fixed height position in the flame. Repeating this procedure at different heights above the burner (HAB), three-dimensional temperature information can be finally obtained.

In Fig. 32, the simulated spectrum based on the spectroscopic parameters listed in HITRAN 2004 [16] for these five water vapor transitions with different temperature dependence (i.e., different lower state energy E”) for the conditions in the atmospheric pressure flame and the low-pressure reactor are plotted. The black lines are for the methane/air flame at atmospheric pressure (for water vapor mole fraction: 0.19, optical pathlength: 20 cm, temperature 1000 K). The red dashed lines are for the low-pressure flame reactor (for water vapor mole fraction: 0.30, optical pathlength: 40 cm, reactor pressure 30 mbar, temperature 1000 K). The simulation in the atmospheric-pressure burner shows that all five transitions show absorbance values that are larger than 5%. However, for the low pressure reactor, it reveals that water-vapor line 4 and 5 has absorbance values that are larger than 10%, whereas lines 1 and 3 are smaller than 5% since they are more sensitive at even higher temperatures. Liu et al. have developed an important line selection guideline for the temperature binning technique [20]. For instance, with a narrow range of *E”* will not guarantee a good least square fitting for eq. 58.

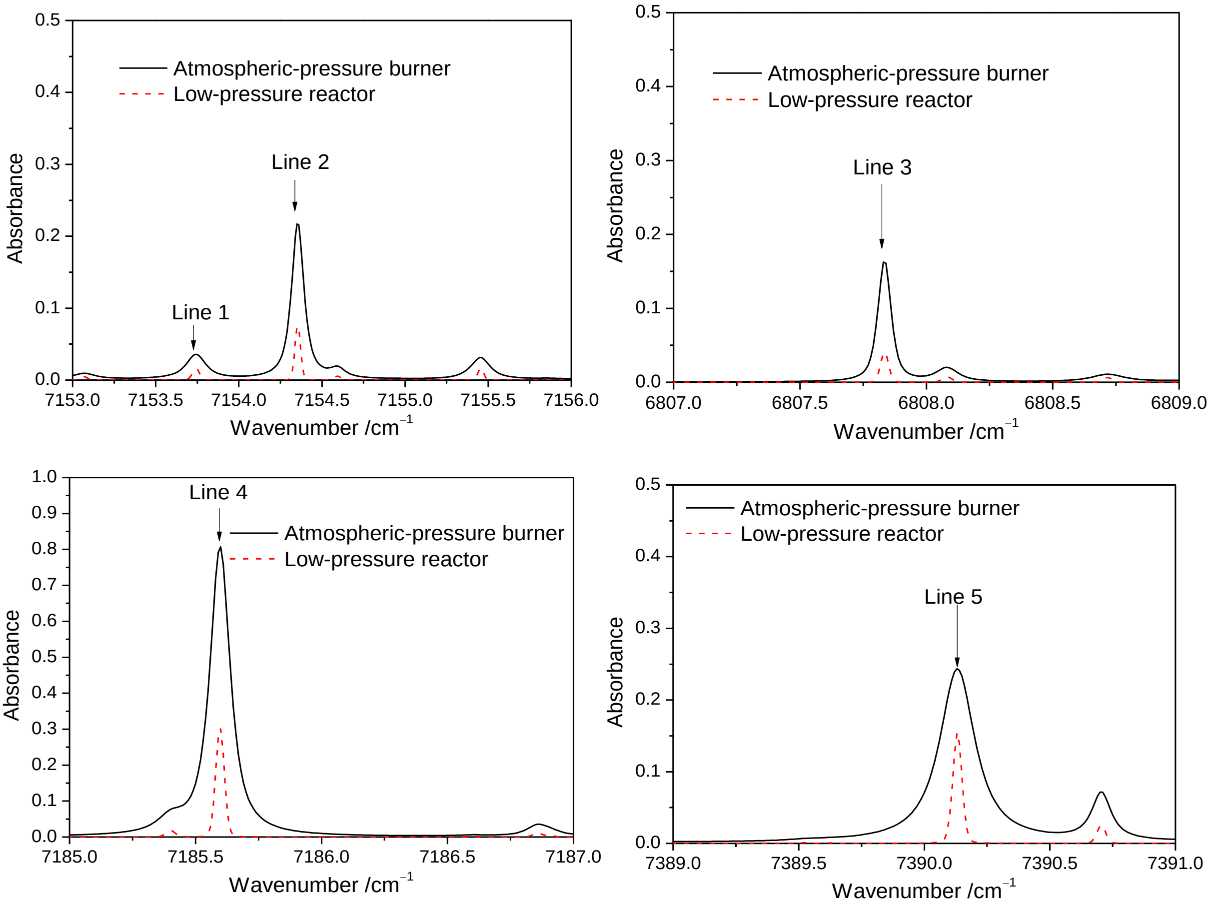

Fig. 32: Simulation of H_2O absorption lines for the five transitions for atmospheric-pressure burner and low-pressure reactor

Multi-line NO-LIF imaging

The diagnostic method of multi-line nitric-oxide (NO) laser-induced fluorescence (LIF) thermometry [8, 82-83] was applied to validate the TDLAS experiments. LIF is a process of spontaneous emission from an excited electronic state populated upon absorption of a laser photon. Quantitative state population distributions or total population prior to laser excitation, measuring temperature or species concentrations can be determined by this method. Multi-line LIF thermometry can consecutively probe several ground states with different term energies to determine the temperature with high temperature sensitivity in a wide temperature range. With this multi-line scanning method, lineshape effects caused by only partial overlap of excitation and absorption lines as well as background contributions are taken into account during numerical simulations of excitation spectra. Since NO is stable at a wide temperature range (250–2500 K) and provides strong red-shifted fluorescence signals, NO-LIF thermometry is attractive [78, 82]. The fundamentals of NO-LIF thermometry have been described previously [8, 82-83]. A pulsed, tunable, narrowband laser system was used, together with a spectrally filtered, gated and intensified CCD camera [78]. The laser is tuned over a part of the absorption spectrum of the NO molecule and individual fluorescence images are taken by the intensified CCD camera for each excitation wavelength. NO-LIF excitation spectra can then be obtained for each single pixel for the stack of images. The temperature is determined for each spatial location in the image plane via a non-linear least-square fitting (Levenberg-Marquardt algorithm) of simulated to experimentally determined NO-LIF excitation spectra. In the fitting procedure, the line shape and the exact position of the excitation lines are first determined and a pixel-by-pixel fit is then performed to obtain the temperature [78]. The technique has been used in previous work to determine the two-dimensional temperature profile (in planes containing the center line of the flame, i.e. parallel to the main gas flow direction) inside the same reactor [83].

By placing the excitation laser sheet parallel to the burner head, with different locations of the burner head relative to the light sheet, three dimensional temperature distributions can be obtained in the flame. The technique is provided to select temperature bins in the horizontal planes of the flame probed by TDLAS and will also help validating the results from TDLAS measurements. These NO-LIF measurements inside the reactor were performed by C. Hecht are described in detail in his PhD thesis [84], the results reported here are for purposes of comparison and validation with the TDLAS measurements.

4.2 Experimental setup

4.2.1 Atmospheric-pressure burner

The 1.4 µm multiplexed fiber-based diode-laser sensor was first applied on an atmospheric-pressure burner in order to verify the measurement accuracy of the temperature binning technique. The experimental setup is depicted in Fig. 33. The atmospheric-pressure burner (45 mm diameter) with a water-cooler porous bronze sinter matrix was used here stabilizing a premixed stoichiometric methane/air flame. A plate was positioned 20 mm above the burner to stabilize the flame and the temperature was measured at 15 mm height above the burner. Since this burner has a two-zone temperature distribution: a uniform high temperature in the flame zone that can be measured by a thermocouple and an ambient air temperature (~300 K) at both sides (Fig. 33). The TDLAS calculated temperature distribution can be then compared with the estimated value.

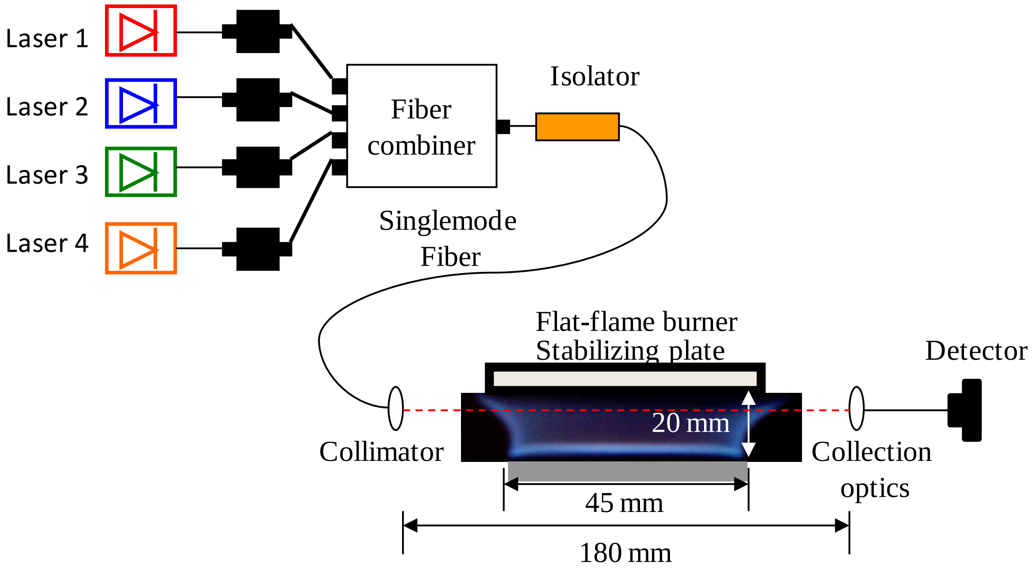

Fig. 33: Experimental setup for the temperature binning technique of TDLAS on an atmospheric-pressure burner

Four fiber-pigtailed diode lasers (NEL) (laser 1–4) are combined, collimated and transmitted through the atmospheric pressure. Since laser 1 (1398 nm) and 3 (1392 nm) has only 6 nm difference in wavelength, in the wavelength demultiplexing technique they cannot be separated by a grating. Since the flame is steady, the time division multiplexing (TDM) technique can here be used. In the case the multiplexed beam passing through the sample is registered by only one detector, which simultaneously simplifies the experimental setup. Each laser is scanned by a saw-tooth current ramp of 100 Hz across its targeted absorption transition. The individual absorbances are calculated by Voigt fits using LabVIEW (National instruments) program which also controlled the experiment.

4.2.2 Low-pressure flame reactor

The low-pressure nanoparticle flame-synthesis reactor is described in detail in [83]. A schematic drawing with front view (a) and top view (b) through the reactor are shown in Fig. 34. The top view in Fig. 34(b) is the cross section towards the ICCD camera in Fig. 34(a). The reaction chamber is 300 mm long with a diameter of 100 mm. A H_2/O_2/Ar flat flame (with flows of 600, 800, and 300 sccm, respectively) is stabilized at a total pressure of 30 mbar on a water-cooled sinter matrix burner, which is horizontally mounted inside the vacuum chamber.

For NO-LIF a fraction of Ar flow is substituted by a 2% NO/Ar mixture to obtain an overall concentration of 600 ppm NO.

H_2O TDLAS

The experimental setup of TDLAS shown in Fig. 34 (a) is similar to the application in the atmospheric-pressure burner introduced in section 4.2.1. Two wedged (2°) quartz windows with a free aperture of 90 mm at two sides of the chamber enable the diode laser beams to pass through the flame perpendicular to the translation axis of the burner head. The distance between the inner faces of two quartz windows at both sides is 150 mm. All the dimensions are marked in Fig. 34(b). The position of the beams was varied in a plane parallel to the burner head. Based on the temperature binning method and the assumption of a symmetric temperature distribution with the highest temperature on the burner axis, multiple parallel measurements provide information about the two-dimensional temperature distribution.

Multi-line NO LIF imaging

For the multi-line NO-LIF thermometry, a Raman-shifted narrowband KrF-excimer laser was tuned over individual NO absorption lines of the A-X (0,0) γ-band system around 225 nm, and an ICCD camera (LaVision) was placed perpendicular to the light sheet taking individual images for each excitation wavelength. The laser energy was kept low enough to avoid saturation of the NO transitions. LIF excitation spectra were then extracted for each pixel from the obtained images. The experimental data were then fitted with simulated spectra using LIFSim [85]. By this procedure temperature images were determined in the plane containing the centerline of the reaction chamber.

In the NO-LIF imaging, the windows at both sides previously used for the TDLAS measurements were used to pass the excitation laser light sheet through the combustion chamber in a plane parallel to the burner head. A third observation window opposite to the burner head allows detection of the LIF signal (see Fig. 34(a)). Since the limitation of space in the lab, the laser light is first reflected by a rectangle mirror in front of the window, and then an ICCD camera (LaVision) was placed far away to obtain the fluorescence images. Hence, the dimension of the 2D image obtained by NO-LIF is not round but a rectangle with length 90 mm and width 50 mm.

Through the movement of the burner head perpendicular to the laser light sheet in the same plane of the beams of the TDLAS technique to obtain a stack of two-dimensional data sets. These can be assembled into three-dimensional temperature distributions of the flame. It should be noted that the flame structure slightly changes whenever the burner head is moved to a different measurement position due to a variation in the heat losses of the flame gases to the combustion chamber walls.

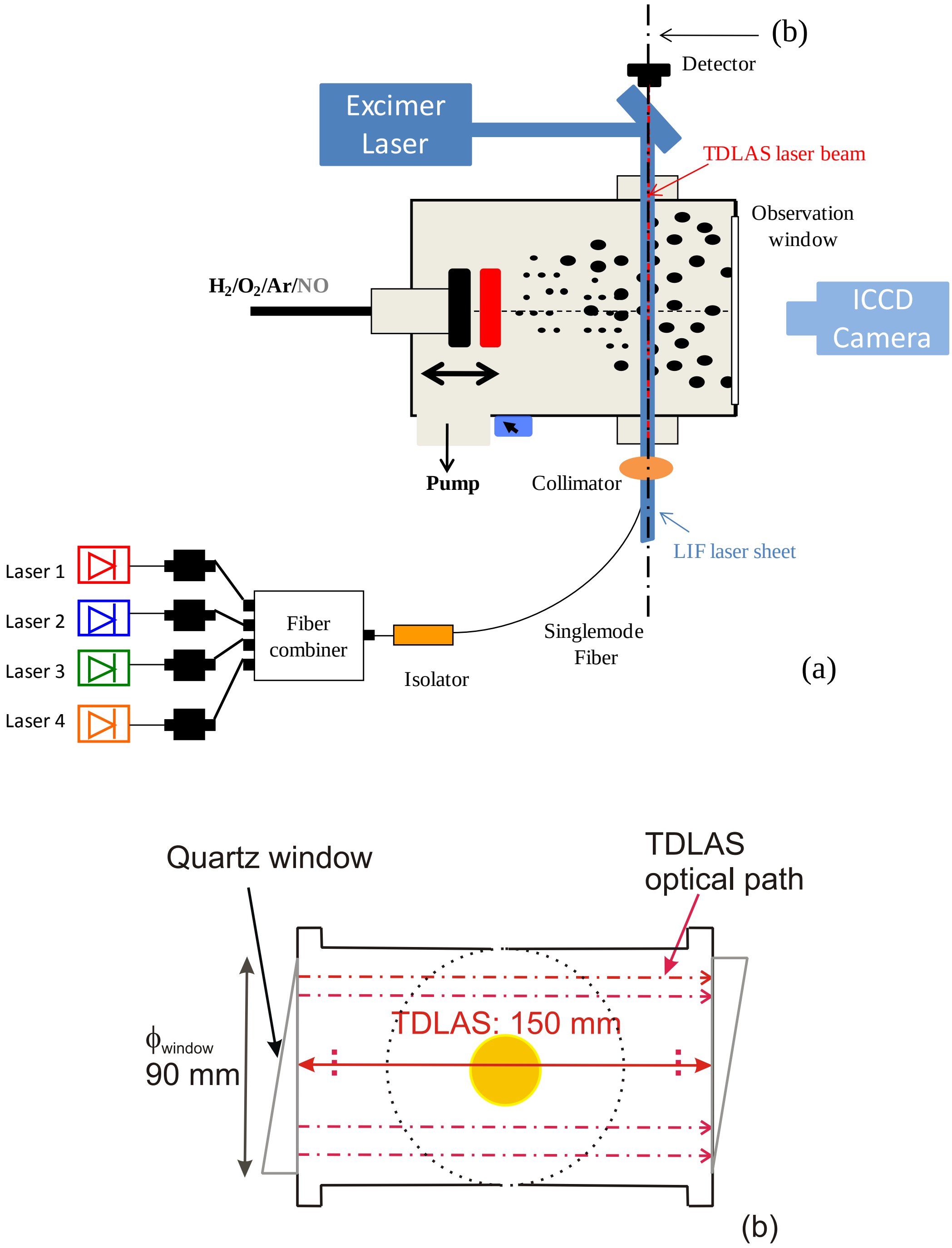

Fig. 34: Top view (a) with TDLAS and NO-LIF setup and front view (b) into the low-pressure flat-flame reactor

4.3 Results and discussion

4.3.1 Validation in the atmospheric-pressure burner

As shown in Fig. 33, the distance between the collimator and the detector collimating lens is 18 cm. The atmospheric-pressure burner is located in the center of the beam path. The flame is fueled by a mixture of methane and air. The fuel and air flow rates are controlled to be 8.635 l/min and 0.907 l/min respectively by a mass flow controller (Tylan) in order to realize an equivalence ratio of 1.0, which leads to an equilibrium water vapor mole fraction of 19%. The room air relative humidity indicated by a hygrometer was around 56%, which translates to a water mole fraction of approx. 1.75%. Based on previous research [56], the entire LOS path can approximately be divided into two temperature zones, one is the section in room air (~300 K) between the collimators and the flame boundaries, while the other is the hot flame measured by a thermocouple (982 K). The temperature, water mole fraction and the path length of the two zones are listed in

Table 3.

Table 3 Expected properties of the temperature distribution along the LOS measurement path

	Zone 1	Zone 2
T /K	300	982
x_{H2O}	0.0175	0.19
L /cm	2 × 6.75	4.5

As introduced in section 2.4.2, the recorded raw-data scan from the detector for the individual transition can be used to determine the integrated absorbances A_i by fitting a Voigt function to the respective absorption line. Assuming constant pressure the extracted absorbance values are then used to solve eq. 57 in order to obtain the x_iL_i by a non-negative least squares fitting procedure written in MATLAB.

Four temperature bins 300 / 600 / 750 / 1000 K are estimated. The calculated x_iL_i (indicated as red solid bars) along the beam path is close to the expected results (dashed lines in Fig. 35). There are two zero solutions (i.e., evaluated zero length sections) for the 600 and 750 K bins, and non-zero solutions at both side bins, which shows a consistent trend with the estimated two-temperature zone.

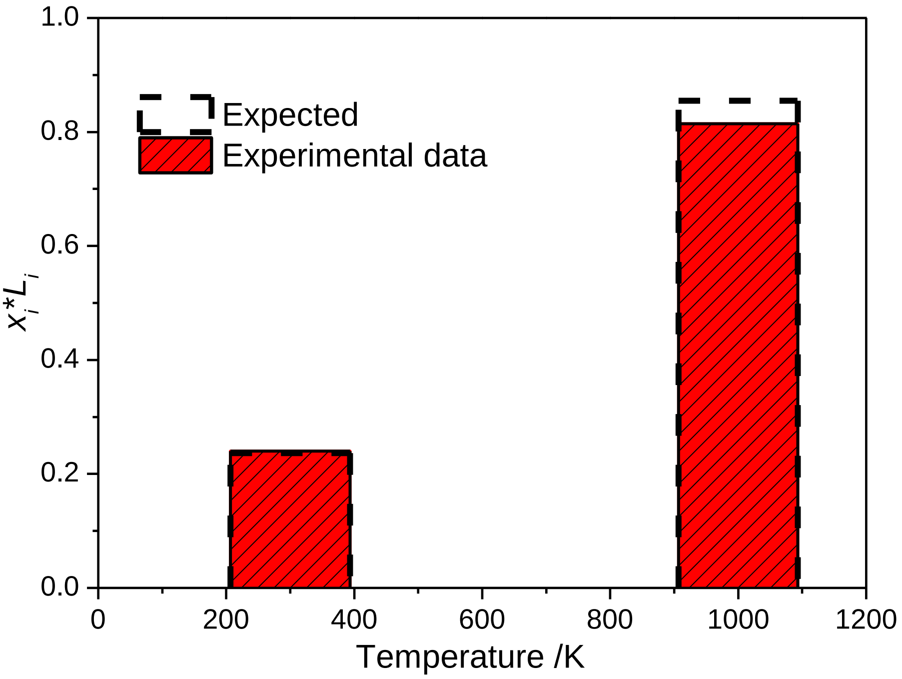

Fig. 35: Illustration of the temperature binning results using five individual transitions in the atmospheric-pressure burner

4.3.2 Low-pressure flame reactor

At low pressure, the linewidth is dominated by Doppler broadening. The reduced collisional broadening causes narrower transition linewidths in low-pressure than in atmospheric-pressure environments. Meanwhile, according to eq. 34, the absorbance is also smaller at low pressure than at atmospheric pressure when species concentration, temperature and pathlength are identical. However, at low pressure the transitions are more isolated from neighboring lines, as e.g., for line 2 depicted in Fig. 32.

As suggested in [44], the choice of the temperature bins is critical in the temperature binning technique. In the present work the temperature profile was first evaluated from the multi NO-LIF thermometry measurement and, from this information suitable temperature bins were estimated for evaluating the TDLAS line-of-sight temperature profile. The NO-LIF has an optical access of 90 mm because of the observation window aperture, while the free beam path of TDLAS is 150 mm (as shown in Fig. 34b). Hence, the temperature information obtained by NO-LIF should be expanded to a larger region.

In the NO-LIF experiments the gas temperature field was measured by moving the burner head relative to reference positions for different HAB, thus obtaining a stack of temperature fields in planes parallel to the burner head for different burner positions. The 2D temperature image at 5 cm HAB is shown in Fig. 36a, the obtained temperature (black square) along the laser sheet propagation direction of a binned 2 mm wide stripe (white rectangle in Fig. 36a) at 10 mm above the burner centerline is depicted in Fig. 36b. The red line is a second-order polynomial fit to the data. The maximum temperature is close to 980 K and the fitted curve reveals that the temperature is ~400 K when extends the length of TDLAS beam path of 150 mm. From these results temperature bins with values of 400, 550, 800 and 1000 K were selected for evaluating the corresponding TDLAS measurements along the LOS.

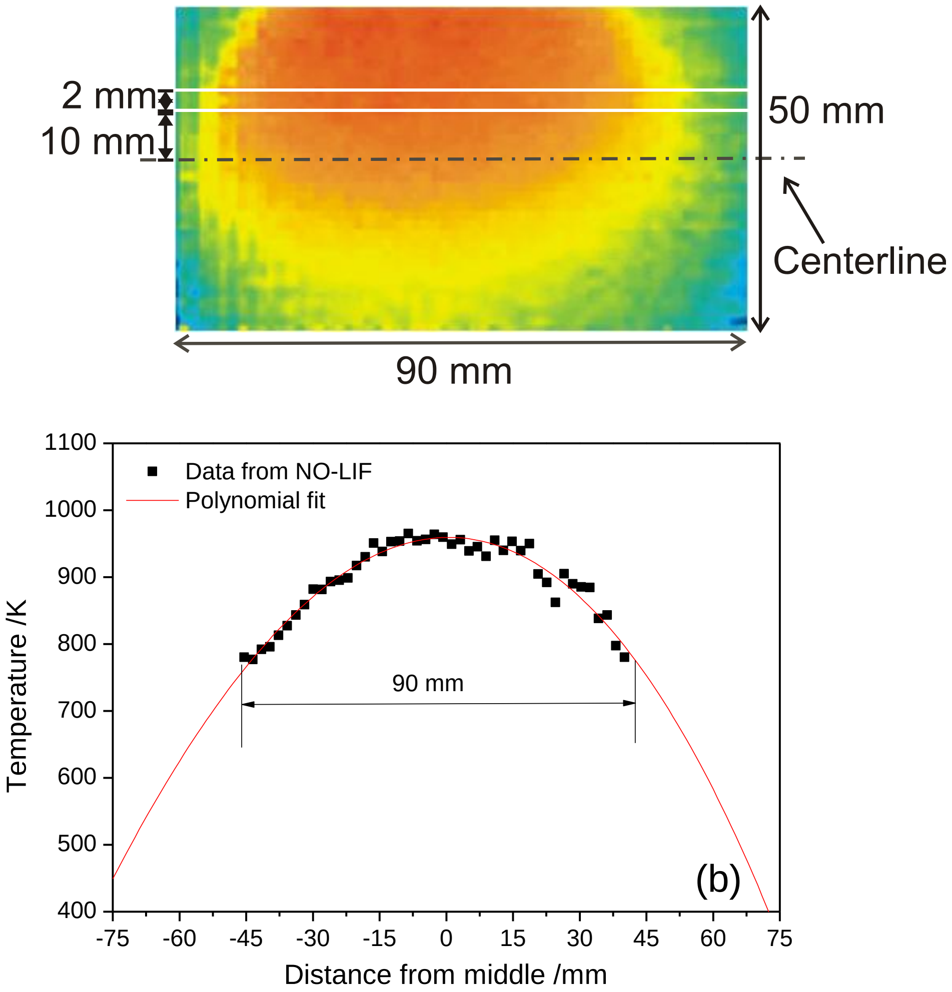

Fig. 36: NO-LIF 2D image (a) at HAB 5 cm and temperature profile (b) along the beam path of TDLAS 10 mm above the centerline evaluated from the image

For the TDLAS measurements the experiments were performed in the reactor by first fixing the burner head at three different HAB (3, 5, and 7 cm, respectively). For each fixed HAB position, the laser beam then was displaced parallel to the burner plate in steps of 2 mm, thus measuring 36 positions in each plane. The water vapor concentration is assumed homogenously distributed along the whole beam path inside the reactor. This is justified because the flame gases fill the whole chamber due to the absence of an inert gas co-flow.

By these assumptions the length fractions f_j for each temperature bin were calculated by eq. 58-61 as shown in Fig. 37. A value of zero on the *y*-axis indicates the beam crossing the symmetry axis of the burner, and positive and negative values corresponding to the laser beam passing above or below this line. The length fraction distribution shows that the flame shape is asymmetric with respect to the central axis: The maximum of the length fraction of the highest temperature bin (1000 K) is not located at the zero position. Since the flame is mounted horizontally, the flame is distorted by buoyancy effects. The evaluated length fractions show that the temperature in the upper part of the plane above the burner is higher than in the lower part, the location of the highest flame temperature is slightly shifted to the higher part and distribution of the highest temperature distribution is getting narrower with increasing HAB. It is shown that the high-temperature length fraction is largest (i.e., ~35%) at 3 cm HAB. The majority of the data points fall within the intermediate temperature bins (550 and 800 K, black circles in Fig. 37), which occupy regions further outside the centerline of the burner, whereas the higher temperature regions are located in the center region of the respective planes. As expected, significant length fractions of the low temperature bin (400 K) are located near the edge of the probed regions. The asymmetric length fraction distribution is visible for each of the selected temperature bins and all three HAB positions.

To validate the measured spatially resolved water vapor temperature distributions from TDLAS, the temperature values deduced from the NO-LIF measurements, averaged over a 2 cm stripe along the direction of NIR beam path (as shown in Fig. 36a) were obtained. An example for the 5 cm HAB experiment is plotted in Fig. 38. In qualitative agreement with the TDLAS measurements the temperature profile is also shifted with respect to the burner centerline. Because the flame is asymmetric inside the reactor, TDLAS 2D temperature reconstruction is impossible. In order to get a symmetric flame, the reactor should be turned to an upright configuration for further experiments.

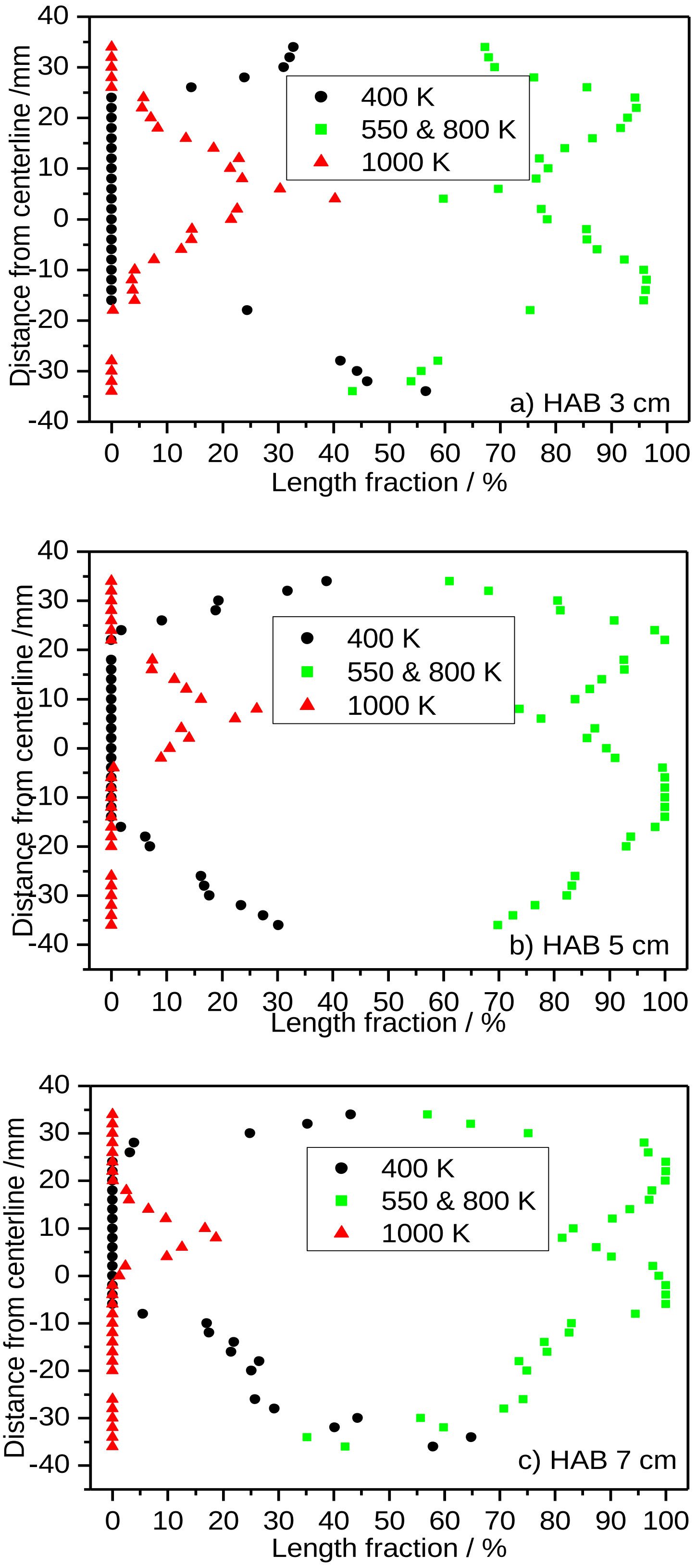

Fig. 37: Length fractions of the temperature bins in planes parallel to the burner head at fixed HAB of 3 (a) 5 (b), and 7 cm (c), respectively

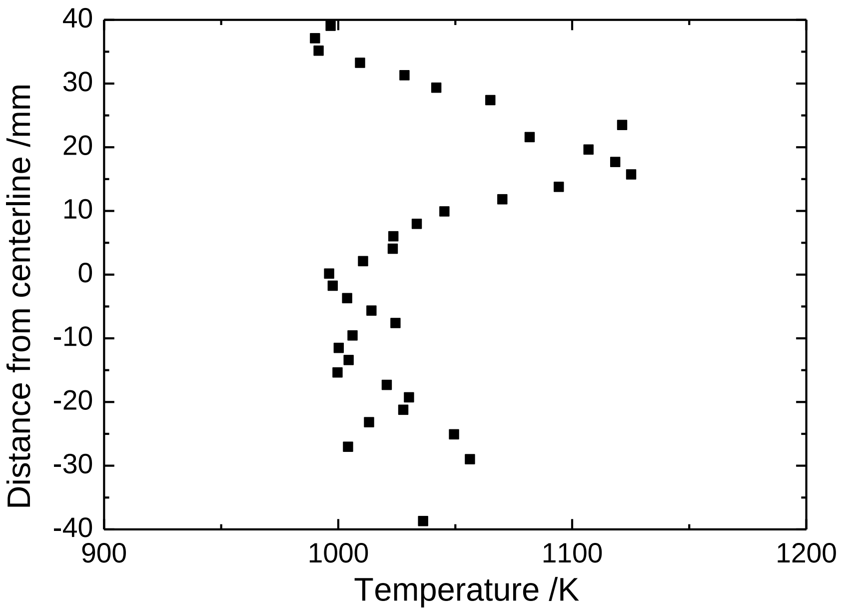

Fig. 38: Temperature profile perpendicular to the TDLAS beam path in the center measured with NO-LIF thermometry at 5 cm HAB

4.3.3 Low-pressure flame reactor after 90 °rotation

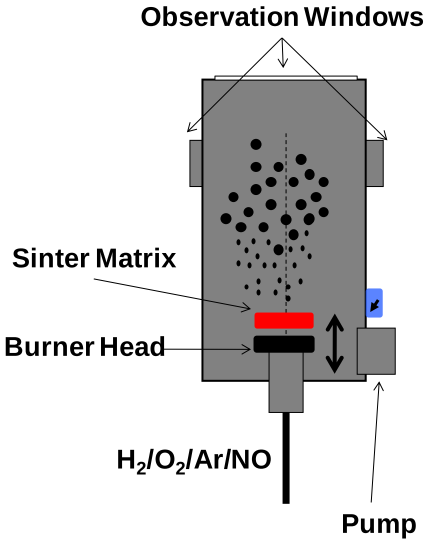

Fig. 39: Low-pressure flame-reactor after 90 °rotation

Since buoyancy effects disturb the flame structure in the horizontally mounted burner, the reactor was rotated 90 ° counterclockwise to obtain a symmetric flame (Fig. 39). The experimental setup is similar as described in section 4.3.2, with the ICCD camera for NO-LIF now placed vertically above the burner chamber. With this setup the 2D_reconstruction TDLAS and the LIF experiments were repeated. In their work, Liu et al. [86] pointed out that increasing the number of estimated temperature bins will deteriorate the measurement accuracy from their simulation studies. Therefore, here only three temperature bins were chosen instead of four to decrease the measurement uncertainties. Based on the available NO-LIF temperature profiles temperature bins of 300, 670 and 1400 K were chosen for evaluating the corresponding TDLAS measurements.

From the results the length fraction distributions of each temperature bin at HAB 7 cm is taken as an example and plotted in Fig. 40. It reveals that the highest temperature bin (1400 K) is located in the middle of the flame zone, the majority of the length fraction ~60 % is the intermediate temperature bin (670 K), and the lowest temperature bin (300 K) has the larger fractions at both border regions of the flame than near the centerline. The spatial temperature distribution observed by NO LIF shows that the temperature distribution is symmetric relative to the burner axis in direction of the (horizontal) laser beams which justifies the approach for the 2D reconstruction method based on the multiple parallel TDLAS measurements with temperature binning. The resulting 2D temperature distribution based on the result from Fig. 40 is plotted in Fig. 41 as a contour plot where the lines indicate the limits of the individual temperature bins. The width of the two-dimensional temperature image along the burner head is only 62 mm corresponding to the 31 beam positions measured in the TDLAS experiments.

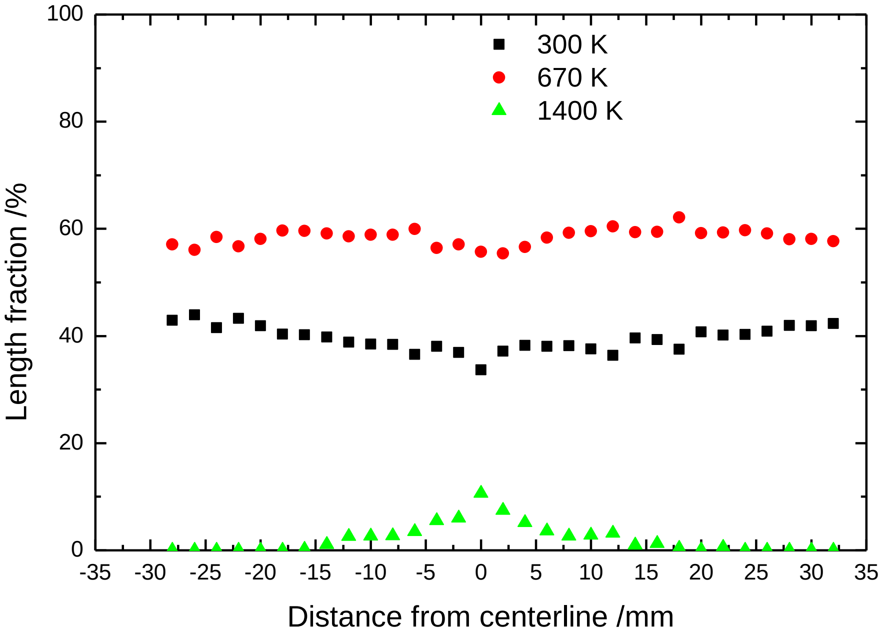

Fig. 40: Length fractions of the temperature bins in a plane parallel to the burner head at 7 cm above the burner

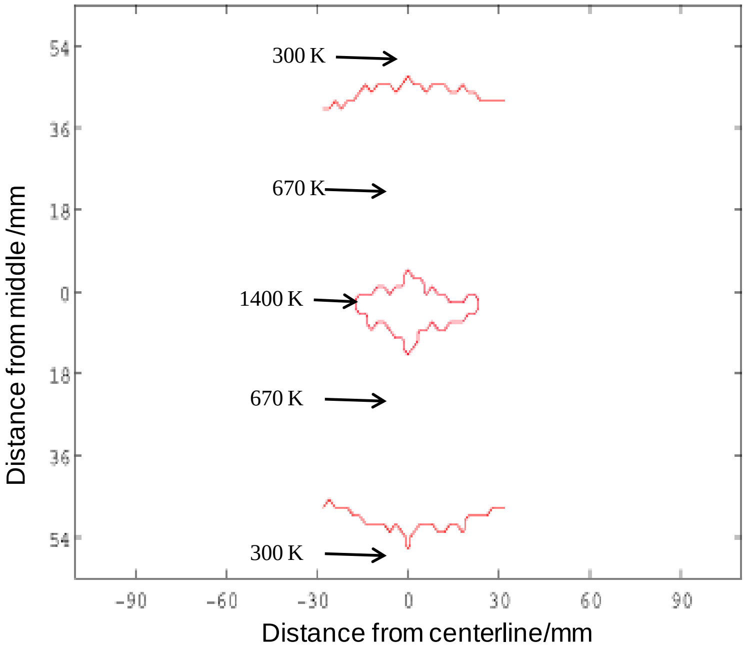

Fig. 41: 2D temperature reconstruction of TDLAS temperature at HAB 7 cm

To compare the NO-LIF 2D temperature distribution with TDLAS, two limiting temperatures should be defined for NO-LIF by assuming the temperature bins are associated with their respective center temperature. However, these two temperatures in between the three temperature bins was not exactly the arithmetic average, they can be determined by a "numerical experiment" as shown in Fig. 42. The relationship between the temperature and the length of the estimated temperature bins can be assumed to be linearity. The temperature is assumed to be started from 300 K up to 1400 K, increased by every 1 K with a pathlength of 1 mm. The absorbance can be determined by eq. 34 at each temperature for the five transitions with TDLAS. The lengths of the three estimated temperature bins can be obtained by eq. 58-60 based on the calculated absorbances. The value of the *y*-axis in Fig. 42 corresponds to the two interfaces between these three calculated lengths are determined as the limiting temperatures to be 408 K and 1024 K (two steps in Fig. 42). That is, the temperatures determined from NO-LIF higher than 1024 K would be accounted for 1400 K temperature bin, below 408 K accounted for 300 K temperature bin and other temperatures belong to the intermediate temperate bin. The calculated two-dimensional temperature profile obtained from NO-LIF thermometry is plotted in Fig. 43. The comparison of the 1400 K bin with TDLAS is shown in Fig. 43. Other two bins cannot be compared here due to the limited observed range of NO LIF. Both of them show a symmetric distribution and overlap each other. However, the contour of the TDLAS is smaller than the results of NO-LIF thermometry, because the colder region near the windows at both sides cannot be observed by NO-LIF thermometry.

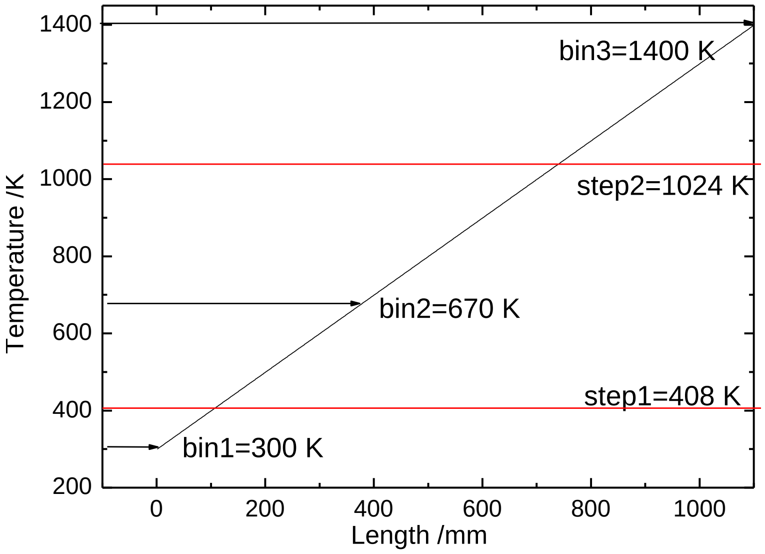

Fig. 42: Numerical experiment to determine the interface temperatures between three temperature bins of NO-LIF in order to compare with TDLAS 2D temperature distribution

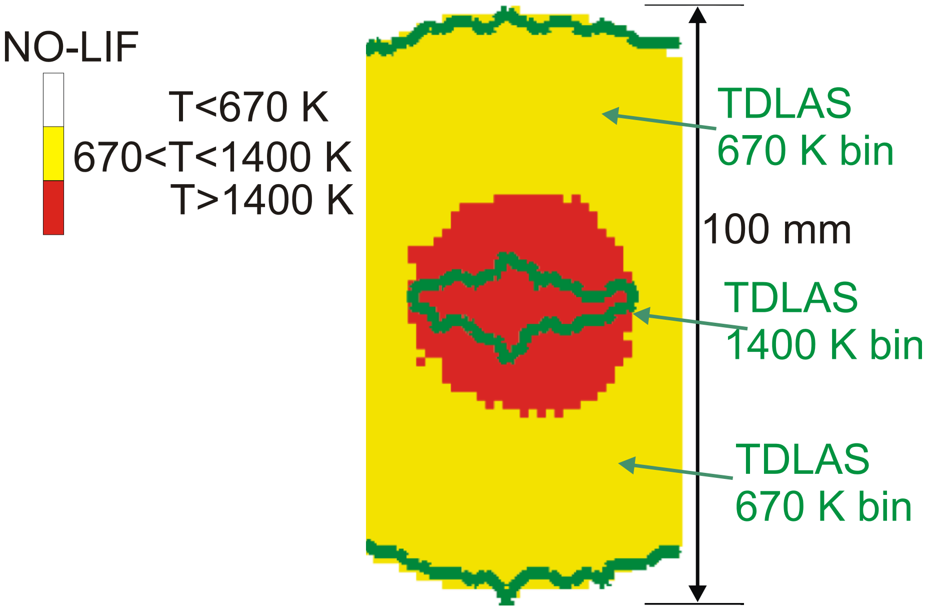

Fig. 43: Reconstruction of TDLAS temperature-binning results in comparison with 2D measurements based on multiline NO-LIF thermometry

4.4 TDLAS temperature measurements: Summary

In this chapter, the TDLAS multi-line thermometry for flames exhibiting a non-uniform temperature distribution along the absorption beam path was investigated. The temperature binning technique was applied using four diode lasers (lasers 1–4) with five water absorption transitions of different temperature dependency (i.e., different lower-state energies *E*”). In such cases the non-uniform temperature distribution along the line of sight can be obtained by non-negative least squares fitting.

The technique was first investigated in an atmospheric-pressure burner with a “two-zone” temperature distribution to provide an estimate for the measurement accuracy. The calculated product of assumed concentration and length fraction within which concentration is assumed to be constant, $x_i L_i$, was compared with expected values and showed reasonable consistency. The technique was then applied in a low-pressure flat-flame burner, where a comparison with results from multi-line NO-LIF thermometry was available, and which provided some initial estimate for the choice of proper temperature bins (400, 550, 800, and 1000 K, respectively). Experiments were performed at different HAB (3, 5, and 7 cm, respectively), with the NIR laser beams routed through the reactor in planes parallel with the burner head at each fixed HAB position. The length fractions of each temperature bin at each HAB were evaluated from the absorption signals. The highest temperature was observed at 3 cm HAB. However, since the burner was mounted horizontally, the 1000 K temperature bin was located off center of the burner symmetry line, which was an indication that the flame was asymmetric due to buoyancy effects. After rotating the reactor by 90°, the TDLAS showed (e.g. at HAB 7 cm) a symmetric temperature distribution. It shows a similar spatial temperature distribution compared to the NO-LIF method.

5 TDLAS applied for liquid-water film-thickness measurements

In this thesis a fiber-based multiplexed tunable diode-laser absorption sensor with four near-infrared (NIR) distributed-feedback (DFB) diode lasers at ~1.4 µm was used for the first time for simultaneous non-intrusive measurement of liquid water film thickness, liquid-phase temperature, and vapor-phase temperature above the film, respectively. As detailed in section 2.5.1, the vapor-phase temperature is obtained from the absorbance ratio of two lasers rapidly tuned across narrow gas-phase absorption transitions, whereas the other parameters are calculated from the absorbance ratio at three wavelengths assessing the broad-band spectral signature of liquid water. With regard to the water film temperature measurements an optimized combination of laser wavelengths were determined using liquid-water absorption cross sections measured by a Fourier transform infrared (FTIR) spectrometer. When probing the liquid film at three different wavelengths with significantly different absorption cross-sections, two of these have extreme different temperature sensitivities, which favors them for liquid temperature measurements. It allows discriminating against additional signal losses due to surface fowling, reflection and beam steering simultaneously. The performance of the sensor was first validated in calibration-tool experiments with liquid layers of known thickness and temperature. Then experiments are presented for time-resolved thickness and temperature measurements of evaporating water films on a transparent quartz plate. The sensor was also applied in a flow channel for film thickness measurements. The TDLAS technique is also compared with two imaging diagnostic methods performed within the PhD thesis work of D. Greszik – laser-induced fluorescence (LIF) from low concentrations of a dissolved tracer substance, and spontaneous Raman scattering of liquid water, respectively, both excited with a laser beam at 266 nm [87]. Results from each method are compared for the thickness measurement of liquid water films deposited on a transparent quartz plate.

5.1 Liquid water

In the liquid phase, water exhibits broad-band absorption from the OH-stretch vibrational bands in the NIR region due to hydrogen bridge bonding and hindered rotations. The vibrational manifolds are broadened significantly due to the high density and the large number of collisions. Compared to the gas phase the main stretching band in liquid water is shifted to a lower frequency (v_3, 3490 cm^{-1} and v_1, 3280 cm^{-1}) [88] and the bending frequency increased (v_2, 1644 cm^{-1}) [89]. The frequency of the fundamental vibration modes for liquid water and water vapor are shown in Table 4. A review of the absorption spectrum of liquid water covering the wavelength region between 0.2 and 200 µm is given by Hale et al. [90] and a more detailed compilation in the 0.65–2.5 µm range was presented by Kou et al. [91]. A portion of the broad-band liquid water absorption spectrum published by Kou et al is shown in Fig. 44 [91]. The imaginary part of the refractive index of water at room temperature was reported, however, the measurements were performed in a Bomem DA3.02 FTIR spectrometer with low spectral resolution of 16 cm^{-1} [91]. In the present work higher resolution spectra at different temperatures were measured in our FTIR spectrometer, which will be described in the section 5.2.2.

Table 4: Fundamental vibrations and frequencies for water vapor and liquid water [34]

Vibrational mode	Frequency in water vapor [cm^{-1}]	Frequency in liquid water [cm^{-1}]
v_1	3652	3280
v_2	1595	1644
v_3	3756	3490

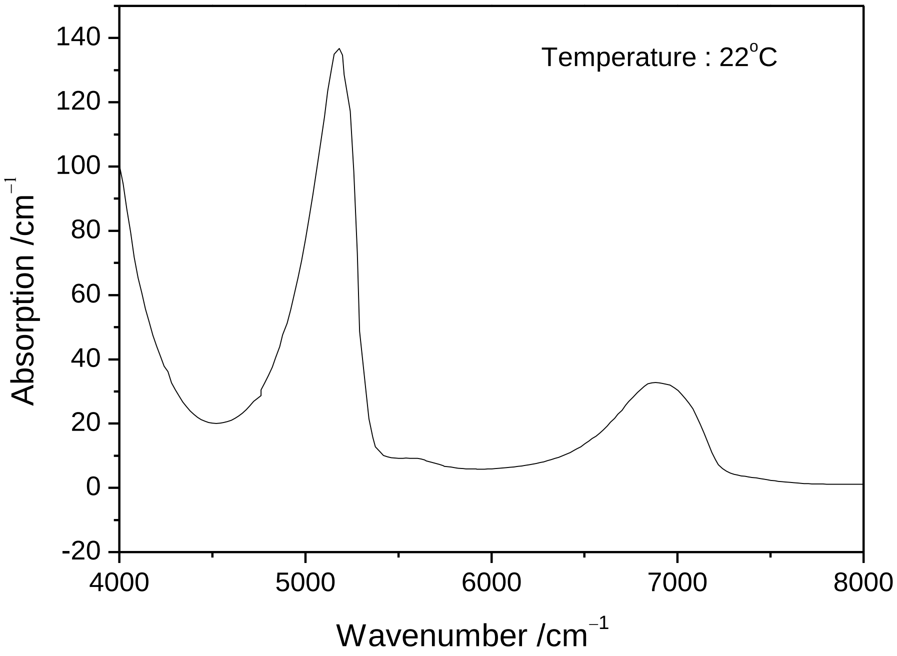

Fig. 44: Absorption spectrum of liquid water from 4000 to 8000 cm^{-1} [91]

5.2 Measurement strategy

TDLAS relies on a rapid scanning of the laser wavelength via current tuning to distinguish between narrow band molecular absorption features in the gas phase and laser attenuation due to other losses such as reflection at interfaces, window fouling, scattering, and beam steering.

When applying to water-vapor measurements, the molecular absorption of gas-phase species is then derived from the spectrally integrated narrowband absorption features after subtracting the spectrally unstructured background effects. When a liquid water film is present in the beam path, additional absorption originating from the unstructured broad overtone and/or combination vibrational bands in the liquid occurs. Using a suitable combination of different wavelengths its contribution also is subtracted in the data evaluation when determining the line-integrated absorption from the gas-phase species. At the same time the data evaluation can also return information about the broad-band liquid water absorption and thus film thickness. Because in the NIR region (5500–8000 cm^{-1}) the broad-band absorption of liquid water is strongly wavelength dependent, a measurement at more than one wavenumber position allows separating the absorption due to liquid water from the other light losses that can be considered wavelength independent absorption. In addition, the liquid water absorption spectrum changes with temperature (cf. [92]) in this region, this must be taken into account when determining the film thickness. With a suitable choice of several different wavenumber positions based on our survey FTIR measurements of liquid water absorption cross sections (see below), the liquid film thickness and its temperature in the presence of unspecific laser attenuation can be simultaneously deduced.

5.2.1 Vapor-phase temperature

As already introduced in chapter 4, TDLAS is commonly used for the measurement of vapor-phase temperature, T_v, and species concentration [18, 60, 93-94]. For temperature measurements in environments with unknown absorber concentrations a minimum of two transitions with a separation in ground state energy adjusted to the expected temperature range must be used [12] taking into account their spectral properties, such as overlap with neighboring transitions, line strength, lower state energy, thermal population, and line broadening and shifting [54]. The contribution of broad-band absorbers or the attenuation due to losses on the optics is excluded by scanning the lasers rapidly across the line profiles and by evaluating the contribution of the narrow-band absorption only. When measuring water vapor concentration and temperature above liquid films, the broad-band absorption features of the liquid film add to the losses and can be neglected from the evaluation of absorbance ratios.

In the experiments presented here, we follow the line selection for the measurement of T_v as discussed in chapter 3.3 assessing two transitions in the v_1+v_3 band with transition frequencies of 7185.59 and 7390.13 cm^{-1} (denoted as laser 3 and 4 in chapter 3.3, respectively). The vapor-phase temperature can be then obtained by comparing the absorbance ratio between laser 3 and 4 with two-line thermometry.

5.2.2 Liquid-phase temperature and film thickness

Since in the early research there are no accurate enough liquid-water absorption cross sections available in the NIR region of interest, in the present thesis a FTIR spectrometer with a spectral resolution of 2 cm^{-1} was used to measure the wavelength- and temperature- dependent absorption cross section $\sigma(v,T_l)$ of liquid water. For this purpose tri-distilled water was filled in a 1-mm-pathlength quartz cuvette with two optical windows and a double-jacket wall through which thermostating oil was circulated with temperatures between 298 and 348 K. The absorption spectrum at different temperatures is presented in Fig. 45. The error bars indicate a statistical error of 1% for three repeated experiments. With increasing temperature, the peak of the absorption feature slightly shifts towards larger wavenumbers (i.e., shorter wavelengths) [92, 95]. Hence, the temperature of the liquid can thus be retrieved from measured transmittance ratios at suitably chosen wavelength positions, ideally at both sides of the peak maximum, where the derivative of absorption cross-sections with respect to temperature, $d\sigma/dT$ has an opposite sign.

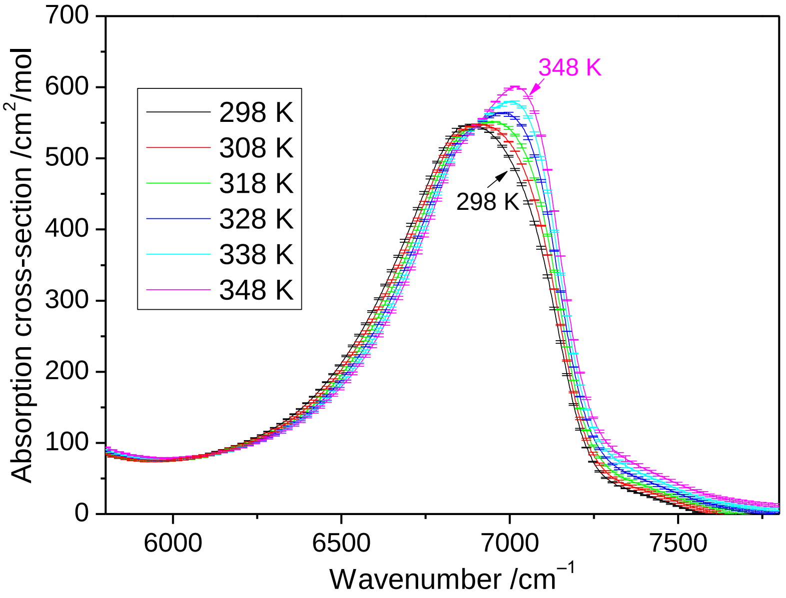

Fig. 45: Near-infrared absorption spectrum of liquid water in the range 5500–8000 cm^{-1} for temperatures between 298 and 348 K measured via FTIR

The $d\sigma/dT$ is depicted as a dashed line in Fig. 46. The wavenumbers of the diode lasers used in the present work are marked as vertical lines. Lasers 3 and 4 are the two used for the vapor phase temperature measurements (see section 5.2.1). Two additional diode lasers (laser 5 and laser 6) were positioned around the extrema (7082.89 cm^{-1} and 6714.57 cm^{-1}, respectively) of the $d\sigma/dT$ curve. Because laser 4 exhibits the lowest absorption cross-section in the liquid (red curve shown in Fig. 46), it can be combined with laser 5 and 6 to infer the additional non-specific background attenuation that is caused by losses from the window surfaces or other broad-band absorptions. The tuning range of laser 4 was sufficiently wide to cover the water vapor line at 7390.13 cm^{-1} as well as an (essentially flat) region of „background absorption" at 7389.47 cm^{-1} that is dominated by attenuation not related to water.

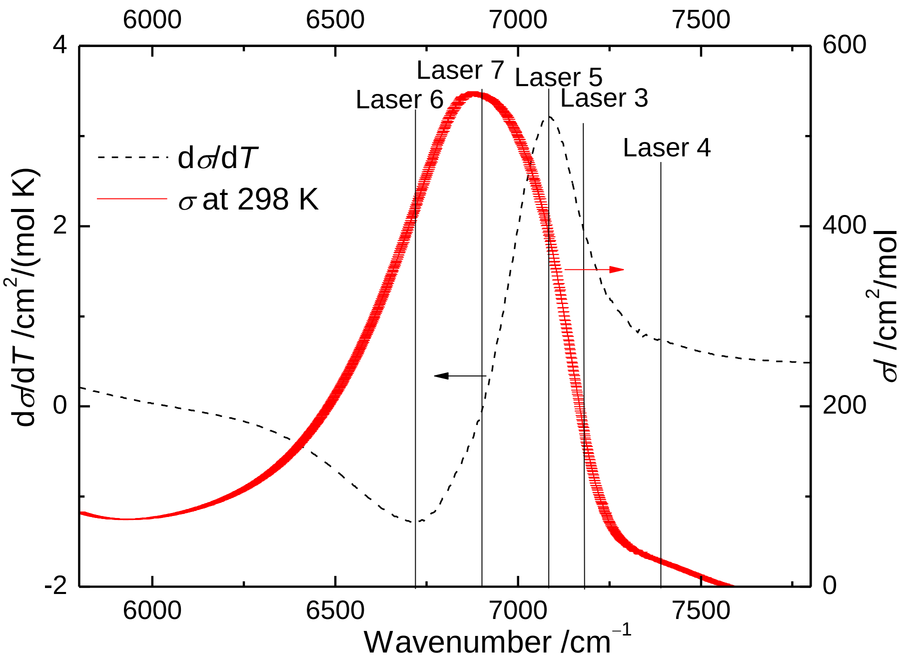

Fig. 46: The wavelength dependence of the derivative of the absorption cross-section with respect to temperature from 298 to 348 K (dashed line) and measured absorption cross-section at room temperature (red symbols)

Fig. 47 shows the temperature dependence of the absorption cross section as derived from Fig. 45 for the wavenumber positions of lasers 4-6 together with their linear fit (solid lines):

$$\sigma(v_i, T_l) = a_i + b_i T_i \qquad i = 4, 5, 6 \tag{63}$$

where a_i and b_i are the respective fitting coefficients, and T_l is the temperature of the liquid.

Based on the Beer-Lambert law introduced in eq. (29), the transmittance $\tau(v_i)$ at the wavenumber v_i of the laser beam passing through the liquid film is described as

$$\tau(v_i) = \left({}^{I_t}\!/_{I_0} \right) = (1 - u)\exp(-n)\sigma(v_i, T_l)d_l \tag{64}$$

where I_t and I_0 are the transmitted and incident intensities, respectively, d_l is the length of the absorbing medium (i.e., the film thickness), and $u < 1$ represents a non-specific background attenuation. In order to discriminate the liquid water absorption from other non-specific attenuations (represented by u), the ratio of the transmittance is calculated. n [mol/cm^3] is the molar concentration of the absorbing species,

$$n = \frac{\rho(T_l)}{M} \tag{65}$$

with the density ρ [g/cm^3] and the molecular mass M [g/mol]. The temperature dependence of the density of the liquid can be fitted with a second-order polynomial [96], which is shown in Fig. 48:

$$\rho(T_l) = 0.73694 + 0.00199T_l - 3.73881 \times 10^{-6}{T_l}^2 \tag{66}$$

After inserting eq. (63), (65) and (66) into (64), the transmittance τ is a function of the three unknown parameters T_l, d_l and u.

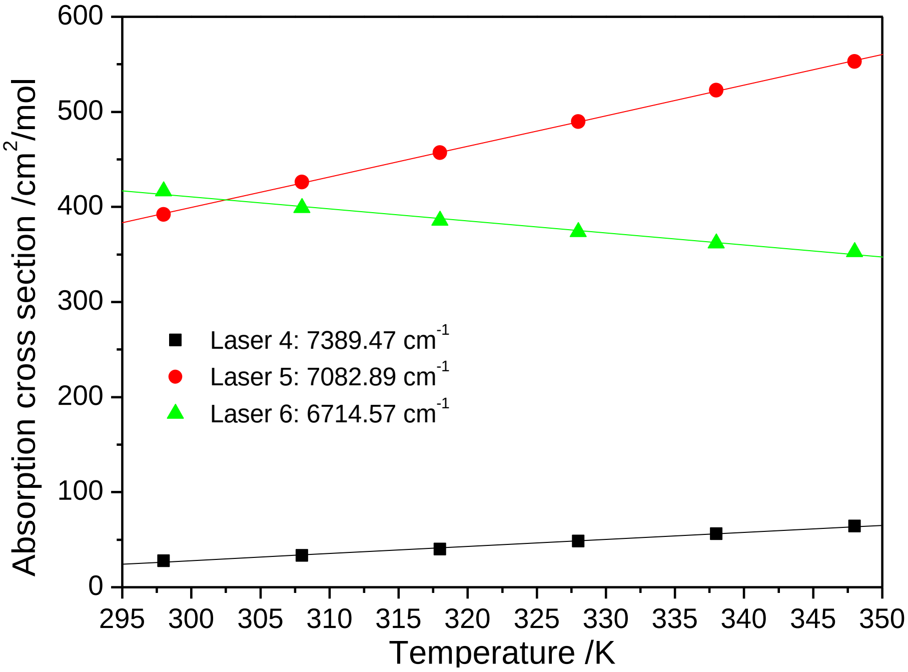

Fig. 47: Temperature dependence of the liquid water absorption cross-sections at the three wavenumbers of lasers 4–6 (cf., Fig. 45) relevant in the thickness measurement strategy

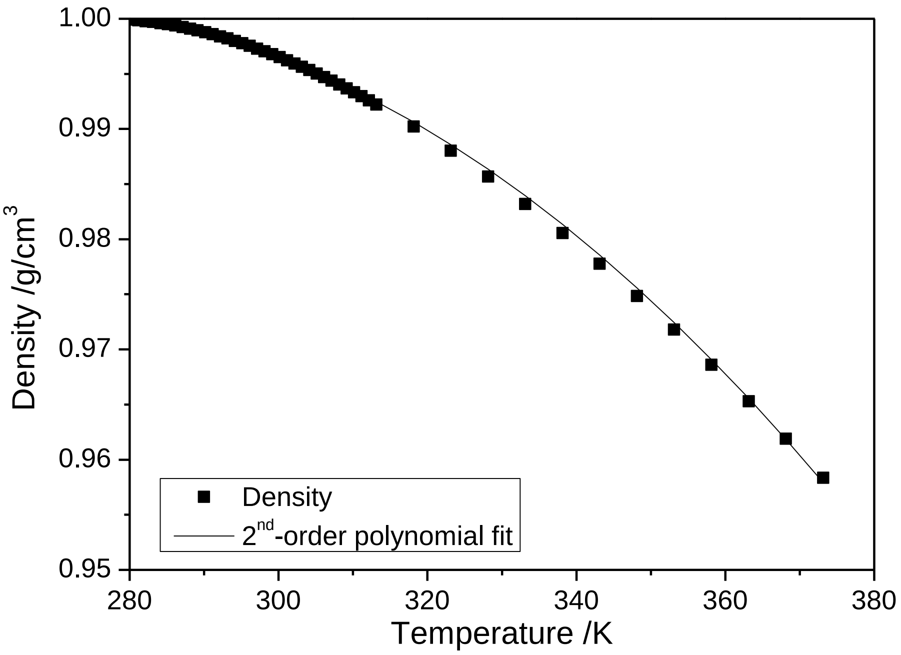

Fig. 48: Temperature dependence of the density of liquid water (symbols) with its 2nd-order polynomial fit (line)

Generally, for a liquid film deposited on a substrate transparent for the analysis light the partial reflection losses at each phase boundary must be taken into account when calculating the total transmitted intensity for each wavelength individually. This has been demonstrated before by Porter et al. in their studies of film thickness measurements of liquid hydrocarbon fuels [75], where the dispersive signature of the complex refractive index changes substantially in the neighborhood of the absorption band. However, in the case of liquid water the real part of the complex refractive index is almost constant in the NIR spectral region of interest, i.e., it varies by less than 0.8% from 5800 to 7800 cm^{-1}. This leads to a baseline offset [75] smaller than 1% when taking the difference of refractive indices into account between quartz and the liquid. Therefore, in our experiments this contribution can be considered as a constant to the non-specific background attenuation, u. Forming the ratio of the transmittance values of lasers 6 and 5 (eq. (67)), and lasers 6 and 4 (eq. (68)), respectively, u can be eliminated:

$$R_{6/5} = \left({}^{I_t}\!/_{I_0} \right)_{v6} \Big/ \left({}^{I_t}\!/_{I_0} \right)_{v5} = \exp\big(n\big(\sigma_5(T_l) - \sigma_6(T_l)\big)d_l\big) \tag{67}$$

$$R_{6/4} = \left({}^{I_t}\!/_{I_0} \right)_{v6} \Big/ \left({}^{I_t}\!/_{I_0} \right)_{v4} = \exp\big(n\big(\sigma_4(T_l) - \sigma_6(T_l)\big)d_l\big) \tag{68}$$

Following this procedure, the logarithmic ratio R of (68) and (69) cancels n and d_l, and R is a function of the temperature of the liquid only:

$$R(T_l) = \ln(R_{6/5})/\ln(R_{6/4}) = (\sigma_5(T_l) - \sigma_6(T_l))/(\sigma_4(T_l) - \sigma_6(T_l)) \tag{69}$$

The sensitivity of the measurement with respect to T_l depends on the absolute value of the derivative $\mathrm{d}R/\mathrm{d}T_l$.

$$dR/dT_l = \frac{(d\sigma_5/dT_l - d\sigma_6/dT_l) * (\sigma_4 - \sigma_6) - (d\sigma_4/dT_l - d\sigma_6/dT_l) * (\sigma_5 - \sigma_6)}{(\sigma_4 - \sigma_6)^2} \tag{70}$$

Because in the present experiments, a simultaneous measurement is attempted of T_v and other variables (i.e., T_l and d_l), it is attractive to use laser 4 (introduced in chapter 3.3) also for the T_l measurement in order to reduce the total number of required laser wavelengths from 5 to 4. Other two additional lasers were chosen at wavelengths with maximum and minimum $\mathrm{d}\sigma/\mathrm{d}T_l$ (laser 5 and 6, cf. Fig. 46), respectively. The temperature dependence of the absolute value of the ratio, $|\mathrm{d}R/\mathrm{d}T_l|$, of this combination of laser wavelengths is plotted in Fig. 49; it increases with increasing liquid-phase temperature. With five lasers (or with giving up the attempt to simultaneously measure T_v) the sensitivity of the T_l measurement could be further increased with one laser (denoted as laser 7 in Fig. 46) near the maximum of the absorption feature at 6903.91 cm^{-1} with $\mathrm{d}\sigma/\mathrm{d}T_l = 0$, instead of laser 4.

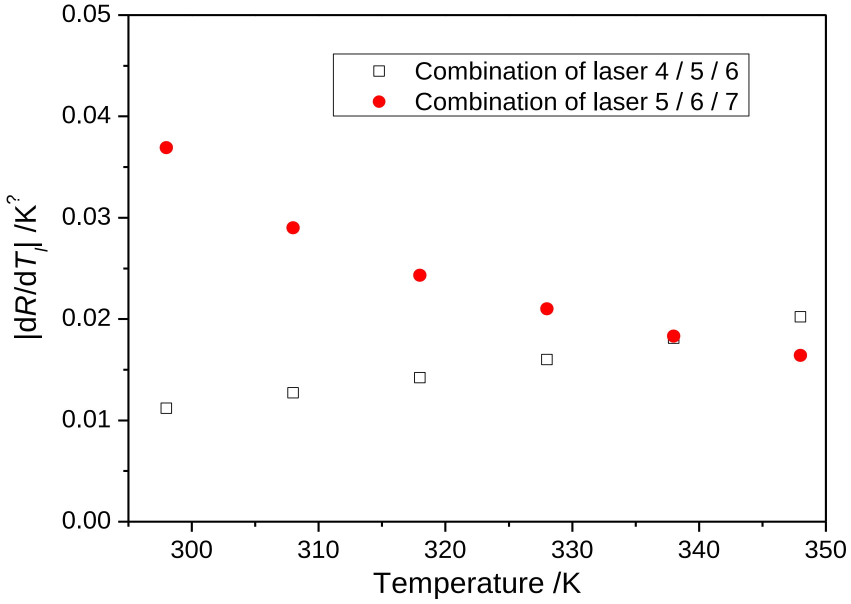

Fig. 49: Sensitivity, $|\mathrm{d}R/\mathrm{d}T_l|$, for the combination of lasers 4 / 5 / 6 (open squares) and 5 / 6 / 7 (filled circles), respectively

The ($|\mathrm{d}R/\mathrm{d}T_l|$) for this laser combined with the same lasers 5 and 6 is also plotted in Fig. 49. The comparison reveals that both combinations have the same sensitivity around 340 K. At T_l < 340 K, the latter combination shows an increased sensitivity. Therefore, when a liquid-phase temperature measurement is attempted only, laser 7 is more attractive than laser 4 (in both cases, combined with lasers 5 and 6). However, laser 7 hits a transition with a very large absorption cross-section, which is not optimal for applications with large film thicknesses. Therefore, the combination with laser 4 gives a reasonable sensitivity leading to the measurement accuracy discussed later.

When inserting eq. (63) into eq. (69) for the respective laser frequencies, the temperature T_l of the liquid can be obtained:

$$T_l = \frac{R(a_4 - a_6) - (a_5 - a_6)}{(b_5 - b_6) - R(b_4 - b_6)} \tag{71}$$

Once T_l is known, d_l can be derived when inserting (72) into (68):

$$d_l = \frac{\ln\left(R_{6/5}\right)}{\left((a_5 + b_5 T_l) - (a_6 + b_6 T_l)\right) \cdot \frac{\rho(T_l)}{M}} \tag{72}$$

Finally, with the insertion of (72) and (73) into (65), u can be determined from the transmittance measured at the frequency of laser 4:

$$u = 1 - \frac{\left({}^{I_t}/_{I_0}\right)_{v6}}{\exp\left(-(a_6 + b_6 T_l) \cdot \frac{\rho(T_l)}{M} \cdot d_l\right)} \tag{73}$$

The four diode lasers (laser 3–6) used in the present work are listed in Table 5 with their respective center wavenumber positions and fractional absorptions for a typical liquid film thickness of 500 µm, and saturated water vapor with 1 cm absorption length at room temperature, respectively.

Table 5: Diode laser frequency positions and calculated fractional absorption values expected for a typical measurement situation

Laser	Center wavenumber position / cm^{-1}	Fractional absorption in 500 µm liquid water (298 K)	Fractional peak absorption in 1 cm saturated water vapor (298 K)
3	7185.59	8.58%	3.48%
4	7390.13 (for vapor phase)	1.55%	6.35%
	7389.47 (for liquid phase)	1.55%	0.8%
5	7082.89	19.52%	0.35%
6	6714.57	20.61%	0.035%

5.3 Experimental setup and results

5.3.1 Calibration tool

In order to validate the performance of the sensor, a series of experiments were performed first on a calibration tool (shown in Fig. 50) [87] with known liquid film thickness and temperature. The home-made calibration tool consists of a stainless-steel trough with two quartz plates (LITHOSIL® synthetic fused silica (grade Q1, Schott)). One is glued into the bottom of the trough, while the other is mounted on a vertical translation stage (Thorlabs). After filling the trough with liquid water, a well-defined film thickness is formed between these two plates once they are adjusted parallel to each other. The plate distance was measured by a caliper with an accuracy of 3 µm. A HeNe-laser was used to align the parallel orientation of the two inner quartz-plate surfaces by adjusting in such a way that the partially reflected rays from both surfaces maintain equal separation close to and at a large distance from the plates. The whole unit was wrapped with heating tape to vary the temperature of the liquid in the trough. The temperature of the liquid was measured with an immersed thermocouple. Incident beam intensities I_0 were determined with the two plates in contact (i.e., virtually zero film thickness).

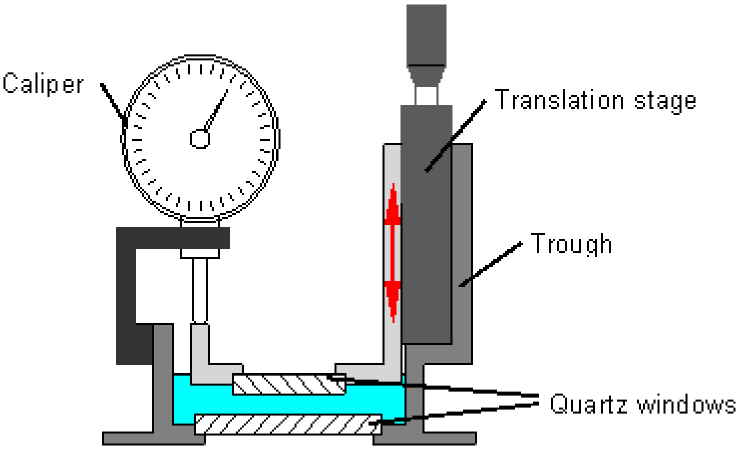

Fig. 50: Calibration tool used for producing liquid layers of known thickness

The TDLAS technique for the simultaneous measurement of water film thickness and liquid-phase temperature in the calibration tool was similar to setups described in chapter 3.4 and 3.5, respectively, and the experiment is depicted in Fig. 51. The calibration tool rested on a round aluminum table. The three selected DFB diode lasers (NEL) (laser 4-6) were current-tuned simultaneously at 100 Hz by the saw-tooth signal from the function generator, and their output was multiplexed by the fiber combiner. The collimated laser beams were then directed through the liquid film at an angle of 2 °with respect to the plate normal in order to avoid etalon effects and then collected by the multimode collection fiber with the collimator and demultiplexed by a diffraction grating before being focused onto three individual InGaAs detectors (Thorlabs, PDA10CS-EC). Control of the experiment and further data processing was performed in LabVIEW (National Instruments) environment. Ten consecutive wavelength scans of the diode lasers were averaged which takes 100 ms.

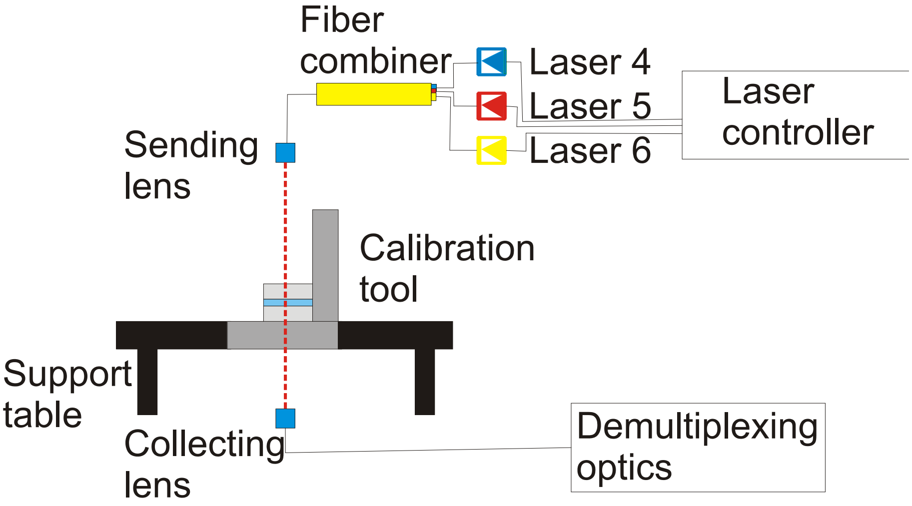

Fig. 51: Experimental setup for validating the thickness measurements in the calibration cell

After the liquid water in the calibration trough had reached constant temperature, simultaneous multi-line transmission measurements were carried out to determine T_l and d_l for plate separations, i.e., liquid layer thicknesses, of 200, 400, 600, and 800 µm, respectively. The correlation between these preset and retrieved values is depicted in Fig. 52.

In Fig. 52a, the three almost horizontal dashed lines mark the respective liquid temperature indicated by the thermocouple readings. These temperature values slightly increase with increasing film thickness, showing a consistent trend with the measured TDLAS temperatures (solid symbols). This may be caused by the fact that the experiments were performed before the film still has not reached thermal equilibrium with the surrounding. It is observed that the largest deviations between the TDLAS and thermocouple temperatures at 800 µm film thickness are around 3 K for measurements at 296 K (squares) and 319 K (triangles), respectively, and around 4.5 K at 309 K (circles). The temperature deviation averaged over all measurements is smaller than 1.5%. This systematic error in accuracy may result from uncertainties in the absorption cross-sections obtained from the previous FTIR measurements. An estimated spectral resolution in the FTIR measurements of ±2 cm^{-1} translates into a ±2 K error in the determination of T_l. The measured film thickness (Fig. 52b) overall is in good agreement with the preset plate separation. However, for each temperature and plate separation the evaluated average thickness value of ten successive scans shows increasing deviations from the given plate separation with increasing film thickness. This observation may be attributed to water impurities, either contained initially in the liquid, or dissolved from the trough walls after filling. This interpretation is also consistent with the trend observed for the non-specific background attenuation, which at room temperature increases from 4 to 17% when the plate separation is increased from 200 µm to 800 µm, respectively. For the present range of conditions the uncertainty in the film-thickness measurements does not exceed 5% for a ten scan average.

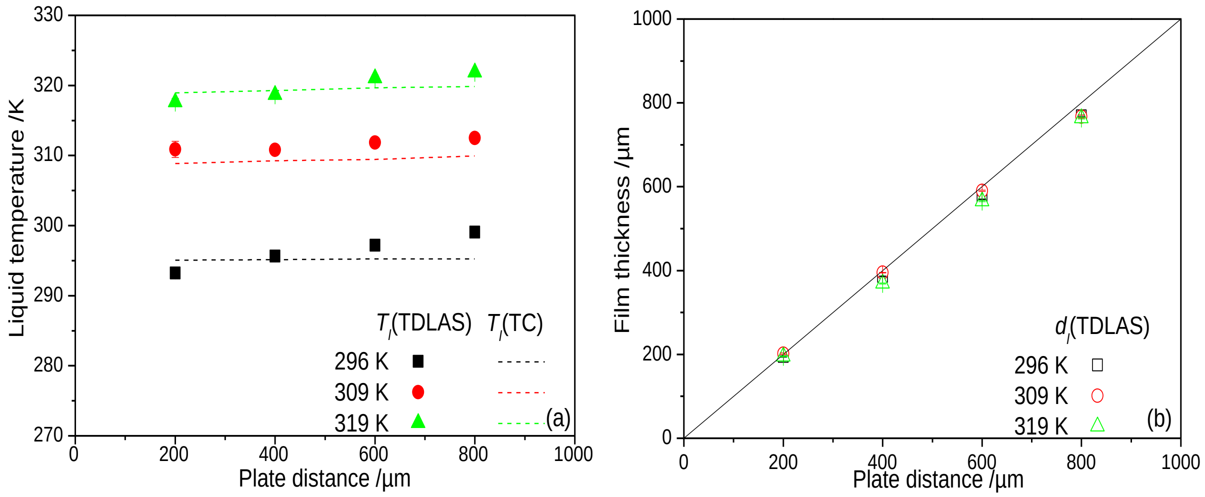

Fig. 52: Measured film temperature (a) (filled symbols by TDLAS and dashed lines by TC) and film thickness (b) (open symbols) as a function of the plate separation in the calibration tool for three set temperatures

5.3.2 Measurement of liquid film thickness on transparent quartz plates

Further experiments were performed for time-resolved simultaneous measurements of liquid film thickness, liquid-phase temperature, and vapor-phase temperature of an evaporating free water film deposited on a polished quartz plate (same material as in the calibration tool). The whole setup is depicted in Fig. 53, which is similar to the one described before for the calibration tool, but with laser 3 added to the system in order to get the vapor-phase temperature above the liquid film. Liquid layers were prepared by dripping small droplets onto the quartz plate using a glass pipette, and the liquid was spread subsequently through gentle mechanical stirring. The film was heated by blowing hot air from a heat gun towards the bottom surface of the plate. The TDLAS laser sending fiber was positioned 10 cm above the film. For shielding the vapor atmosphere above the liquid from room air a cylindrical cup covered both the quartz plate and the sending fiber with the attached collimator lens, and a weak purge flow of dry nitrogen was directed towards the collimator to avoid water condensation on the lens surface. To avoid water vapor interference from ambient air a second nitrogen purge flow was also applied through a T-shaped tubing positioned between the backside of the film supporting plate and the lens-coupled detection fiber. Etalon effects during wavelength scans were avoided by directing the laser beams towards the plate with an angle of incidence of 2 °. A thin thermocouple with diameter 100 µm was immersed into the film as closely as possible to the crossing point with the laser beams to provide coarse real time comparisons with the temperature readings deduced from the TDLAS measurements. The intensities of all beams transmitted through the clean and dry quartz plate were defined as the incident intensities I_0, and measurements were carried out until disturbances by beam steering occurred when the films were strongly distorted due to surface tension effects.

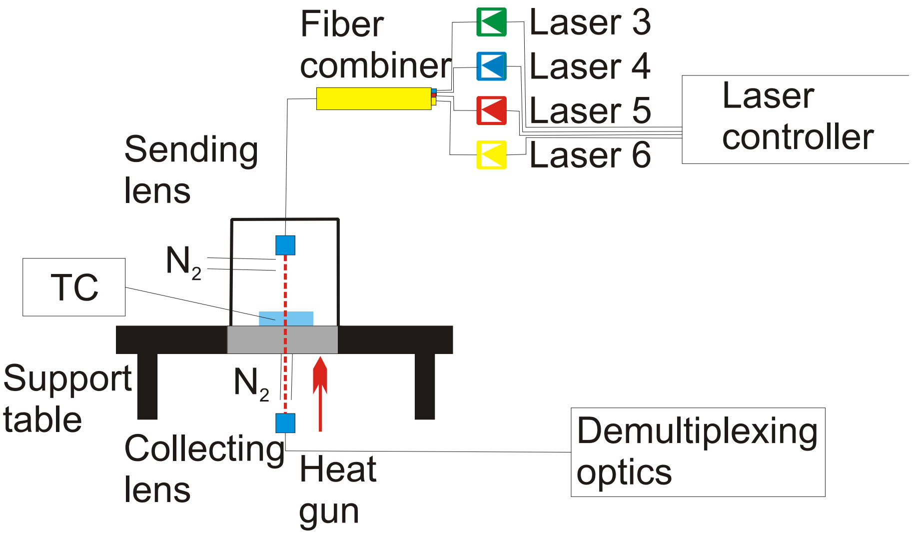

Fig. 53: Experimental setup of liquid film measurement on a transparent quartz plate

Fig. 54 shows the results from the simultaneous time-resolved measurement of the liquid layer thickness (blue triangles), the temperature of the liquid (red circles: TDLAS, open squares: thermocouple (TC)) and the vapor-phase (green diamonds), respectively, for an evaporating open water film deposited on the heated quartz plate. Because the data acquisition time step for the thermocouple reading is 2 s, the other measured parameters were calculated as an average value for 200 consecutive scans at the 100 Hz repetition rate of the TDLAS spectrometer. To not overload the figure only every tenth data point is plotted. For ten repeated measurements the RMS deviation for the measurement of liquid film thickness and temperature is 1.5% and 0.5 K, respectively.

At the start of the evaporation process, the temperature of the liquid is around 295 K and then slowly increases during the first five minutes after data acquisition, before reaching a plateau region at around 332 K for the following 18 minutes. During the initial heating period the film thickness slightly decreases from about 1400 µm to around 1210 µm. In the constant temperature phase the liquid layer thickness linearly decreases until about 300 µm (after 22 min). This behavior can be understood from a simple model of film evaporation off surfaces, as described by the empirical equation [97]:

$$g = \theta \cdot A \cdot (x_s - x) \tag{74}$$

Here, g [kg/h] is the mass flux of liquid water leaving the surface area A [m^2] of the liquid as vapor, and θ [kg/m^{2}h] represents the evaporation coefficient, which for an assumed quiescent atmosphere above the liquid is a constant with a value of 25. x_s [kg/kg] is the humidity ratio in saturated air at the same temperature as the water surface (at 332 K, $x_s = 0.155$), and x [kg/kg] is the given humidity ratio of the surrounding air (0.0175 during the experimental run). For the simulation the initial film thickness was given by 1.22 mm, when the liquid temperature starts to remain at a constant value of 332 K, as indicated by the thermocouple measurements (open squares in Fig. 54). It can be observed that the trend calculated from eq. 74 (solid line) is consistent with the linear decrease of the evaluated TDLAS data.

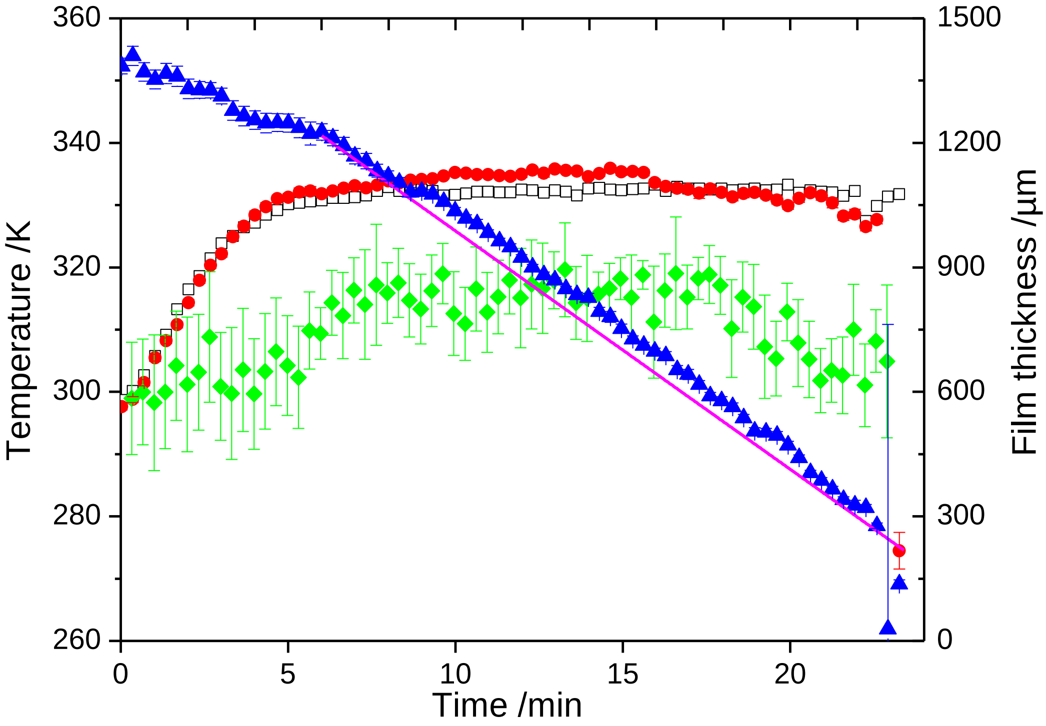

Fig. 54: Time-resolved measurement of film thickness (filled blue triangles), liquid-phase temperature (filled red circles) and vapor-phase temperature (filled green diamonds) during film evaporation. Open squares: Thermocouple measurement in the liquid film

For the determination of vapor-phase temperatures, ten consecutive measurements of laser 3 and 4 were averaged and fitted by Voigt functions before the vapor-phase temperature can be inferred by forming the ratios (eq. (56) in section 2.5.1). The averaged vapor temperature and RMS error for every 2 s during the experimental run is shown in Fig. 54 (green diamonds). At the start of film evaporation the measurement uncertainty is 4% (±10 K). This error is the result of the relatively strong background absorption due to the presence of a thick liquid water layer at the start of the experiment, which at the given laser power reduces the intensity of the transmitted signal for the vapor phase measurements, thus decreasing the signal-to-noise ratio for the scanned absorption lines. This effect can be seen in Fig. 55, where the average from ten consecutive scans are plotted for each water vapor absorption line accessible by laser 1 and 2, respectively, at 6 min (bottom) and 20 min (top) after start of film evaporation. Also shown are their respective Voigt fits and fit residuals (lower panel of each graph). It is observed that the amplitude of the residual at 6 min (second row) on average is larger than at 20 min (first row), i.e., when the film gets thinner a better signal-to-noise ratio is reached and the error decreases to approx. ±6 K.

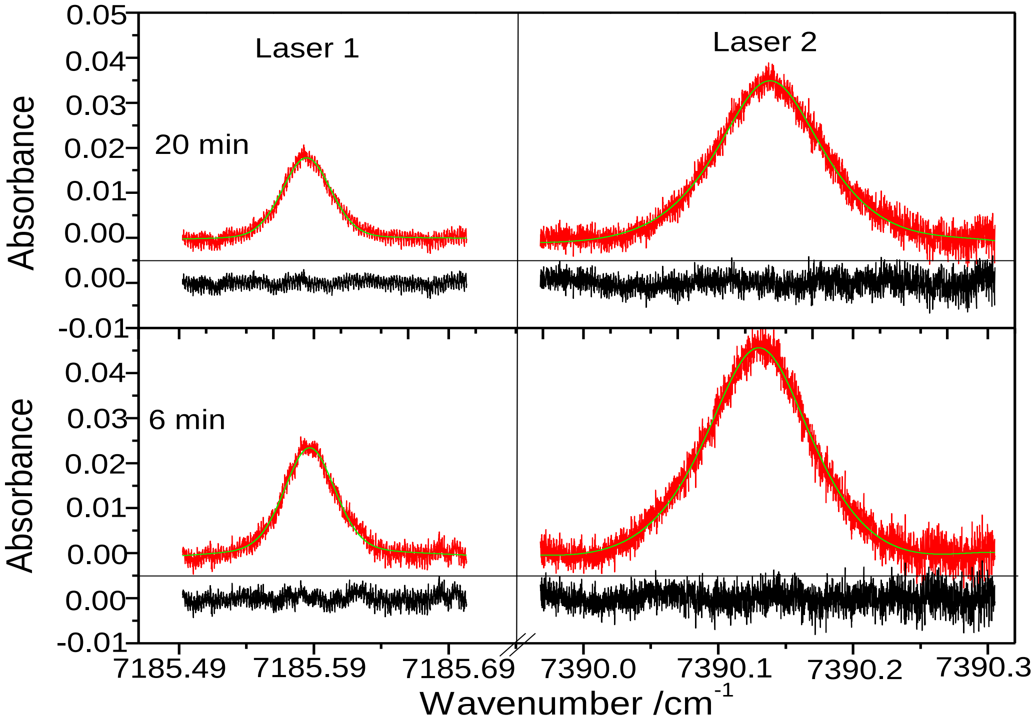

Fig. 55: Average of ten consecutive scans of the water vapor absorption line shapes (accessed by laser 1 and 2, respectively) together with fitted Voigt functions (green solid lines) and corresponding residuals (black lines) 6 min (bottom) and 20 min (top) after start of film evaporation

The measurements reveal that the vapor temperature slightly increases at the beginning of film evaporation and then remains constant at around 315 K, when according to the thermocouple reading the liquid reaches its plateau temperature. Here, the heat loss from the film due to evaporation compensates the heating from the hot air flow towards the plate. Towards the end of film evaporation the vapor temperature decreases slightly while the film gets thinner and its size shrinks, causing the amount of vapor phase water above the film to reduce and its dilution with the continuously room temperature refreshing N_2 purge flow leads to a decrease in the mixing temperature in the gas phase.

After approximately 22 minutes visual inspection shows that the film had shrunk due to mass loss and surface tension effects thus no longer covering the beam crossing area. In the neighborhood of the beams the deformation of the surface of the liquid caused strong steering of the crossing laser beams such that they no longer consistently hit the collimator lens of the receiving fiber. As Fig. 54 shows, this causes strong fluctuations of all derived film parameters. As detailed in the next section this effect could also be observed by a simultaneous recording of shadowgraph images of the liquid film. The detrimental effect of beam steering could be partially avoided by using an integrating sphere as will be demonstrated in the next subsection where film thickness measurements performed in the flow channel will be described.

5.3.3 Comparison of TDLAS and shadowgraphy

To more closely investigate the beam steering effects due to the shrinking of the liquid film at the end of film evaporation on the transparent quartz plate, shadowgraph images were simultaneously taken as a means for tracking the change of film shape during TDLAS film thickness measurements.

For the shadowgraph technique, a continuous wave He-Ne laser (JDS Uniphase 1135P) at 632.8 nm was used as a radiation source. The beam passed a concave lens (*f* = 80 mm) to enlarge its diameter to 40 mm at the film surface. The light transmitted through the liquid film and the quartz plate was reflected by a 45 ° aluminum mirror and projected on a translucent glass screen from where images where taken by an ICCD camera (LaVision, StreakStar). The TDLAS experimental setup was the same as described in section 5.3.2. Care was taken to image the same area on the deposited water film through which the diode laser beam was transmitted.

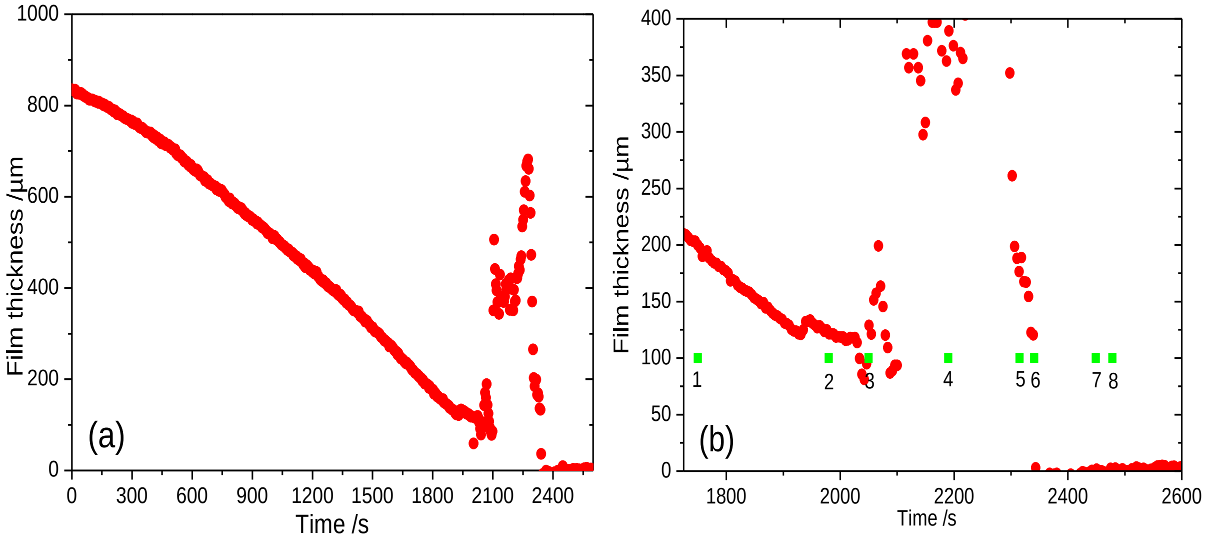

Fig. 56: Film thickness variation measured by TDLAS during the liquid-film evaporation process (a) and the enlarged area at the end of the evaporation process and the eight corresponding number

The film thickness evaluated from the TDLAS measurements is plotted vs. time in Fig. 56. It is observed that the film thickness monotonously decreases during the first 1800 s after the start of the experiment, after which large irregularities in the retrieved values appear (shown in the enlarged area from 1700 to 2600 s in Fig. 56 (b)). Eight specific instances in time (marked as green dots in Fig. 56(b) were chosen where the recorded shadowgraph images where investigated in Fig. 57, where a black dot marks the point of transmission of the NIR laser beams through the film. At 1750 s and 1980 s (instant 1 and 2) the spatial extent of the film has reduced but its shape did not change, thus obviously not disturbing the TDLAS measurements. From 2050 s (instant 3) on the film started to shrink substantially, and until 2341s (instant 6), the NIR laser beams are located at the edge of the film thus being refracted out of the collection angle of the collimating lens with an accompanying large thickness measurement error (cf. Fig. 56). From 2449s (instant 7), the film was totally evaporated at the position where the laser beam transmitted the plate, thus the thickness is zero. An integrating sphere will avoid this effect and will be used in the next section.

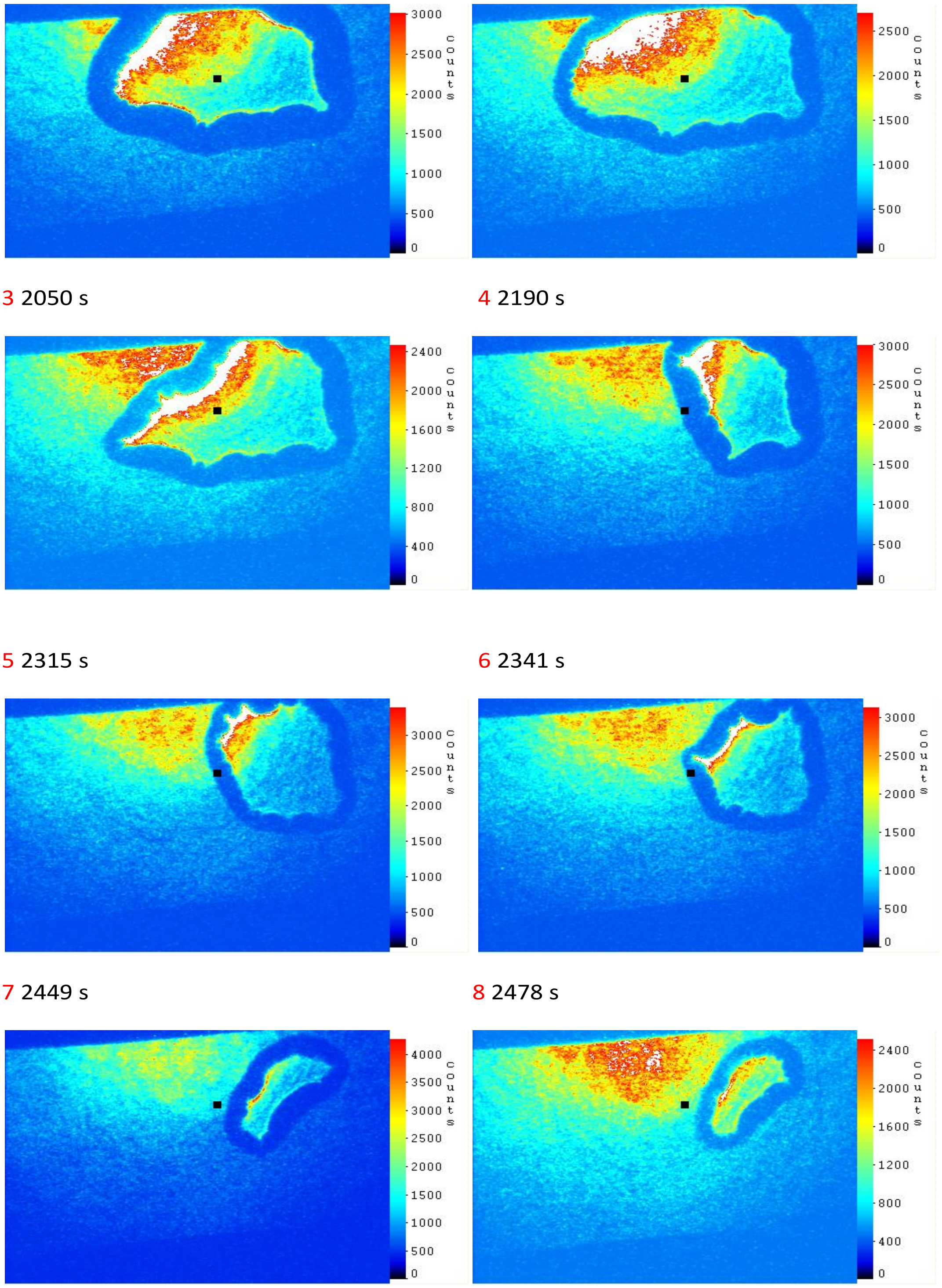

1 1750s

2 1980 s

3 2050 s

4 2190 s

5 2315 s

6 2341 s

7 2449 s

8 2478 s

Fig. 57: Shadowgraph images at the eight specific instants in time (marked as green dots in Fig. 56) during film evaporation

5.3.4 Measurement of liquid film thickness in a flow channel

The experiments presented in section 5.3.2 on liquid films in an enclosed housing were performed in quiescent atmospheres. However, in many practical applications the measurement of liquid film thickness in the presence of gas flows above the film is of great interest. For this purpose a flow channel with rectangular cross section was employed which can provide air flows of various strength.

The experimental setup for film thickness measurements in the flow channel is shown in Fig. 58. The flow channel consists of four separated aluminum segments with square cross section of 50 x 50 mm^2. The two segments at both ends of the channel are with length 21 cm. There is an extra honeycomb structure in the first upstream segment of the channel to laminarize the flow. The two center segments with length 31 cm allow for optical access by transparent quartz windows in all four sidewalls. A three-hole injection nozzle is inserted into the upper sidewall which ejects three closely spaced water spray cones onto the lower sidewall used for film analysis. The air flow velocity in the middle of the channel is to be measured about at maximum of 7.5 m/s [87].

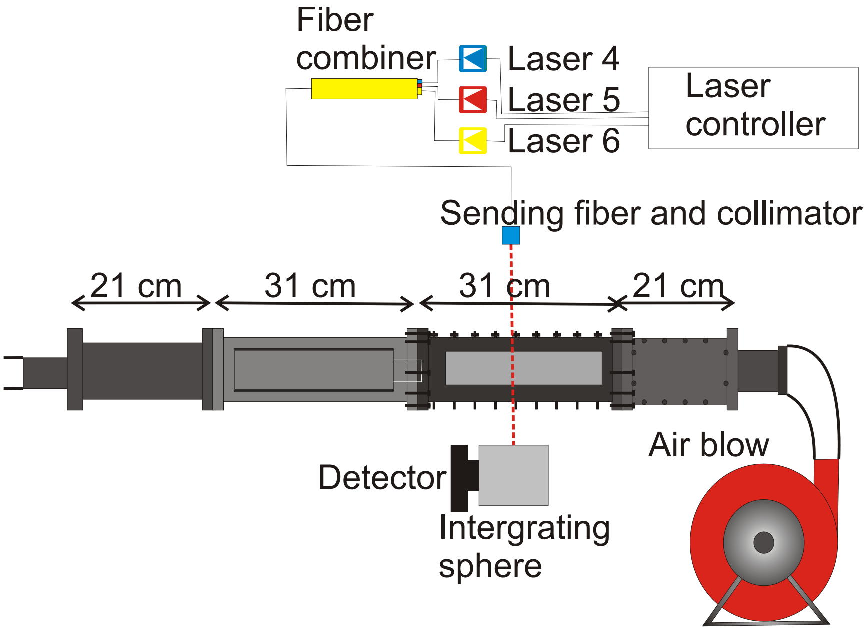

Fig. 58: Experimental setup for film thickness measurements in a flow channel

The TDLAS spectrometer is operated in the time multiplexing mode. Three diode lasers are combined and current scanned by a 100 Hz saw-tooth signal during consecutive time spans. The beams are transmitted through the film. As discussed previously in section 5.3.2 a curved film surface may refract the transmitted beam such that they will not hit the collimation lens (5 mm diameter) of the detection fiber. Hence, an integrating sphere (Thorlabs, IS210C) with a large opening (12.5 mm diameter) was positioned into the transmitted beam path. The sphere interior wall is coated with PTFE-based high reflective bulk material with a reflectivity higher than 98% in the near infrared. An InGaAs detector (Thorlabs, PDA10CS-EC) was inserted into a second 12.5 mm diameter sphere opening at 90 °with respect to the entrance axis for detecting the signal.

Experiments were performed without and with air flow above the film. It should be pointed out that after the injection event by the nozzle three individual water droplets were deposited on the quartz plate. In the following the temporal thickness development of only one of the three droplets was studied. However, in case of the activated air flow the droplets changed their shape and relative position on the plate and eventually combined with one another during the evaporation process.

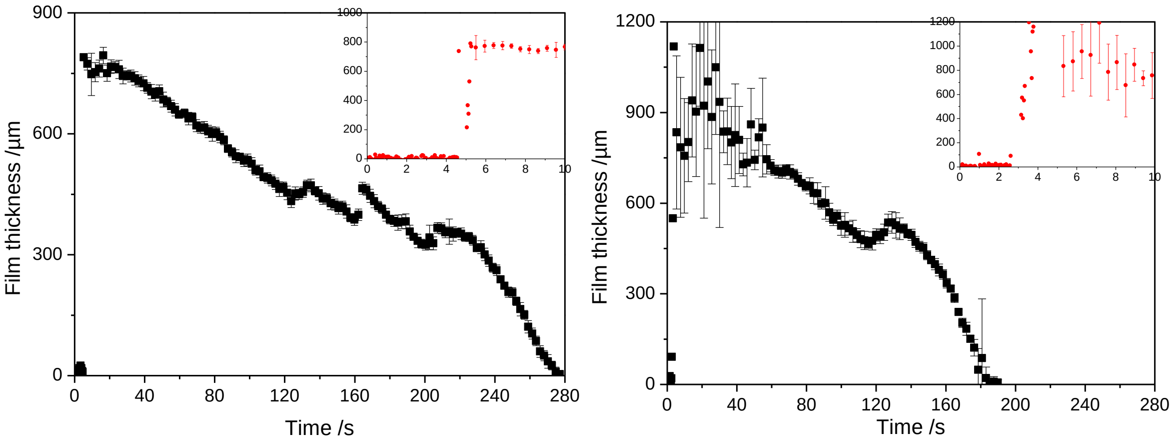

Fig. 59: Film thickness variation (black rectangles) of an impinging water jet with subsequent film evaporation as a function of time in the flow channel, without (a) and with (b) active air flow. Insets: film thickness variation within the first 10 seconds

At the beginning of data acquisition (abbreviated as “BODA”) the transmitted beam intensities were recorded shortly before the water droplets were injected providing a measure for the incident intensities. Fig. 59 shows the deduced film thickness from the recorded absorption ratios during the complete injection-evaporation process without (a) and with (b) an activated channel air flow. In the first case (Fig. 59a), during impingement of one of the water jets hitting the laser beam interaction region the film thickness suddenly increased from zero to ~ 800 µm during a time span of 0.5 s after BODA. The standard deviation of ten consecutive scans of was large due to the thickness of the film with an accompanying small signal-to-noise ratio. Subsequently, the evaporation process caused an almost linear decrease of the film thickness with the exception of three interruptions occurring at around 130, 160, and 210 s after BODA where a short increase of film thickness was recorded, possibly due to a recombination or rearrangement of the three water droplets on the plate. The measured film thickness decreased to zero at around 275 s after BODA; thus, the whole evaporation process can be tracked without excessive variations of the transmitted signal intensity, as it was the case in the previous measurements depicted in Fig. 54 and Fig. 56. Hence, the beam steering effects occurring when the NIR laser beams are refracted off a changing film surface or during interaction with the film boundaries can be avoided by using the integrating sphere.

For the case with an active air flow above the film the retrieved thickness variation is shown in Fig. 59b. Also in this case it drastically increased from zero to ~ 1000 µm within the first 0.5 s after BODA. However, in contrast to the case without active air flow the variation in measured film thickness shows a much stronger fluctuation with a standard deviation of more than ±100 µm within the first minute after BODA. This might have been caused by small air bubbles present and vibrate on the surface of the liquid, their movement in the strong air flow leading to additional beam deflections/deformations not leveled out by the integrating sphere in front of the detector. When these effects disappeared after approx. 60 s the standard deviation of the measurement decreased to levels similar to the case with no air flow. There also are visible temporally short increases in film thickness, e.g. around 140 s after BODA – though much slower than in the case without air flow – which may be ascribed to movement and/or recombination of the individual water droplets on the surface. The air flow assisted film evaporation ceased after approx. 180 s after BODA, roughly within 65% of the time it needed for the case without air flow.

5.3.5 Comparison of TDLAS with tracer LIF and Raman imaging

In collaboration with D. Greszik in our team at IVG the TDLAS technique was compared with two other nonintrusive diagnostic methods for thickness measurements of liquid water: tracer LIF and Raman scattering (for details, see [73, 98]). The liquid films were deposited on the polished quartz plate as described in chapter 5.3.2 (cf. Fig. 60).

Tracer LIF and Raman scattering measurements were performed with a beam from a quadrupled Nd:YAG laser at 266 nm with a pulse energy of 9 ±1 mJ. After a diverging lens the energy was distributed homogeneously in a circular cross section with a diameter of 30 mm and passed from below through the quartz plate for excitation of the liquid film (Fig. 60).

After being reflected from an aluminum mirror the backward propagating signal radiation – either from the tracer fluorescence or from Raman scattering of liquid water – was detected spatially resolved with an ICCD camera (LaVision, StreakStar) fitted with a UV-lens (Coastal Optics, 105 mm focal length, $f_\#$ = 4.5). Fluorescence in the 320–550 nm range was generated from adding 0.1% by weight of ethyl-acetoacetate (EAA) to the liquid, and was filtered from scattered and background light by a 320-nm long-pass filter (Schott WG 320). Further suppression of stray light was accomplished by an edge filter (Semrock RazorEdge LP266 RS). For the Raman measurements a bandpass filter with high transmission in the 290–315 nm range in combination with the edge filter isolated the signal from stray light and LIF [98].

TDLAS measurements were carried out with two NIR diode lasers (laser 2 and 3) with their respective wavenumber positions fixed at positions of 6808.40 cm^{-1} and 7185.10 cm^{-1}, respectively, that are not in resonance with water vapor absorption lines to avoid interference from water vapor present in the beam path outside the liquid.

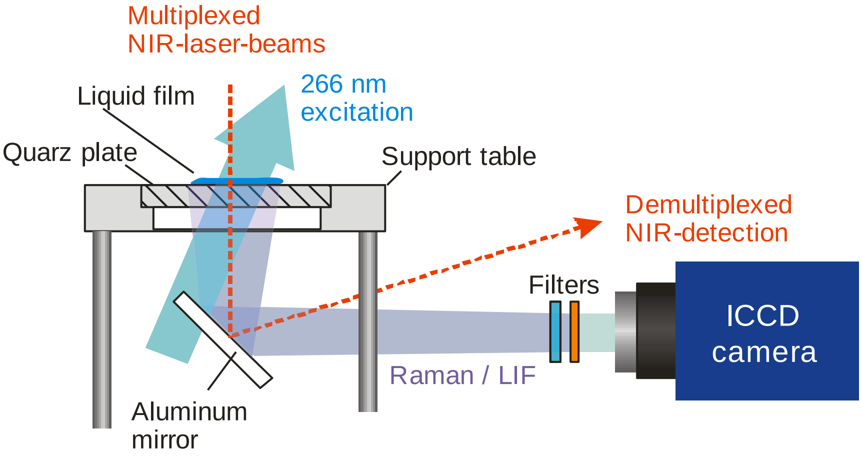

Fig. 60: Excitation and detection arrangement for film measurements on a quartz plate combining Raman-, LIF-imaging, and TDLAS absorption techniques

A liquid water droplet (for the LIF experiments doped with the EAA tracer and for Raman without tracer) was prepared on the plate and the respective signal was recorded continuously during the evaporation process. Again, the evaporation rate of the film was promoted by directing the hot air flow of a blower from below towards the quartz plate. A thermocouple immersed into the liquid indicated a temperature of approximately 323 K during the film evaporation process. Since the LIF and Raman techniques delivered two-dimensional distributions of film thickness [98], data evaluation in the LIF and Raman techniques was performed in an approximately 700 × 700 µm^2 spatial region including the area where the NIR laser beam crossed the liquid layer.

The result of the thickness evaluations from all three simultaneously applied measurement techniques is shown in Fig. 61. Generally, there exists a good correlation between the time-resolved film thickness measurement from the TDLAS and Raman technique (Fig. 61 (a)), respectively, while stronger deviations are visible when comparing the TDLAS with results from the tracer LIF diagnostics (Fig. 61 (b)). Because of the low signal level in the Raman derived film thickness (with a standard deviation of ±35 µm around the linear fit line in the figure), in Fig. 61 (a) the absolute values follow quite closely the trend of the TDLAS data during the whole film evaporation process. On the other hand, during the whole observation time the measured tracer LIF film thickness is smaller than the TDLAS results and results in a 15% deviation at the end. It is also observed that the measured film thickness deduced from LIF data decreases much faster than what is evaluated from the TDLAS diagnostic. This phenomenon can be attributed to a preferential evaporation of the tracer from the solution, showing that a suitable tracer still needs to be found for this system. Alternatively, in cases of sufficient signal levels the tracer free diagnostic technique of spontaneous Raman scattering (or TDLAS) would be more appropriate.

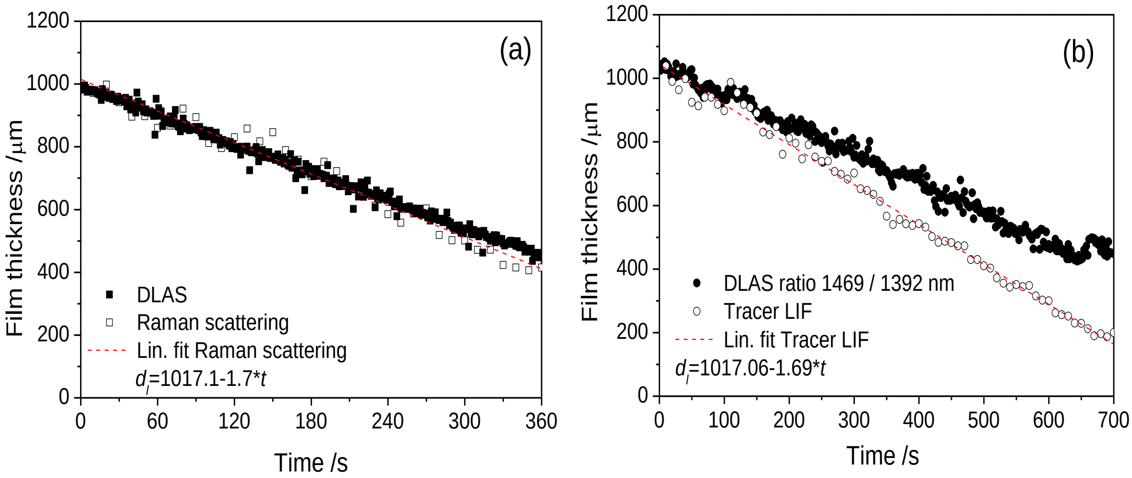

Fig. 61: Variation of liquid water layer thickness with time during film evaporation deduced, respectively, from the Raman (a) and LIF (b) signal intensities (open symbols), in comparison with simultaneously acquired NIR-DLAS ratio measurements (filled symbols). To guide the eye, the Raman and LIF data, respectively, were fitted with a straight line (red dashed line)

5.4 TDLAS liquid water film thickness measurements: Summary

In this work, a multiplexed TDLAS sensor with a wavelength of ~1.4 µm was employed for time-resolved measurements of liquid water film thickness. To reliably determine liquid water film thickness, the absorption strength and the temperature of the liquid must be known accurately. Therefore, absolute absorption cross-sections of liquid water and their temperature dependence were determined by FTIR spectroscopy within the range of the respective laser wavelengths. They were first measured with a FTIR spectrometer for liquid temperatures in the 298–348 K range. Because the liquid-water absorption spectrum shifts towards shorter wavelengths with increasing temperature, a sensitivity analysis enabled a proper choice of three wavelengths (lasers 4–6) for an optimized simultaneous measurement of the temperature of the liquid. This information can be used for correction of the film thickness data obtained from other line-pair ratios. Probing the liquid film at three wavelengths can eliminate other non-specific attenuation caused by surface fowling, reflection and beam steering.

The performance of the sensor was first validated in a calibration tool with liquid layers of known thickness between 200 and 800 µm, and temperatures between 296 and 319 K, respectively. It is found that the uncertainties for the liquid temperature measurement – relative to the thermocouple readings – are ±1.5%, and for film thickness measurements 5% with respect to the manually set plate distance.

Experiments were also performed for time-resolved thickness and temperature measurements of evaporating liquid water films on a transparent quartz plate. The temperatures measured with TDLAS showed good correlations with simultaneous thermocouple recordings. The liquid temperature increased at the beginning, and remained at a constant level during film evaporation as long as thermal equilibrium exists. During film evaporation the thickness linearly decreased, which was also consistent with a simple model of mass loss by evaporation in a humid atmosphere. At beginning of film evaporation the vapor-phase temperature determined by two-line thermometry from the ratio of lasers 3 and 4 has a RMS error of ±10 K due to the large background absorption from the liquid. The error margin decreased to ±6 K when film thickness decreased. The temperature of the liquid measured by the thermocouple and TDLAS correlated well, showing the validity of the optical technique. The vapor-phase temperature increased at the beginning of surface heat up, reached a constant value of 310 K and decreased towards the end of the evaporation process.

Film thickness measurements were also performed during dynamic film formation, i.e., the impingement of a water jet on a quartz plate in the presence of an air stream parallel to the plate. To avoid disturbance of the signal collection due to beam steering caused by distortion of the film during the impingement and the evaporation, an integrating sphere was installed in front of the detector. Diode laser control and data readout was done in a time division multiplexing (TDM) mode. After deposition the film thickness variation was recorded without and with active air flow. It is shown that the film decreased much faster with air flow. However, the accidental presence of air bubbles on the film right after jet impingement caused large standard deviations for the set of thickness values during this event.

The TDLAS technique was also compared with film thickness imaging techniques developed in our lab within the thesis of D. Greszik [87] based on tracer LIF (using ethyl acetoacetate as a fluorescent tracer) and spontaneous Raman scattering, respectively, and simultaneously applied with the TDLAS technique. The comparison showed a good correlation between the TDLAS technique and results from Raman scattering. However, film thickness values deduced from tracer LIF decreased much faster than results from TDLAS because of preferential tracer evaporation.

6 Conclusions and future work

The main objective of this thesis is to investigate the temperature and liquid film thickness measurement with fiber-based, multiplexed diode laser absorption spectroscopy (TDLAS) sensors in combustion-related systems.

6.1 Conclusions

Vapor-phase temperature measurements in combustion-related systems, especially the determination of temperature in systems with inhomogeneous temperature distribution is of great interest in practical applications. In this thesis a multiple parallel scanning measurement technique using several path absorption and temperature binning was employed by monitoring several absorption lines with different lower state energies and estimating different temperature bins to infer the temperature distribution along the laser beam path.

In this thesis a ~1.4 µm tunable diode laser absorption spectroscopy (TDLAS) sensor, using four multiplexed and fiber-coupled DFB diode lasers (lasers 1–4) capable of probing five water-vapor absorption lines was set up and applied in a low-pressure flat-flame reactor. The temperature binning technique was first validated in an atmospheric-pressure flat flame burner with known temperature profile. When applying the sensor into the low-pressure flat-flame reactor, it was shown that the flame was asymmetric since the burner was mounted horizontally. The length fractions of estimated temperature bins evaluated from the TDLAS experiments by a non-negative least-squares fitting procedure were compared with multi-line NO-LIF temperature imaging in the same flame environment. After rotating the burner by 90°, the flame showed a symmetric temperature distribution and TDLAS enabled a 2D temperature reconstruction. For future applications, simulation for specific line selection should be done [20] to maximize temperature measurement sensitivity in the temperature range of interest.

Liquid film measurements are crucial in many practical applications. In this thesis, using four DFB diode lasers (lasers 3–6), the multiplexed TDLAS sensor was applied for the first time for the simultaneous measurement of the thickness and temperature of liquid water films and the vapor-phase temperature above the film by using absorption ratios of four individual laser sources. The developed sensor was first validated in a calibration tool with known film thicknesses and temperatures. This resulted in uncertainties of liquid temperature and thickness of ±1.5% and ~5%, respectively. The sensor was then successfully applied for open evaporating films on a transparent quartz plate and in a flow channel. For the film-thickness measurements in the flow channel, an integrating sphere was used to reduce the effects of beam steering when the laser beams traverse the liquid layer with irregular surface topology. This necessitated time-multiplexing instead of wavelength multiplexing for evaluating absorbances from each laser source. The film thickness evaluated from the TDLAS technique was also compared with other laser-based techniques, e.g., tracer-LIF and Raman imaging. Shadowgraphy was also used to compare with TDLAS in order to investigate the beam-steering effects of TDLAS. The present thesis is the first realization of a NIR diode-laser absorption technique for the simultaneous measurement of liquid water film thickness and temperature.

6.2 Future work

In the present work, direct absorption methods with fixed- and scanned-wavelength spectroscopy were used. With these methods, significant errors occur when the absorption is low and other noise sources exist. Wavelength-modulation spectroscopy (WMS) was demonstrated to be another attractive diagnostic technique, which provides better signal-to-noise ratio (SNR) [55, 99-100]. For WMS, the laser is fast modulated at hundreds of kHz, and the first harmonic ($1f$) and second harmonic ($2f$) of the laser transmission signals are recorded. With $2f$ detection, the sensor sensitivity and accuracy are improved. This technique is more sensitive to the absorption lineshape not only the amplitude, and insensitive to the low-frequency noise. Normalization of $2f$ signal by $1f$ signal can minimize the influences from other non-specific attenuation and is also calibration free. Therefore, to improve the SNR for the further applications in the future, WMS is an advantageous tool [55].

Alternative fuels are currently being developed for internal combustion engines. However, these fuels have different ignition behavior than conventional fuels. Therefore, the ignition delay time is of great interest. Ignition delay times can be measured in shock tubes. The initial gas-dynamic temperature behind the shock wave is usually calculated from the shock wave velocity. However, the temperature history behind the shock wave that is influenced by both, gas-dynamic effects at long test time as well as the thermochemistry of the reaction is of great interest. CO_2 is the main product of hydrocarbon combustion, as mentioned in section 3.4.2, a 2.7 µm spectrometer for CO_2 is developed and that will be applied for the temperature measurements in the shock tube in future.

In this thesis, only pure water liquid film thickness measurement has been studied. Further research will be done with various aqueous solutions. In practical applications, studies on thin films are of interest. Hence, future development of this technique for the characterization of liquid films might focus on other wavelength regions, e.g., in the mid-infrared exhibiting stronger absorption features with larger liquid water absorption cross-sections. Furthermore, detection of film thickness in a reflection mode, e.g., with a retro-reflecting surface would be also studied in the future.

7 Own publications originating from this thesis

7.1 Articles in peer-reviewed journals

1. H. Yang, D. Greszik, I. Wlokas, T. Dreier, C. Schulz, "Tunable diode laser absorption sensor for the simultaneous measurement of water film thickness, liquid- and vapor-phase temperature", Appl. Phys. B, **104**, 21-27 (2011)
2. D. Greszik, H. Yang, T. Dreier, C. Schulz, "Laser-based Diagnostics for the Measurement of Liquid Water Film Thickness", Appl. Opt. **50**, A60-A67 (2011) .
3. H. Yang, D. Greszik, T. Dreier, C. Schulz, "Simulaneous measurement of liquid water film thickness and vapor temperature using near-infrared tunable diode laser spectroscopy," Appl. Phys. B **99**, 385-390 (2010).
4. D. Greszik, H. Yang, T. Dreier, C. Schulz, "Measurements of water film thickness by laser-induced fluorescence and Raman imaging", Appl. Phys.B, **102**, 123-132 (2010) .

7.2 Non peer-reviewed articles and conference publications

1. H. Yang, D. Greszik, T. Dreier, C. Schulz, "Laser-based diagnostics for water-film thickness measurements" (Gordon Conference on Laser Diagnostics in Combustion, Poster, Watervielly, USA, 2011).
2. D. Greszik, H. Yang, T. Dreier, C. Schulz, Measurements of Liquid Film Thickness by Tracer LIF, Raman Scattering and Diode Laser Absorption Spectroscopy" (Laser Applications to Chemical, Security, and Environmental Analysis (LACSEA), San Diego, CA, USA, 2010).
3. C. Hecht, H. Yang, T. Dreier, and Schulz, "In situ Laser Diagnostics of Temperature, Intermediate Species Concentration and Particle Size in Gas-Phase Nanoparticle Synthesis" (Laser Applications to Chemical, Security, and Environmental Analysis (LACSEA), San Diego, CA, USA, 2010).
4. H. Yang, D. Greszik, T. Dreier, C. Schulz, "Diode laser absorption spectroscopy for liquid film thickness measurement on transparent walls" (Gordon Conference on Laser Diagnostics in Combustion, Poster, Watervielly, USA, 2009).
5. C. Hecht, H. Yang, T. Dreier, H. Wiggers, C. Schulz, "3-Dimensional temperature imaging in a low-pressure flame reactor for nanoparticle synthesis using tomographic tunable diode laser absorption and multi-line nitric-oxide laser-induced fluorescence

imaging" (Gordon Conference on Laser Diagnostics in Combustion, Poster, Watervielly, USA, 2009).

6. H. Yang, C. Hecht, T. Dreier, H. Wiggers, C. Schulz, "3-Dimensional temperature imaging in a low-pressure reactor for nanoparticle synthesis using tomographic tunable diode laser absorption and multi-line nitric-oxide laser-induced fluorescence imaging" (4th European Combustion Meeting, Vienna, Austria, 2009).
7. H. Yang, C. Hecht, T. Dreier, H. Wiggers, C. Schulz, "3D tempearture imaging in a low-pressure flame reactor for nanoparticle synthesis using tomographic TDLAS and multi-line NO LIF" (4th European Combustion Meeting, Poster, Vienna, Austria, 2009).
8. H. Yang, M. Hartmann, H. Kronemayer, C. Hecht, T. Dreier, C. Schulz, "A multiplexed diode-laser sensor for temperature measurements in combustion systems" (32nd International Symposium on Combustion, Poster, Montreal, Canada, 2008)

8 References

1. C. Schulz, A. Dreizler, V. Ebert, and J. Wolfrum, "Combustion diagnostics," in *Springer handbook of experimental fluid mechanics*, C. Tropea, J. Foss, and A. Yarin, eds. (Springer, Berlin, 2007).
2. V. Ebert, C. Schulz, H. R. Volpp, J. Wolfrum, and P. Monkhouse, "Laser diagnostics of combustion processes: From chemical dynamics to technical devices," Isr. J. Chem. **39**, 1-24 (1998).
3. J. Wolfrum, T. Dreier, V. Ebert, and C. Schulz, "Laser-based combustion diagnostics," in *Encyclopedia of Anlytical Chemistry*, R. A. Meyers, ed. (John Wiley & Sons Ltd, Chichester, 2000).
4. M. G. Allen, "Diode laser absorption sensors for gas dynamic and combustion flows," Meas. Sci. Technol. **9**, 545-562 (1998).
5. J. A. Silver, and D. J. Kane, "Diode laser measurements of concentration and temperature in microgravity combustion," Meas. Sci. Technol. **10**, 845-852 (1999).
6. E. R. Furlong, D. S. Baer, and R. K. Hanson, "Combustion control and monitoring using a multiplexed diode-laser sensor system," Proc. Comb. Inst. **26**, 2851-2858 (1996).
7. V. Ebert, and J. Wolfrum, "Absorption spectroscopy," in *Optical measurements-techniques and applications*, F. Mayinger, and O. Feldmann, eds. (Springer, Heidelberg, München, 2001), pp. 227-265.
8. H. Kronemayer, W. G. Bessler, and C. Schulz, "Gas-phase temperature imaging in spray systems using multi-line NO-LIF thermometry," Appl. Phys. B **81**, 1071-1074 (2005).
9. C. Schulz, and V. Sick, "Tracer-LIF diagnostics: Quantitative measurement of fuel concentration, temperature and air/fuel ratio in practical combustion situations," Prog. Energy Combust. Sci **31**, 75-121 (2005).
10. E. Barbour, M. Oehlschlaeger, D. Mattison, D. Davidson, C. Schulz, J. Jeffries, and R. Hanson, "UV absorption of CO_2 for temperature diagnostics," Laser Applications to Chemical and Environmental Analysis, Technial Digest (Optical Society of America, 2004), paper MF4.
11. R. P. Lucht, and V. Velur-Natarajan, "Dual-pump coherent anti-stokes Raman scattering temperature and CO_2 concentration measurements," AIAA J. **41**, 679-686 (2003).
12. X. Zhou, X. Liu, J. B. Jeffries, and R. K. Hanson, "Development of a sensor for temperature and water concentration in combustion gases using a single tunable diode laser," Meas. Sci. Technol. **14**, 1459-1468 (2003).
13. H. Teichert, T. Fernholz, and V. Ebert, "In situ measurement of CO, H_2O and gas temperature in a lignite-fired power-plant," Appl. Opt. **42**, 2043-2051 (2003).
14. A. C. Eckbreth, *Laser diagnostics for combustion, temperature and species* (Gordon and Breach Publishers, Amsterdam, 1996).
15. K. Kohse-Höinghaus, and J. B. Jeffries, *Applied combustion diagnostics* (Taylor & Francis, New York, 2002).

16. L. S. Rothman, D. Jacquemart, A. Barbe, D. C. Benner, M. Birk, L. R. Brown, M. R. Carleer, C. C. Jr., K. Chance, L. H. Coudert, V. Dana, V. M. Devi, J.-M. Flaud, R. R. Gamache, A. Goldman, J.-M. Hartmann, K. W. Jucks, A. G. Maki, J.-Y. Mandin, S. T. Massie, J. Orphal, A. Perrin, C. P. Rinsland, M. A. H. Smith, J. Tennyson, R. N. Tolchenov, R. A. Toth, J. V. Auwera, P. Varanasi, and G. Wagner, "The HITRAN 2004 molecular spectroscopic database," J. Quant. Spectrosc. Radiat. Transfer **96**, 139-204 (2005).

17. L. S. Rothman, I. E. Gordon, A. Barbe, D. C. Benner, P. F. Bernath, M. Birk, V. Boudon, L. R. Brown, A. Campargue, J.-P. Champion, K. Chance, L. H. Coudert, V. Dana, V. M. Devi, S. Fally, J.-M. Flaud, R. R. Gamache, A. Goldman, D. Jacquemart, I. Kleiner, N. Lacome, W. J. Lafferty, O. V. Naumenko, A. V. Nikitin, J. Orphal, V. I. Perevalov, A. Perrin, A. Predoi-Cross, C. P. Rinsland, M. Rotger, M. Simeckova, M. A. H. Smith, K. Sung, S. A. Tashkun, J. Tennyson, R. A. Toth, A. C. Vandaele, and J. V. Auwera, "The HITRAN 2008 molecular spectroscopic database," J. Quant. Spectrosc. Radiat. Transfer **110**, 533-572 (2009).

18. X. Liu, J. B. Jeffries, R. K. Hanson, K. M. Hinckley, and M. A. Woodmansee, "Development of a tunable diode laser sensor for measurements of gas turbine exhaust temperature," Appl. Phys. B **82**, 469-478 (2006).

19. M. P. Arroyo, and R. K. Hanson, "Absorption measurements of water-vapor concentration, temperature and line-shape parameters using a tunable InGaAsP diode laser," Appl. Opt., 6105-6116 (1993).

20. X. Liu, "Line-of-sight absorption of H_2O vapor: Gas temperature sensing in uniform and nonuniform flows," (Dissertation, Stanford University, USA, 2006).

21. S. Wittig, J. Himmelsbach, B. Noll, H. J. Feld, and W. Samenfink, "Motion and evaporation of shear-driven liquid films in turbulent gases," Journal of Engineering for Gas Turbines and Power **114**, 395-400 (1992).

22. T. A. Shedd, and T. A. Newell, "Automated optical liquid film thickness measurement method," Rev. Sci. Instrum. **69**, 4205-4213 (1998).

23. A. A. Mouza, N. A. Vlachos, S. V. Paras, and A. J. Karabelas, "Measurement of liquid film thickness using a laser light absorption method," Exp. Fluids **28**, 355-359 (2000).

24. A. Schagen, and M. Modigell, "Local film thickness and temperature distribution measurement in wavy liquid films with a laser-induced luminescence technique," Exp. Fluids **43**, 209-221 (2007).

25. M. I. Nathan, W. P. Dumke, G. Burns, F. H. Dills, and G. Lasher, "Stimulated emission of radiation from GaAs *p-n* junctions," Appl. Phys. Lett **1**, 62-64 (1962).

26. T. M. Quist, R. J. Keyes, W. E. Krag, B. Lax, A. L. McWhorter, R. H. Rediker, and H. J. Zeigler, "Semiconductor Maser of GaAs," Appl. Phys. Lett **1**, 91-92 (1962).

27. R. N. Hall, G. E. Fenner, J. D. Kingsley, T. J. Soltys, and R. O. Carlson, "Coherent light emission from GaAs junctions," Phys. Rev. Lett **9**, 366-369 (1962).

28. N. G. Basov, B. M. Vul, and Y. M. Popov, "Quantum mechanical semiconductor generators of electromagnetic oscillations," J. Exptl. Theoret. Phys. (USSR) **37**, 587-588 (1959).

29. W. W. Chow, and S. W. Koch, *Semiconductor laser fundamentals: Physics of the gain materail* (Springer-Verlag, Berlin, 1999).
30. M. C. Amann, and J. Buus, *Tunable laser diodes* (Artech House, Boston, 1998).
31. M. Teshima, "Dynamic wavelength tuning characteristics of the 1.5-μm three-section DBR lasers: Analysis and experiment," IEEE J. Quant. Electron. **31**, 1389-1400 (1995).
32. P. Aktins, and J. d. Paula, *Physical chemistry* (Oxford University Press Inc., New York, 2002).
33. R. K. Hanson, *Introduction to spectroscopic diagnostics for gases* (Stanford University, 2001).
34. C. N. Banwell, and E. M. McCash, *Fundamentals of molecular spectroscopy* (McGraw-Hill Book Co., Maidenhead, Berkshire, 1994).
35. A. Yariv, *An introduction to theory and applications of quantum mechanics* (Wiley, NY, 1982).
36. W. Demtröder, *Laser Spectroscopy: Basic Concepts and Instrumentation* (Springer, Berlin, 1996).
37. E. E. Whiting, "An empirical approximation to the Voigt profile," J. Quant. Spectrosc. Radiat. Transfer **8**, 1379-1384 (1968).
38. F. Schreier, "The Voigt and complex error function: A comparison of computational methods," J. Quant. Spectrosc. Radiat. Transfer **48**, 743-762 (1992).
39. J. Humlicek, "Optimized computation of the Voigt and complex probability functions," J. Quant. Spectrosc. Radiat. Transfer **27**, 437-444 (1982).
40. D. W. Mattison, J. B. Jeffries, R. K. Hanson, R. R. Steeper, S. D. Zilwa, J. E. Dec, M. Sjoberg, and W. Hwang, "In-cylinder gas temperature and water concentration measurements in HCCI engines using a multiplexed-wavelength diode-laser system: Sensor development and initial demonstration," Proc. Combust. Inst. **31**, 791-798 (2007).
41. A. D. Griffiths, and A. F. P. Houwing, "Diode laser absorption spectroscopy of water-vapor in a scramjet combustion," Appl. Opt. **44**, 6653-6659 (2005).
42. M. Born, and E. Wolf, *Principles of optics* (Pergamon, Oxford, 1975).
43. L. C. Philippe, and R. K. Hanson, "Lase diode wavelength-modulation spectroscopy for simultanoues measurment of temperature, pressure and velocity in shock-heated oxygen flows," Appl. Opt. **32**, 6090-6103 (1993).
44. S. T. Sanders, J. Wang, J. B. Jeffries, and R. K. Hanson, "Diode-laser absorption sensor for line-of-sight gas temperature distributions," Appl. Opt. **40**, 4404-4415 (2001).
45. X. Ouyang, and P. L. Varghese, "Line-of-sight absorption measurements of high temperature gases with thermal and concentration boundary layers," Appl. Opt. **28**, 3979-3984 (1989).
46. F. Y. Zhang, T. Fujiwara, and K. Komurasaki, "Diode-laser tomography for arcjet plume reconstruction," Appl. Opt. **40**, 957-964 (2001).

47. W. J. A. Dahm, S.-J. Chen, J. A. Silver, J. A. Mullin, and N. D. Pilltch, "Mixture fraction measurements via WMS-ITAC in a microgravity vortex ring diffusion flame," Proc. Combust. Inst. **29**, 2519-2526 (2002).
48. P. Kauranen, H. M. Hertz, and S. Svanberg, "Tomographic imaging of fluid flows by the use of two-tone frequency-modulation spectroscopy," Opt. Lett. **19**, 1489-1491 (1994).
49. J. T. C. Liu, G. B. Rieker, J. B. Jeffries, M. R. Gruber, C. D. Carter, T. Mathur, and R. K. Hanson, "Near-infrared diode laser absorption diagnostic for temperature and water vapor in a scramjet combustor," Appl. Opt., 6701-6711 (2005).
50. M. A. Bolshov, Y. A. Kuritsyn, V. V. Liger, V. R. Mironenko, S. B. Leonov, and D. A. Yarantesv, "Measurements of the temperature and water vapor concentration in a hot zone by tunable diode laser absorption spectroscopy," Appl. Phys. B **100**, 397-407 (2010).
51. A. R. Awtry, B. T. Fisher, R. A. Moffatt, V. Ebert, and J. W. Fleming, "Simultaneous diode laser based in situ quantification of oxygen, carbon monoxide, water vapor, and liquid water in a dense water mist environment," Proc. Comb. Inst. **31**, 799-806 (2007).
52. L. S. Rothman, I. E. Gordon, R. J. Barber, H. Dothe, R. R. Gamache, A. Goldman, V. Perevalov, S. A. Tashkun, and J. Tennyson, "HITEMP, the high-temperature molecular spectroscopic database," J. Quant. Spectrosc. Radiat. Transfer **111**, 2139-2450 (2010).
53. "HITRAN homepage, http://www.cfa.harvard.edu/HITRAN/ ".
54. X. Zhou, X. Liu, J. B. Jeffries, and R. K. Hanson, "Selection of NIR H_2O absorption transitions for in-cylinder measurement of temperature in IC engines," Meas. Sci. Technol. **16**, 2437-2445 (2005).
55. H. Li, A. Farooq, J. B. Jeffries, and R. K. Hanson, "Near-infrared diode laser absorption sensor for rapid measurements of temperature and water vapor in shock tube," Appl. Phys. B **89**, 407-416 (2007).
56. J. Yin, "Setup and demonstration of a tunable diode-laser gas-temperature sensor for combustion systems," (Bachelor Thesis, University of Duisburg-Essen, Germany, 2007).
57. D. W. Mattison, J. T. C. Liu, J. B. Jeffries, and R. K. Hanson, "Tunable diode-laser temperature sensor for evaluation of a valveless pulse detonation engine," 43rd AIAA-2005-0224 (2005).
58. H. Yang, "Setup and application of a multiplexed diode-laser gas-temperature sensor for combustion systems," (Master Thesis, University of Duisburg-Essen, Germany, 2008).
59. G. B. Rieker, J. B. Jeffries, and R. K. Hanson, "Calibration-free wavelength-modulation spectroscopy for measurements of gas temperature and concentration in harsh environments," Appl. Opt. **48**, 5546-5560 (2009).
60. K. Wunderle, S. Wagner, I. Pasti, R. Pieruschka, U. Rascher, U. Schurr, and V. Ebert, "Distributed feedback diode laser spectrometer at 2.7 µm for sensitive, spatially resolved H_2O vapor detection," Appl. Opt. **48**, 172-182 (2009).
61. A. Farooq, J. B. Jeffries, and R. K. Hanson, "Sensitive detection of temperature behind reflected shock waves using wavelength modulation spectroscopy of CO_2 near 2.7 µm," Appl. Phys. B **96**, 161-173 (2009).

62. A. Farooq, J. B. Jeffries, and R. K. Hanson, "CO_2 concentration and temperature sensor for combustion gases using diode-laser absorption near 2.7 µm," Appl. Phys. B **90**, 619-628 (2008).
63. D. S. Baer, and R. K. Hanson, "Multiplexed diode-laser sensor system for simultaneous H_2O, O_2 and temperature measurements," Opt. Lett. **19**, 1900-1902 (1994).
64. V. Ebert, T. Fernholz, C. Giesemann, H. Pitz, H. Teichert, J. Wolfrum, and H. Jaritz, "Simultaneous diode-laser-based in-situ-detection of multiple species and temperature in a gas-fired power-plant," Proc. Comb. Inst. **28**, 423-430 (2000).
65. T. I. Palaghita, and J. M. Seitzman, "Pattern factor sensing and control based on diode laser absorption," 41st AIAA-2005-3578 (2005).
66. W. Hentschel, A. Grote, and O. Langer, "Measurement of wall film thickness in the intake manifold of a standard production SI engine by a spectroscopic technique," SAE Technical Paper, 972832 (1997).
67. M. C. Drake, T. D. Fansler, A. S. Solomon, and J. G. A. Szekely, "Piston fule films as a source of smoke and hydrocarbon emissions from a wall-controlled spark ignited direct-injection engine," SAE Technical Paper, 2003010547 (2003).
68. P. G. Felton, D. C. Kyritsis, and S. K. Fulcher, "LIF visualiaztion of liquid fuel in the intake manifold during cold start," SAE Technical Paper, 952464 (1995).
69. J. R. Mawhinney, and J. K. Richardson, "A review of water mist fire suppression research and development," Fire Technol. **33**, 54-90 (1996).
70. J. Gieshoff, M. Pfeifer, A. Schafer-Sindlinger, P. C. Spurk, G. Garr, T. Leprince, and M. Crocker, "Advanced urea SCR catalysts for automotive applications," SAE Technical Paper, 2001010514 (2001).
71. E. T. Hurlburt, and T. A. Newell, "Optical measurement of liquid film thickness and wave velocity in liquid film flows," Exp. Fluids **21**, 357-362 (1996).
72. E. Kull, G. Wiltafsky, W. Stolz, K. D. Min, and E. Holder, "Two-dimensional visualization of liquid layers on transparent walls," Opt. Lett. **22**, 645-647 (1997).
73. D. Greszik, H. Yang, T. Dreier, and C. Schulz, "Measurement of water film thickness by laser-induced fluorescence and Raman imaging," Appl. Phys. B **102**, 123-132 (2011).
74. J. M. Porter, J. B. Jeffries, and R. K. Hanson, "Mid-infrared absorption measurements of liquid hydrocarbon fuels near 3.4 µm," J. Quant. Spectrosc. Radiat. Transfer **110**, 2135-2147 (2009).
75. J. M. Porter, J. B. Jeffries, and R. K. Hanson, "Mid-infrared laser-absorption diagnostic for vapor-phase fuel mole fraction and liquid fuel film thickness," Appl. Phys. B **102**, 345-355 (2011).
76. W. Alderfer D, G. C. Herring, M. Danehy Paul, T. Mizukaki, and K. Takayama, "Submicrosecond temperature measurement in liquid water with laser-induced thermal acoustics," Appl. Opt. **44**, 2818-2826 (2005).
77. V. Simanzhenkov, P. Ifeacho, H. Wiggers, J. Knipping, and P. Roth, "Synthesis of germanium oxide nanoparticles in low-pressure premixed flames," J. Nanosci. Nanotechnol. **4**, 157-161 (2004).

78. H. Kronemayer, "Laser-based temperature diagnostics in practical combustion systems," (Dissertation, University of Heidelberg, Germany, 2007).
79. S. M. Schoenung, and R. K. Hanson, "Carbon monoxide and temperature measurements in a flat flame by laser absorption spectroscopy and probe techniques," Combust. Sci. Technol. **24**, 227-237 (1981).
80. J. Wang, M. Maiorov, J. B. Jeffries, D. Z. Garbuzov, J. C. Connolly, and R. K. Hanson, "A potential remote sensor of CO in vehicle exhausts using 2.3 µm diode lasers," Meas. Sci. Technol. **11**, 1576-1584 (2000).
81. J. M. Seitzman, and B. T. Scully, "Broadband infrared absorption sensor for high-pressure combustor control," J. Propul. Power **16**, 994-1001 (2000).
82. W. G. Bessler, and C. Schulz, "Quantitative multi-line NO-LIF temperature imaging," Appl. Phys. B **78**, 519-533 (2004).
83. H. Kronemayer, P. Ifeacho, C. Hecht, T. Dreier, H. Wiggers, and C. Schulz, "Gas-temperature imaging in a low-pressure flame reactor for nanoparticle synthesis with multi-line NO-LIF thermometry," Appl. Phys. B **88**, 373-377 (2007).
84. C. Hecht, "Laserspektroskopische Charakterisierung von Reaktionsprozessen zur Gasphasensynthese von Nanopartikeln," (University of Duisburg-Essen, Duisburg, 2011).
85. W. G. Bessler, C. Schulz, V. Sick, and J. W. Daily, "A versatile modeling tool for nitric oxide LIF spectra (http://www.lifsim.com)," in *3rd Joint meeting of the US sections of the Combustion Institute*(Chicago, 2003), pp. PI1-6.
86. X. Liu, J. B. Jeffries, and R. K. Hanson, "Measurement of nonuniform temperature distributions using line-of-sight absorption spectroscopy," AIAA J. **45**, 411-419 (2007).
87. D. Greszik, "Entwicklung eines laseroptischen Messverfahrens zur Quantifizierung der Schichtdicke von Wasserfilmen," (Universität Duisburg-Essen, 2011).
88. D. Eisenberg, and W. Kauzmann, *The structure and properties of water* (Oxford University Press, London, 1969).
89. J.-J. Max, and C. Chapados, "Isotope effects in liquid water by infrared spectroscopy. III. H_2O and D_2O spectra from 6000 to 0 cm^{-1}," J. Chem. Phys. **131**, 184505 (2009).
90. G. M. Hale, and M. R. Querry, "Optical constants of water in the 200-nm to 200-µm wavelength region," Appl. Opt. **12**, 555-563 (1973).
91. L. Kou, D. Labrie, and P. Chylek, "Refractive indices of water and ice in the 0.65- to 2.5-µm spectral range," Appl. Opt. **32**, 3531-3540 (1993).
92. J. R. Collins, "Change in the infra-red absorption spectrum of water with temperature," Phys. Rev. **26**, 771-779 (1925).
93. X. Chao, J. B. Jeffries, and R. K. Hanson, "Absorption sensor for CO in combustion gases using 2.3 µm tunable diode lasers," Meas. Sci. Technol. **20**, 115201/115201-115201/115209 (2009).
94. A. D. Griffiths, and A. F. P. Houwing, "Diode laser absorption spectroscopy of water vapor in a scramjet combustor," Appl. Opt. **44**, 6653-6659 (2005).

95. H. Yang, D. Greszik, T. Dreier, and C. Schulz, "Simultaneous measurement of liquid water film thickness and vapor temperature using near-infrared tunable diode laser spectroscopy," Appl. Phys. B **99**, 385-390 (2010).
96. D. R. Lide, *Handbook of Chemistry and Physics, 75th Edition* (Taylor & Francis, Florida, 1994).
97. "The Engineering Toolbox, http://www.engineeringtoolbox.com/evaporation-water-surface-d_690.html," (2010).
98. D. Greszik, H. Yang, T. Dreier, and C. Schulz, "Laser-based diagnostics for the measurement of liquid water film thickness," Appl. Opt. **50**, 60-67 (2011).
99. J. T. C. Liu, J. B. Jeffries, and R. K. Hanson, "Wavelength modulation absorption spectroscopy with 2f detection using multiplexed diode lasers for rapid temperature measurements in gaseous flows," Appl. Phys. B **78**, 503-511 (2004).
100. V. Ebert, K.-U. Pleban, and J. Wolfrum, "In-situ oxygen-monitoring using near-infrared diode lasers and wavelength modulation spectroscopy," Laser Applications to Chemical and Environmental Analysis, Technial Digest (Optical Society of America, 1998), 206-209.

9 List of abbreviations

a	Voigt parameter
a_Q	Coefficients of 3rd polynomial expression for water vapor partition function
A_i	Integrated area
A	Surface area of the liquid
a_i	Respective fitting coefficients
α_ν	Spectral absorbance
A_{21}	Einstein coefficients of spontaneous emission
B	Rotational constant
b_Q	Coefficients of 3rd polynomial expression for water vapor partition function
B_{12}	Einstein coefficients of induced absorption
B_{21}	Einstein coefficients of stimulated emission
b_i	Respective fitting coefficients
c	Speed of light
c_Q	Coefficients of 3rd polynomial expression for water vapor partition function
d	Distance between two parallel plates in etalon
d_Q	Coefficients of 3rd polynomial expression for water vapor partition function
d_g	Distance between parallel grooves in grating
d_l	Length of absorbing medium (water)
dx	Gas medium with differential length dx
$\Delta\nu$	Full width at half maximum (FWHM)
$\Delta\nu_C$	Collisional FWHM
$\Delta\nu_D$	Doppler FWHM
$\Delta\nu_S$	Pressure-induced frequency shift
ΔE_i	Uncertainty of energy of two states in the absorption transition with limited lifetime
δ_i	Collisional line shifting coefficients
E_e	Electron energy
E_F	Fermi energy
E_{Fc}	Quasi-Fermi levels for conduction band
E_{Fv}	Quasi-Fermi levels for valence band
E	Total energy
E_{elec}	Electronic energy

E_{vib}	Vibrational energy
E_{rot}	Rotational energy
ε_i	Common energy at each individual states
ΔE	Energy difference at two quantum states
E''	Lower-state energy of the quantum transition
FSR	Free spectral range
f_j	Length fraction for each temperature bin
f_i	Fraction of molecules or atoms in energy level *i*
$f(E)$	Probability that an electron state at energy is occupied by an electron
$\phi(v)$	Normalized lineshape function
$\phi_C(v)$	Lorentzian lineshape function
$\phi_D(v)$	Doppler lineshape function
$\phi_V(v)$	Voigt lineshape function
g_i	Degeneracy of the level *i*
γ_i	Collisional line broadening half-width
g	Mass flux of liquid water
h	Planck’s constant
$\hbar$	Reduced Planck’s constant
H	Peak absorbance (height) at the line center of transition
i	Energy level, isolated transition
I_v	Incident intensity
I_0	Initial intensity
I_t	Transmitted light intensity
J	Rotational quantum number
J'	Quantum number for the upper state
J''	Quantum number for the lower state
k	Boltzmann constant
k_v	Absorption coefficient
λ	Wavelength
L	Pathlength
m	Mass of molecule
m	order of diffraction
m	number of selected absorption transitions in temperature-binning technique

M	Molar mass
m_i	Temperature-dependent coefficients
N	Total number of molecules
n	Refractive index
n	molar concentration of the absorbing species
n_1	Number density at state 1
n_i	Temperature dependent coefficients
ν	Frequency
υ	Vibrational quantum number
$\tilde{\nu}$	Wavenumber
ν_0	Center frequency of the transition
p	Pressure
Q	Partition function
Q_{elec}	Electronic partition function
Q_{vib}	Vibrational partition function
Q_{rot}	Rotational partition function
θ_i	Incident angle
θ_m	Diffraction angle
θ	Evaporation coefficient
ρ	Density
R	Ratio
$\rho(\nu)$	Spectral density
S	Line strength
σ_ν	Frequency-dependent absorption cross section
T	Temperature
τ	Transmission
T_0	Reference temperature
T_l	Liquid temperature
τ_i	Lifetime of state i
τ'	Lifetime for upper state
τ''	Lifetime for lower state
$U(x)$	Potential field
u	Non-specific background attenuation

$V(a,w)$	Voigt function
w_e	Energy spacing between adjacent quantum states
x_{abs}	Mole fraction of the absorption species
x_i	Mole fraction of the component *i*
x_s	Humidity ratio in saturated air at the same temperature as water surface
x	Humidity ratio in surrounding air
$\Psi(x)$	Time-independent Schrödinger's wave equation

10 Acknowledgements

I am sincerely grateful to Prof. Dr. Christof Schulz for his support and guidance during my work. Thanks for his insightful ideas and suggestions. For my questions, he always answers immediately since he leads such a large group. Special thanks for offering me the opportunity to attend several international conferences.

I would like to acknowledge Dr. Thomas Dreier for his patience and great help through my research and read on this thesis. And I would like also thank Prof. Ron Hanson and Dr. Jay Jeffries from Stanford University for the discussion and advice in my research.

Further, I also want to acknowledge all the colleagues who have provided help during this work. I want to thank Christian Hecht, especially for the measurement in the low-pressure flame reactor; to Daniel Greszik, for the collaboration of film thickness measurements and the other colleagues in the IVG group: Ahmed, Alessandro, Ali, Ashrina, Barbara Graf, Barbara Nota, Beate, Ben, Benjamin, Birgit, Christian Meffert, Christopher, Claudia, Dennis, Dieter, Eugen, Hartmut, Hans, Heidi, Helge, Ingo, Irenäus, Jörg, Khadijeh, Ludger, Malin, Markus, Michaela, Martin Leschowski, Martin Schild, Metehan, Mohammad, Mustapha, Natascha, Nejra, Nils, Oliver, Omid, Ralf, Robert, Sebastian Hardt, Sebastian Kaiser, Shuying, Sonja, Stefan, Steffen, etc. Thanks for the nice atmosphere all of them have brought to me. Especially, thanks to the whole diagnostic group for the discussion in the group meeting every week.

Meantime, thanks to the mechanical workshop (Ulrich Visser, Harald Landmann, etc.) and optical workshop (Martin Jerman) at the University of Duisburg-Essen for their production of parts for my experimental setup.

I would like to give special thanks to my husband, Ping Deng, for his love, support and confidence in me. He always encourages me when I meet difficulties. I am grateful to my whole family, my grandparents, parents, parents-in-law, sister and brother. Thanks for their love, understanding and supporting of my study in Germany.